DIPLOMA THESIS

conducted at the X-Ray Centre of TU Wien

Crystal Chemistry of Copper Lead Selenide Thermoelectrics with Sulfosalt-type Structures

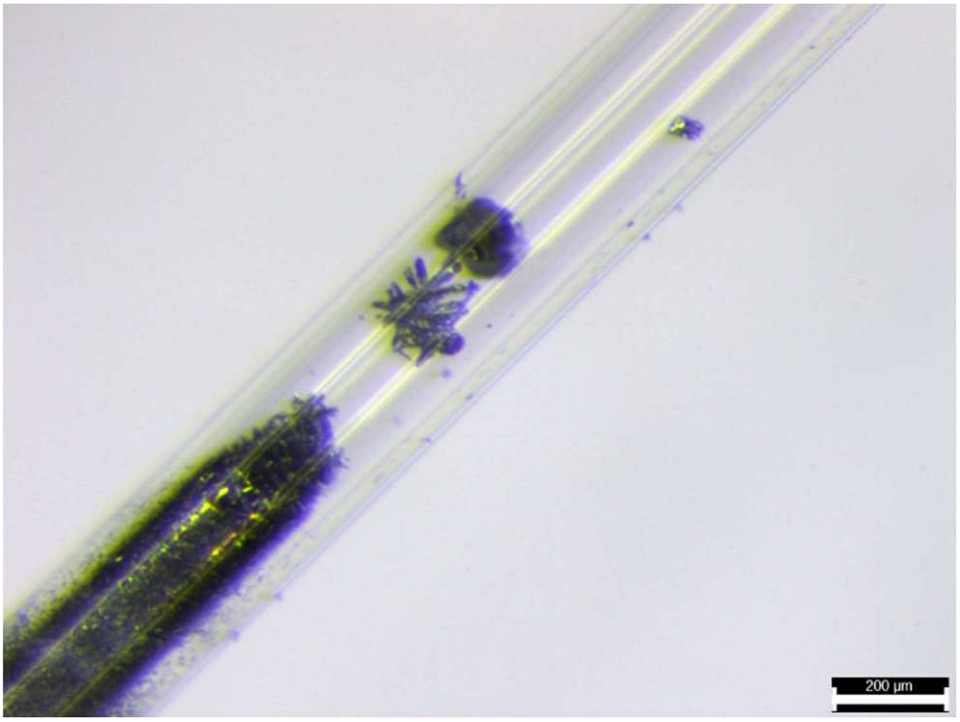

Author: Paul Sicher BSc

Supervision:

Privatdoz. Dipl.-Ing. Dr. techn. Berthold Stöger

Vienna, 17 January 2023 Paul Sicher

Abstract

Thermoelectric materials are a subject of current research because they can convert waste heat to electrical energy. Sulfosalts are especially suitable for these applications because they show a low thermal conductivity due to their complex and disordered structures. Through substitution of S with Se or Te an increase in electrical conductivity can be achieved which results in better thermoelectric performance.

The aim of our research was the synthesis and structural characterisation of new selenide compounds in the systems Cu-Pb-Sb-Se and Cu-Pb-Bi-Se. By using single crystal x-ray diffraction, the structures were not only determined at room temperature but also at elevated temperatures. The syntheses were conducted in evacuated fused silica ampules at 950 °C and 600 °C with the respective selenides serving as starting materials.

A family of three structures with a common andorite-like high-temperature structure at 400 °C was found (space group *Cmcm*, cell parameters about 4 Å, 14 Å and 20 Å) with a stoichiometry of about $CuPbSb_3Se_6$. These different structures resulted from a commensurate superstructure in $P2_1/c$, another commensurate superstructure in $Cmc2_1$ and an incommensurate superstructure in *Cmcm*(*α*00)00*s*. The two commensurate structures were found intergrown in single crystals and separately, too. Additionally, one polymorphous structure in *Pnnm* was discovered.

Pavonites were found with Sb and Bi, these had similar Cu disordering around the centre of an octahedron in their structures with cross-shaped electron densities or different tetrahedral arrangements. Cannizzarite-like compounds known to literature could be synthesised as well, alongside an interesting new composite structure containing Bi_2Se_3 and Cu_2Se_2 layers.

Kurzfassung

Thermoelektrika sind Gegenstand aktueller Forschung, da sie Abwärme in elektrische Energie umwandeln können. Sulfosalze eignen sich besonders für diese Anwendungen, da sie aufgrund ihrer komplexen und fehlgeordneten Struktur eine niedrige thermische Leitfähigkeit aufweisen. Darüber hinaus kann durch Substitution von S durch Se oder Te eine Erhöhung der elektrischen Leitfähigkeit erzielt werden, was die thermoelektrische Leistungsfähigkeit erhöht.

Ziel unserer Forschung war es, neue Selenidverbindungen in den Systemen Cu-Pb-Sb-Se und Cu-Pb-Bi-Se zu synthetisieren und deren Struktur aufzuklären. Mittels Einkristalldiffraktometrie wurden die Strukturen nicht nur bei Raumtemperatur bestimmt, sondern auch die strukturellen Veränderungen bei höheren Temperaturen analysiert. Die Synthese wurde in evakuierten Quarzglasampullen bei 950 °C und 600 °C durchgeführt, Ausgangsstoffe waren die jeweiligen Selenide.

Eine Familie dreier Strukturen mit einer gemeinsamen andoritartigen Hochtemperaturstruktur bei 400 °C (Raumgruppe *Cmcm*, Zellparameter etwa 4 Å, 14 Å, 20 Å) mit der ungefähren Stöchiometrie $CuPbSb_3Se_6$ wurde entdeckt. Dazu wurden eine zweifache Überstruktur in $P2_1/c$, eine dreifache Überstruktur in $Cmc2_1$ und eine inkommensurable Struktur in *Cmcm*(α00)00*s* gefunden. Die zwei kommensurablen Strukturen wurden in separaten Einkristallen und orientiert verwachsen in denselben Einkristallen mit Hauptreflexen an den gleichen Positionen gefunden. Zusätzlich wurde eine polymorphe Struktur in der Raumgruppe *Pnnm* aufgeklärt.

Pavonite wurden sowohl mit Sb als auch mit Bi gefunden, diese hatten ähnliche Fehlordnungen von Cu-Atomen um das Zentrum eines Oktaeders. Das äußerte sich in kreuzförmigen Elektronendichten oder komplexen tetraedrischen Anordnungen. Literaturbekannte cannizzaritartige Verbindungen konnten im Bi-System gemeinsam mit einer anderen zusammengesetzten Struktur gefunden werden. Letztere bestand aus Bi_2Se_3- und Cu_2Se_2-Schichten.

Danksagung

An dieser Stelle möchte ich mich bei allen bedanken, die mich bei der Erstellung dieser Arbeit unterstützt haben. Zuvorderst gilt dieser Dank meinem Betreuer, Berthold Stöger, für die intensive Betreuung bei der ganzen Arbeit von der Synthese bis zum Verfeinern und von der Themenfindung bis zur Abgabe.

Darüber hinaus gilt mein Dank dem Röntgenzentrum für die Bereitstellung eines großartigen Arbeitsumfeldes. Dies betrifft die Hilfsbereitschaft des Technikers Werner Artner genauso wie die organisatorische Unterstützung durch Klaudia Hradil und Angelika Graumann. Auch für die fachlich interessanten Diskussionen mit Erich Halwax und meinem Diplomandenkollegen Tobias Wolflehner möchte ich mich bedanken.

Für die Unterstützung bei der Synthese und die fachliche Anleitung im Labor der Strukturchemie gilt mein Dank Matthias Weil. Ohne seine Mithilfe wäre der Prozess deutlich komplexer gewesen. Ebenso möchte ich seinem Dissertanten Felix Eder für die Unterstützung bei der Bedienung der Geräte des Röntgenzentrums danken.

Zu guter Letzt möchte ich die Gelegenheit nutzen, Dan Topa für seine Vorarbeiten zu diesem Thema und die Messung meiner Proben an der Mikrosonde des Naturhistorischen Museums Wien zu danken.

Contents

1 Introduction

Sulfosalts are a diverse mineral group consisting of different structure types that have very little in common. One of these structure types is the lillianite homologous series which is characterised by the double-capped trigonal prismatic coordination of Pb and octahedral coordination of other atoms in PbS-type slabs. This rather complex structure results in low thermal conductivities which makes these sulfosalts candidates for use as thermoelectric materials. Inhibiting sulfosalts from wider use in thermoelectrics is their low electric conductivity. This can be mitigated by substituting sulphur for selenium or tellurium. Although this substitution rarely occurs in nature because of the higher abundance of sulphur in nature (480 ppm vs 0.8 ppm for selenium and 0.01 ppm for tellurium) [1], it is very easy to do in synthesis because the starting materials can be chosen. Historically, the go-to materials for thermoelectric generators were PbTe and Bi_2Te_3 [2], but with tellurium being scarce and selenium-based thermoelectric materials being on par with their heavier analogues [3], selenides seem promising.

A recent (unpublished) investigation by Dan Topa of the Museum of Natural History in Vienna revealed several unidentified compounds in the Cu-Pb-Bi-Se system which makes the system an excellent ground for searching new selenide compounds. Because of the availability of starting materials, it was decided that the Cu-Pb-Sb-Se system should be investigated first.

1.1 Sulfosalts

According to the sulfosalt sub-committee of the IMA Commission on Ore Mineralogy, sulfosalts are a chemically heterogenous group of chalcogenide (S^{2-}, Se^{2-}, Te^{2-}) minerals that can be seen analogous to oxysalts, although the actual structure of salts with complex thioanions is more complicated than the one of complex oxoanions. [4] Further classification inside the sulfosalt group is generally done by using structure types, some of which are detailed in this introduction because they are relevant to this thesis.

1.1.1 Lillianite

The structure of lillianite ($Pb_3Bi_2S_6$) was first solved with synthetic analogues in 1968 [5] and in 1972 with natural samples, where disordering of lead and bismuth was shown [6]. The structure is orthorhombic with space group *Cmcm* and consists of [PbS_8] in double-capped trigonal prismatic coordination and [(Bi,Pb)S_6] octahedra. In their publication, Takagi and Takéuchi describe the structure in the non-standard spacegroup *Bbmm* with cell parameters *a* = 13.535(3) Å, *b* = 20.451(5) Å, *c* = 4.104(1) Å. [6] In *Cmcm*, *c* would be *a*, *a b* and *b c*. The [(Bi,Pb)S_6] octahedra are summarised into PbS-type slabs which are oriented in two different ways with a layer of [PbS_8] between them, see Figure 1.

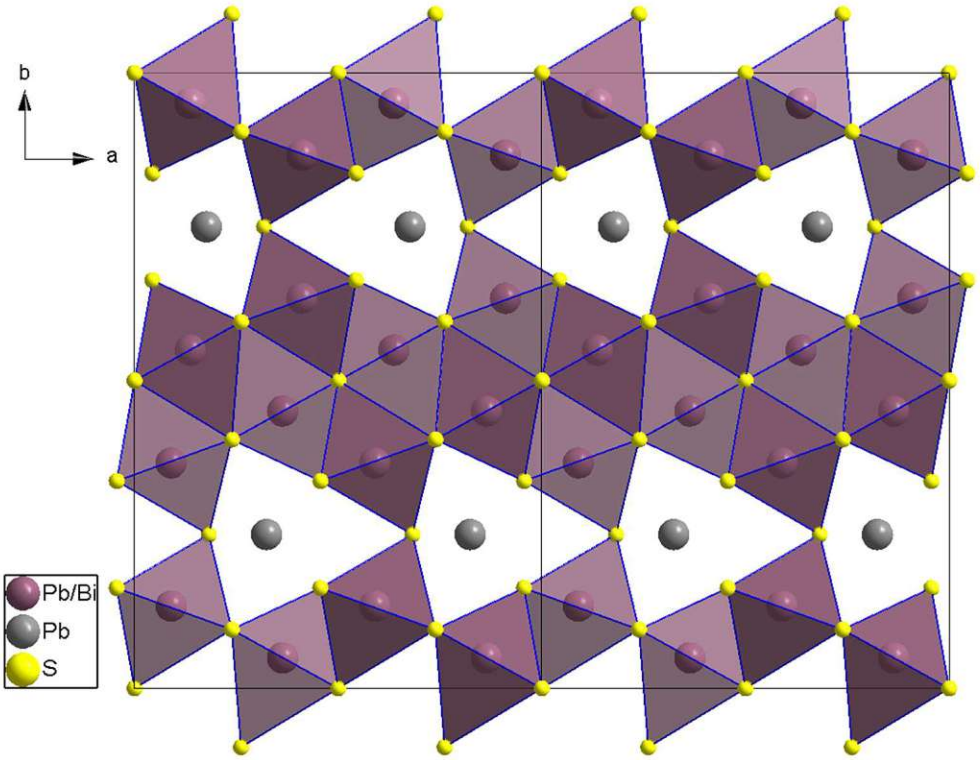

Figure 1: The structure of lillianite minerals, projection on (100) was created with structural data from [6]

In 1977, Makovicky and Karup-Møller established a nomenclature to describe lillianite-like structures by using two Parameters N_1 and N_2 and the symbol L (short for lillianite). [7] The N parameters stand for the number of edge-connected octahedra in a PbS-type slab counted on the longer diagonal of the slab. As a shorthand for homologues where $N_1 = N_2$, the notation ^{N}L was introduced alongside $^{N1,N2}L$. This shorthand however was absent in a similar publication in 1981. [8]

Generally, if every slab has the same thickness N, the structure is orthorhombic or monoclinic in case of cation ordering. If differently orientated slabs have different thicknesses, the structure will be monoclinic or triclinic in case of cation ordering. [9] For this thesis the nomenclature $^{N1,N2}L$ will be adhered to if the PbS-slabs are different. For orthorhombic structures with equivalent slabs, the notation ^{N}L seems sufficient. This is in line with the IMA report which describes the orthorhombic lillianite as ^{4}L and the monoclinic xilingolite [10] as $^{4,4}L$, even though the case of inequivalent slabs of equal thickness is not outlined in the explanation of the nomenclature. [4] Recent literature concerning synthetic lillianite compounds deviates somewhat as orthorhombic lillianite-like structures are described as $^{N,N}L$ [11], [12].

1.1.2 Andorite

While andorite ($AgPbSb_3S_6$) has a lillianite-like structure, it contains Sb instead of Bi and is thus expected to be closer to the structures in the Cu-Pb-Sb-Se system. While the structure itself is lillianite-like, the PbS-type slabs are deformed by the presence of lone electron-pair micelles. Additionally, in contrast to lillianite phases containing bismuth, extended solid solution fields are not observed, only a substitution range of a few percent. [9]

Andorites can be classified by their deviation from the sum formula $AgPbSb_3S_6$. A parameter *n* is determined by multiplying *x* in $Ag_xPb_{3-2x}Sb_{2+x}S_6$ by 100 and written as And_n. [4] This nomenclature is used to classify andorite homologous minerals by the frequent substitution 2 Pb ↔ Ag + Sb.

The andorite mineral from which the sum formula $AgPbSb_3Se_6$ is derived from is senandorite (previously known as andorite VI) where the number six in the name stands for the sixfold superstructure in the direction of the shortest cell parameter (*c* in *Bbmm* or *a* in *Cmcm*). There is also a variant with a fourfold superstructure called quatrandorite with a sum formula corresponding to $And_{93.75}$. [4] The structure of senandorite is shown in Figure 2 in the same projection as lillianite was shown in in Figure 1. A detailed description of the structure is given in [13].

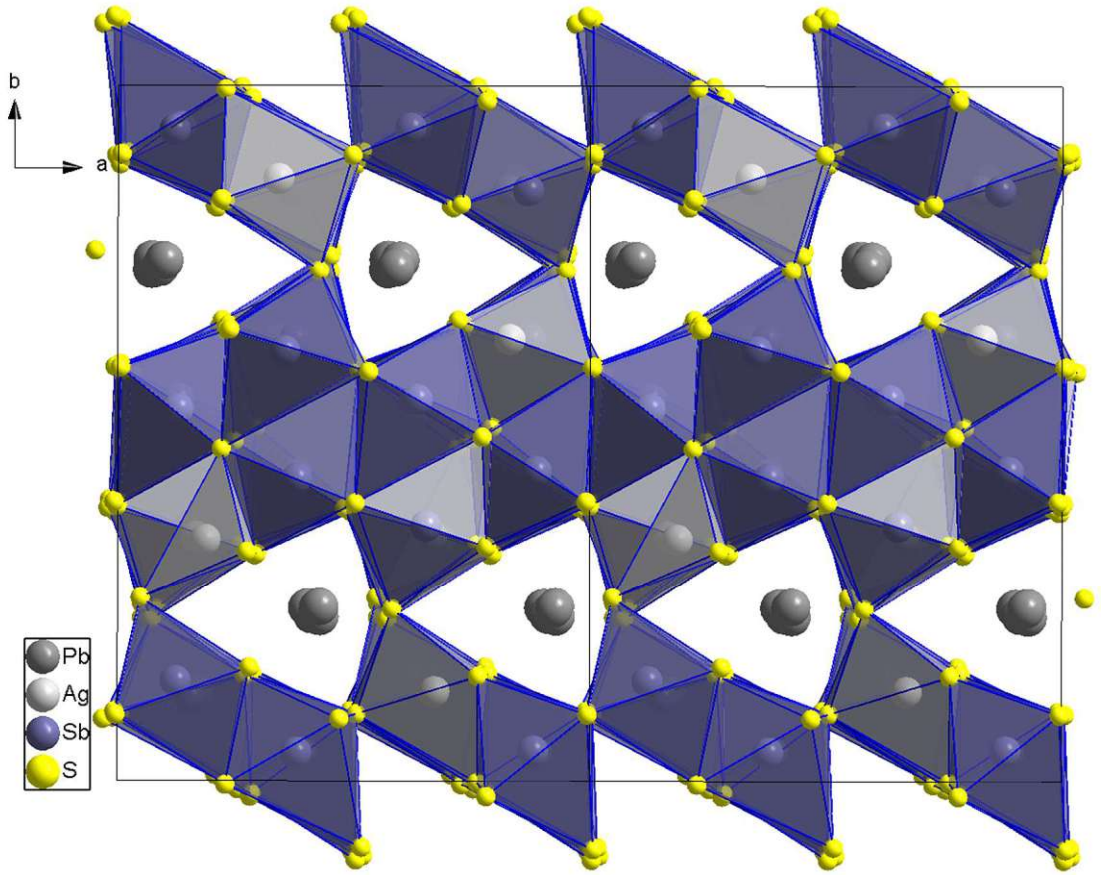

Figure 2: Senandorite structure projected onto (001) with structural data from [13]

1.1.3 Pavonite

The monoclinic structure of pavonite ($AgBi_3S_5$) consists of two different layers, one PbS-like slab with octahedrally coordinated Ag- and Bi-positions and one thin layer with paired [BiS_5] square pyramids and one [AgS_6] octahedron as depicted in Figure 3. The pavonite homologous series varies in the thickness of the PbS-like slab. Just like in lillianite, the thickness of the slab is determined by the number N of edge-connected octahedra along the longer diagonal and the symbol P (for pavonite). The structure of $AgBiS_5$ would thus be denoted as ^{5}P. [8]

The pavonite homologous series is structurally close to the lillianite homologous series as the square pyramids can also be seen as deformed double-capped prisms when three additional S-atoms from the PbS-layer are seen as part of the coordination polyhedron as well. If the single octahedron in the thin layer is seen as a PbS-slab with N=1, a member of the pavonite homologous series ^{N}P could also be viewed as a member of the lillianite homologous series ^{1,N}L. [8]

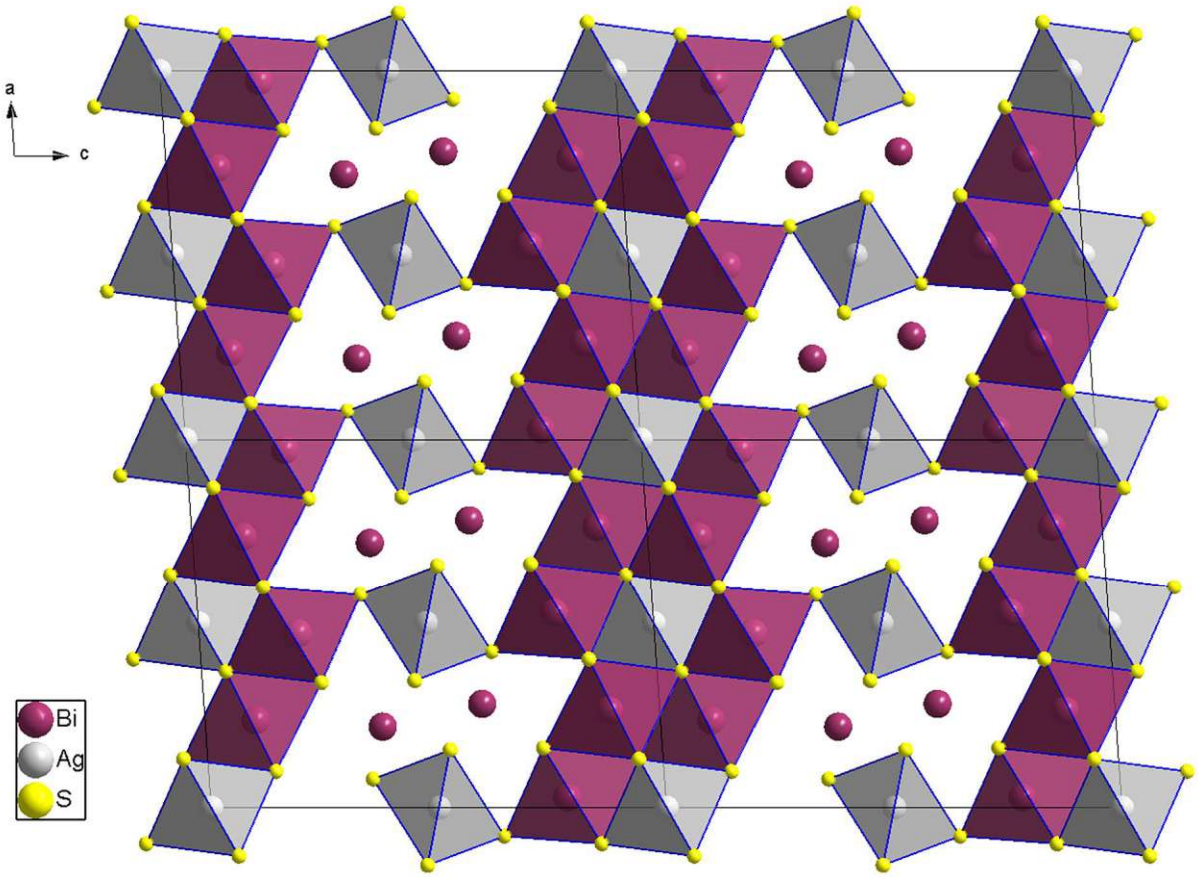

Figure 3: Crystal structure of synthetic pavonite projected onto (010) drawn with structural data from [14]

1.1.4 Cannizzarite and Wittite

Departing from lillianite-related minerals, cannizzarite and wittite are composite layer structures consisting of (Pb,Bi)(S,Se) and $(Bi,Pb)_2(S,Se)_3$ subsystems. The metal atoms of the first subsystem are coordinated in square pyramids while the second, thicker subsystem only contains octahedrally coordinated positions (see Figure 4).

Cannizzarite is the mineral name for S-rich compounds while wittite would be used for Se-rich ones. From a crystallographic point of view, both minerals consist of these sublattices and show disordering regarding both S and Se and Pb and Bi which makes them barely distinguishable. However, in the field of mineralogy, it is heavily debated whether these minerals should be distinct or not. [4], [15]

Numerous studies have been conducted to determine the disordering of the sites, the result of one of them is shown in Figure 4. [16] One study investigated cannizzarite by using resonant

data to differentiate Bi from Pb, however, with estimated standard uncertainties of about 0.1 for site occupancy factors, it did not ultimately solve this problem. [17]

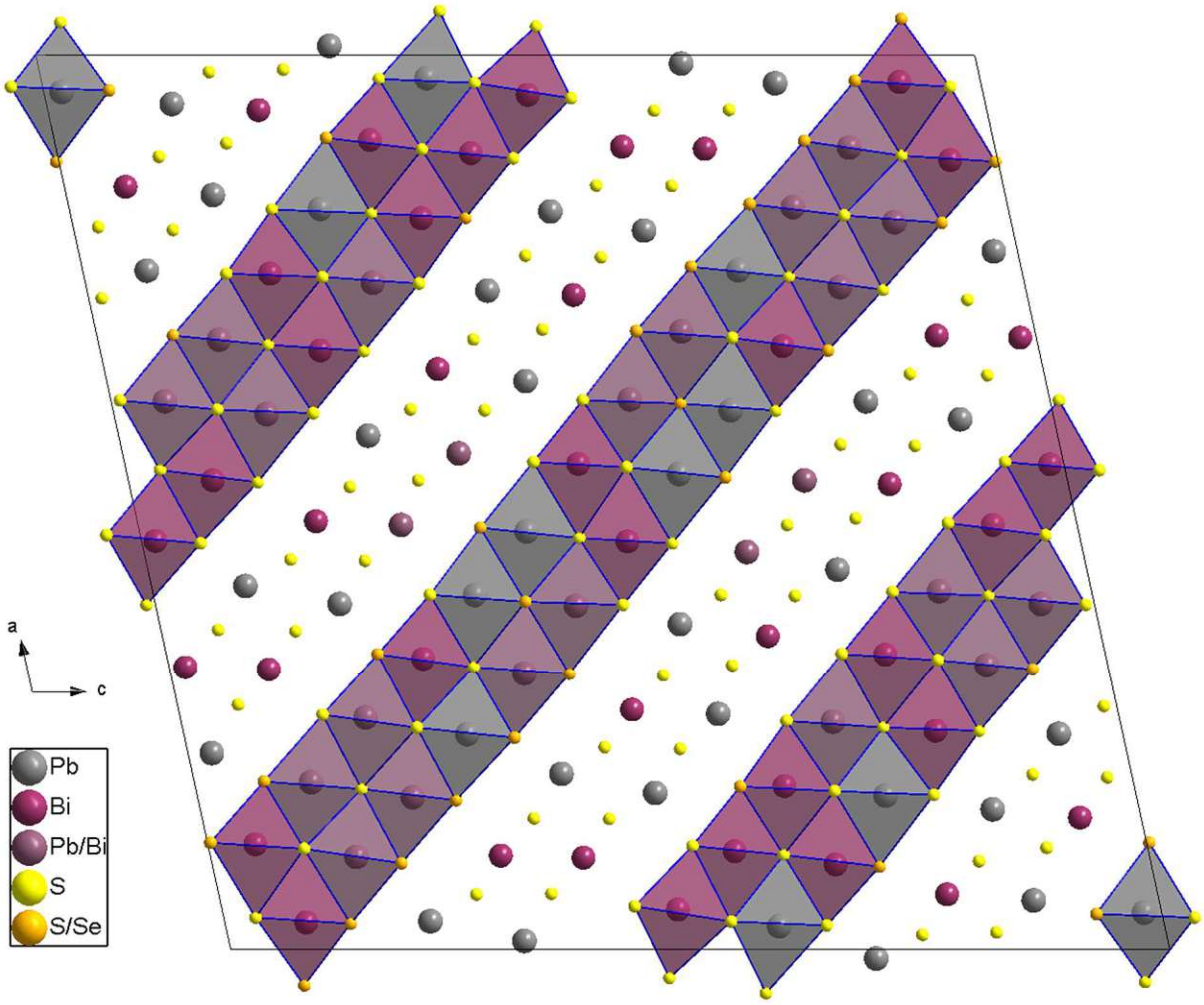

Figure 4: Crystal structure of cannizzarite as determined by [16]

1.2 Thermoelectric Effect

Waste heat is an underutilised resource for generation of power. An easy way to use the otherwise lost energy is converting it to useable electricity. This can be done by thermoelectric generators or heat machines while the former have the advantage of not consisting of moveable parts and thus being less intensive regarding maintenance. A big disadvantage of thermoelectric generators is their low performance in converting heat to electricity.

1.2.1 Figures and Formulae

Thermoelectric materials are assessed with the dimensionless figure of merit ZT which is given by:

$$ZT = \frac{S^2\sigma}{\kappa}T \qquad \text{(eq. 1)}$$

S is the Seebeck coefficient, σ the electrical conductivity, κ the thermal conductivity (all three material constants) and T the temperature. The energy conversion efficiency η_{TE} is given using ΔT for the temperature difference, T_{ave} as the average temperature, T_{hot} as the temperature on the hot side and T_{cold} as the temperature on the cold side:

$$\eta_{TE} = \frac{\Delta T}{T_{hot}} \cdot \frac{\sqrt{1 + ZT_{ave}} - 1}{\sqrt{1 + ZT_{ave}} + \frac{T_{cold}}{T_{hot}}} \qquad \text{(eq. 2)}$$

This must be contrasted to the conversion efficiency of a heat machine, using Carnot's theorem:

$$\eta_{Carnot} = 1 - \frac{T_{cold}}{T_{hot}} = \frac{\Delta T}{T_{hot}} \qquad \text{(eq. 3)}$$

For an infinitely big ZT, the second factor in eq. 2 equals 1 and η_{TE} becomes η_{Carnot}. However, since no heat machine can actually operate at Carnot's efficiency because no heat machine can operate reversibly, ZT does not have to be infinite to be competitive in terms of conversion efficiency. A figure of merit between two and three would be enough to outcompete even the most efficient heat machines which would be modern diesel engines with a conversion efficiency of about 40% of η_{Carnot} (see visualisation in Figure 5). Materials with figures of merit of this size have already been found. [18] However, ZT also depends on the operating temperature as the material constants used for its calculation are temperature dependent.

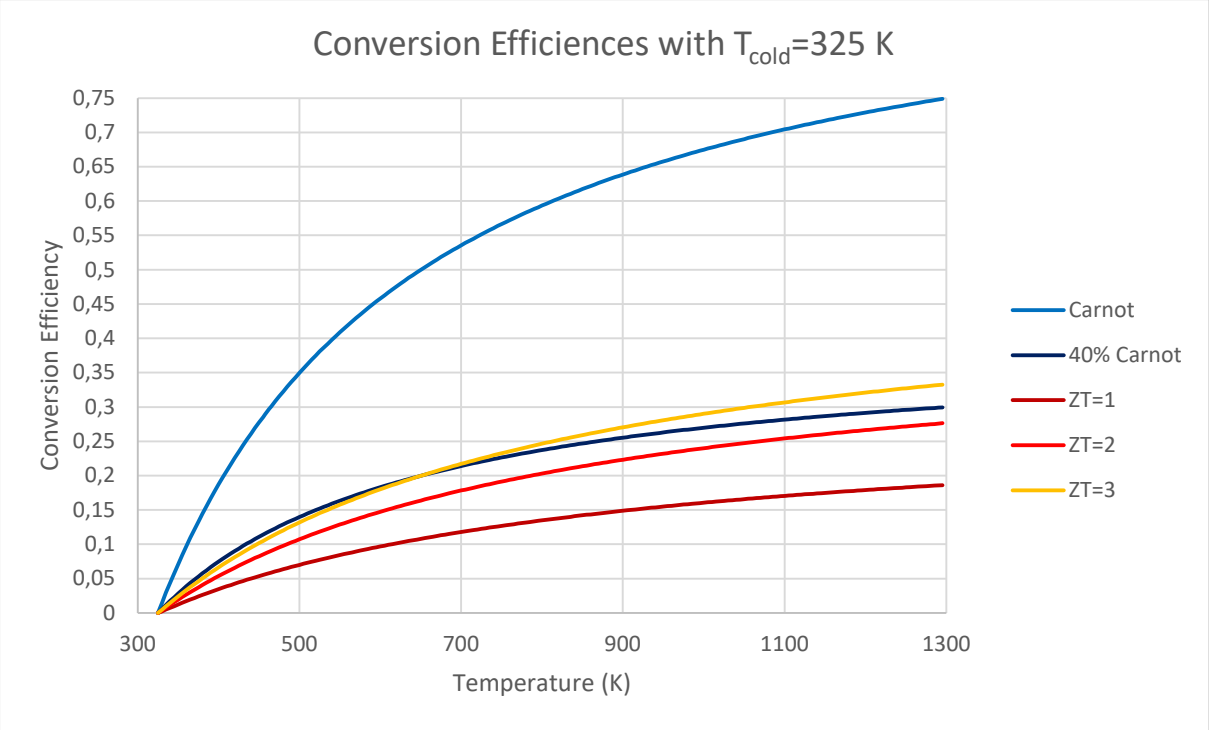

Figure 5: Comparing conversion efficiencies of thermoelectric materials with different ZT with conversion efficiencies in Carnot heat engines

1.2.2 Increasing the Figure of Merit

Increasing this figure is not easy as an increase in electrical conductivity will result in an increase in thermal conductivity according to the Wiedemann-Franz law [19] (eq. 5):

$$\kappa = \kappa_{lattice} + \kappa_{electrons} \quad \text{(eq. 4)}$$

$$\kappa_{electrons} = L\sigma T \quad \text{(eq. 5)}$$

The total thermal conductivity consists of $\kappa_{lattice}$ which is determined by phonons and $\kappa_{electrons}$ which quantifies heat transport by electrons and holes (eq. 4). However, $\kappa_{electrons}$ grows with the electrical conductivity σ (L is the Lorenz factor, a constant). Therefore, $\kappa_{lattice}$ has to be minimised by inhibiting heat transport via phonons through the crystal structure. Its value depends on the heat capacity (C_v), the phonon velocity (v) and the mean free path of the phonon (l):

$$\kappa_{lattice} = \frac{1}{3} C_v v l \quad \text{(eq. 6)}$$

While the first two are material constants, the last parameter can be influenced by point defects, nano-scale precipitates and grain boundaries. [2]

Alternatively, materials with intrinsically low thermal conductivities are available. These show large molecular weights, complex crystal structures, anharmonic or anisotropic bonding, weak chemical bonding or ion liquid-like transport behaviour. [2] Especially relevant to this thesis is the last point as Cu_2Se is a superionic conductor [20] and the second point as sulfosalt structures are complex.

1.3 Superstructures

For a comprehensive review of modulated structures, see the IUCr monograph on incommensurate crystallography by Sander van Smaalen. [21]

If a cell consists of two or more similar building blocks that vary only slightly, e. g. the element occupying a certain position, it can be described as a superstructure of a basic structure with a smaller cell. Often, superstructures disappear at higher temperatures in order-disorder phase transitions. Positions or occupations previously ordered by the superstructure then become disordered.

When determining a superstructure via single crystal x-ray diffraction, it makes sense to differentiate between main reflections and satellites. The main reflections correspond to a hypothetic structure with an averaged unit cell, while the less intense satellites contain information regarding the superstructure. By using modulation wave vectors, the positions of satellites can be described relative to the main reflections with fractional coordinates relative to the basic cell. By ignoring the satellite reflections and solving the structure by integrating

only the main reflections' intensities, the superstructure is averaged and obtained as an average structure.

1.3.1 Commensurate Case

Commensurate superstructures are periodic structures where the volume of the primitive cell is a multiple of the volume of the primitive basic structure cell. The modulation vector is therefore a fractional part of a reciprocal lattice vector. For example, in the simple case of a twofold superstructure in the [100] direction, additional satellite reflections appear at the midpoint between main reflections. The satellite reflections can be indexed by a modulation wave vector of $\boldsymbol{q} = \frac{\boldsymbol{a}^*}{2}$. Expressed with respect to the reciprocal basis the q-vector is represented by the coordinates (1/2, 0, 0). Commensurate structures are characterized by rational **q**-vector coordinate components.

Symmetry reductions frequently occur with the introduction of commensurate superstructures and do not have to be visible in the diffraction pattern, e. g. a structure in *Cmcm* affected by **q** = (2/3, 0, 0) can crystallise in the space group type $Cmc2_1$. Sometimes, even changes in the lattice symmetry are induced by modulation wave vectors. This is common for vectors with more than one non-zero component, e. g. the same *Cmcm* structure, now affected by **q** = (1/2, 1/2, 0), will have a monoclinic diffraction pattern.

1.3.2 Incommensurate Case

Incommensurate superstructures cannot be simply described with bigger unit cells because the periodicity of the basic structure and the modulation functions are not related by a rational number. For every main reflection, satellites are observed following the respective modulation wave vector. The satellite at the end of the vector starting at a main reflection is considered a first order satellite, if the vector is followed again, second order satellites are reached. Similar to main reflections, where the intensity of the reflections decreases exponentially with the *h*, *k*, and *l* coordinates, the intensities of the satellite reflections decrease with their order. Thus, depending on the employed x-ray source and the quality of the crystal typically only the first few orders of satellite reflections are observed. Otherwise, the diffraction pattern would appear as dense. For a rigorous treatment of diffraction patterns of aperiodic crystals, see "Aperiodic Order" by Baake and Grimm. [22]

1.3.3 Internal Space

Incommensurately modulated structures are conveniently described by embedding them in (3+d)-dimensional superspaces where d can range from 1 to 3. Even though the structures are not periodic in three-dimensional physical space, they can be considered periodic in the higher-dimensional superspaces. [23] The whole electron density of the incommensurately modulated structure is contained in a single (3+d)-dimensional unit cell. The (3+d)-superspace contains the 3D physical space and the d-dimensional internal space. Coordinates are called x_n with n ranging from 1 to 3+d. While the diffraction pattern is a projection of a (3+d)-dimensional

pattern onto physical space, the electron density in physical space is a section of the electron density embedded in superspace. Contrary to the superspace, this section lacks translational symmetry. Figure 6 gives an example of a superspace interpretation of an incommensurately modulated structure.

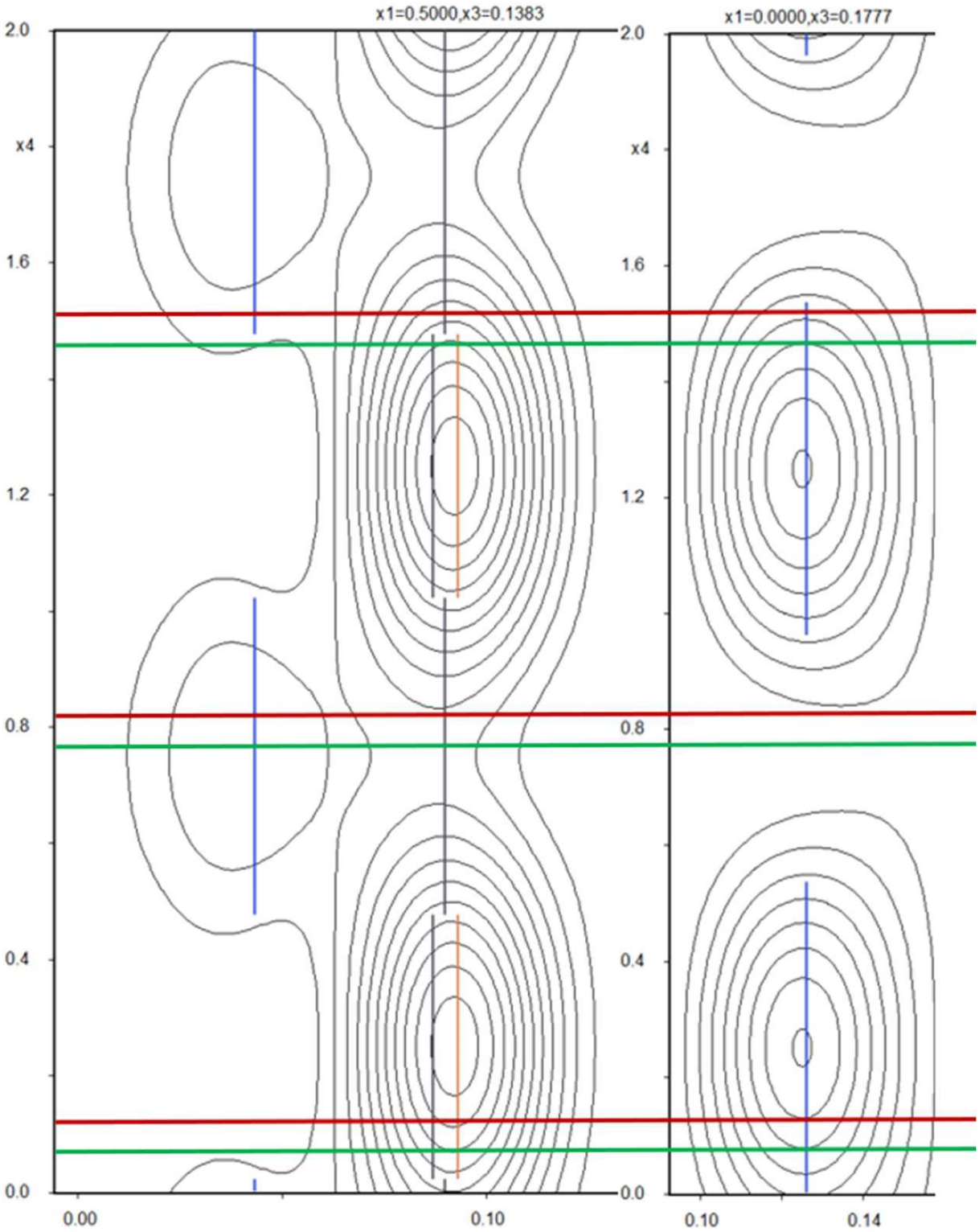

Figure 6: Practical example of an intersection of a (3+1)-dimensional superspace. The contours represent the electron density, the coloured vertical lines atom positions and the coloured horizontal lines show where part of the section runs through to define the atoms of six unit cells in real space.

The standard *hkl*-indices do not suffice for the description of both main reflections and satellites. Therefore, the additional indices *m*, *n* and *o* are introduced who signify how often a modulation wave vector was applied from the main reflections *hkl*000. For internal spaces with two or one dimension, *o* or *o* and *n* are superfluous. Satellite order generally is defined as the sum of |*m*|, |*n*| and |*o*|. Further distinguished are single and mixed satellites: a satellite with the indices *hkl*200 would be called a single second order satellite, one with indices *hkl*110 a mixed second order satellite.

1.3.4 Superspace Groups

Just as the symmetry of periodic crystal structures is expressed through space group types, the symmetry of incommensurate crystal structures is expressed through superspace group types. The superspace groups are a subset of the (3+d)-dimensional spacegroups, because internal space cannot be mapped onto physical space. They are derived from the symmetry of the main reflections because every symmetry operation is retained in some form. This must be case as crystals with an incommensurate superstructure do not exhibit special physical properties because of this property of their superstructure.

The modulation wave vector is considered as well because the modulation of different coordinates produces different structures. Some symmetry operations may have an intrinsic translational component in the internal space directions. For example, a 2_1 screw axis could become a (2_1, *s*) screw axis where *s* denotes a movement along x_4 by 1/2. Other symbols would be *t* for a translational component of 1/3, *q* for 1/4 and *h* for 1/6.

These three aspects are encoded in the symbol of a superspace group the following way: First the Hermann-Mauguin-symbol for the space group of the basic structure, then in brackets the modulation vector, whereby the incommensurate components are denoted by the Greek letters *α*, *β*, and *γ* for the different directions and last the presence or absence of translational components in x_4 where 0 stands for absence and the respective symbol for presence. An example of a superspace group would be *Cmcm*(*α*00)00*s*.

2 Experimental

The experimental part involved synthesising new sulfosalt compounds using the selenides Cu_2Se, PbSe, Sb_2Se_3 and Bi_2Se_3 and determining their structure with single crystal x-ray diffraction (SCXRD). While SCXRD was performed at different temperatures, no measurements of materials properties were conducted. This was done to limit the scope of this thesis, although the measurements would have been questionable anyway as it was not yet possible to synthesise pure phases. In order to aid the determination of the structure and to obtain information about different phases in the samples, electron probe micro analysis (EPMA) was employed.

2.1 Synthesis

Selenides decompose at moderate temperatures to form the respective oxides. Because the temperatures for the synthesis were chosen to be as high as 950 °C, the samples had to be prepared under either inert gas atmosphere or vacuum. Since the preparation of compounds in evacuated fused silica ampules works well for small amounts of product and is an established method in the research group, it was used to prepare all the samples in this thesis.

Generally, commercially obtained Cu_2Se, PbSe and Sb_2Se_3 or self-synthesised Bi_2Se_3 were mixed in different ratios and transferred into ampules, which were sealed with an oxyhydrogen burner after evacuation. The evacuated ampules were heated to 950 °C for homogenisation of the educts, held there for a short amount of time, cooled to 600 °C within 7 h, tempered at 600 °C for a long amount of time and cooled slowly to 200 °C over variable times. The motivation not to adhere to a strict temperature program was to investigate how crystal quality would vary by changing time periods in the program. An optimal program from previous studies was not available.

2.1.1 Samples with Sb_2Se_3

The obtained ingots were inhomogeneous; however, single crystals could be obtained by crushing them and selecting crystals by using single crystal diffraction. In Table 1, the masses of the selenides and the time periods are denoted. Cooldown time stands for the amount of time used to cool the ampules from 600 °C to 200 °C. In the “Identified Crystals” column, new phases are denoted with abbreviations that will also be used in the headers of the respective chapters in the results section. Three abbreviations are used for andorite-type structures with different modulations: 2x for the twofold commensurate variant, 3x for the threefold commensurate variant and ic for the incommensurate variant. 2x/3x is used for an oriented intergrowth of phase of 2x and 3x. oP is used for an unrelated orthorhombic primitive structure and SbP for a pavonite-type structure.

Table 1: Overview of syntheses conducted with Cu_2Se, PbSe and Sb_2Se_3

Sample	Cu_2Se (mg)	PbSe (mg)	Sb_2Se_3 (mg)	Ratio (Cu:Pb:Sb)	Time at 600 °C (h)	Cooldown time (h)	Identified Crystals
2G	25.0	72.0	62.0	0.96:1:1.03	*	*	PbSe, ic, 3x
4	18.8	48.0	122	1.09:1:3.02	99	16	2x/3x, 2x, 3x, oP
5	16.7	93.5	81.9	0.50:1:1.04	99	16	PbSe
6	4.6	103.4	83.0	0.12:1:0.96	99	16	PbSe
7	18.9	48.9	170	1.07:1:4.14	149	5	Sb_2Se_3, 2x
8	18.6	47.0	200	1.10:1:5.07	149	5	Sb_2Se_3
9	12.2	32.8	163	1.03:1:5.92	149	5	Sb_2Se_3
10	40.0	47.6	125	2.33:1:3.13	149	5	oP
11	22.7	67.6	117	0.93:1:2.06	96	6	ic

12	21.7	66.9	100	0.90:1:1.78	96	6	ic
13	21.9	59.9	125	1.02:1:2.48	96	6	ic
14	21.2	59.1	101	1.00:1:2.04	**	-	
15	18.8	25.3	122	2.06:1:5.75	192	1	
16	28.9	24.0	182	3.34:1:9.05	192	1	SbP
17	19.2	0	186	1:0:4.15	44	12	Sb_2Se_3
18	21.5	15.1	178	3.95:1:14.1	44	12	Sb_2Se_3
19	29.4	12.4	183	6.59:1:17.5	192	20	Sb_2Se_3, SbP
20	19.4	11.6	184	4.65:1:18.9	192	20	Sb_2Se_3

* 3h to 800 °C, 48h at 800 °C, to 200 °C over 12 h
** taken out at 950 °C and quenched in water

2.1.2 Samples with Bi_2Se_3

For this system, the same method and educts were used. In contrast to the other selenides, the employed Bi_2Se_3 was not obtained commercially but synthesised. Under the same conditions as samples 15 and 16, 1 g of a 2:3 (n/n) mixture of Bi and Se with 5% excess of Se were heated in an evacuated quartz ampule. The crushed product appeared as a pure phase in a powder diffractogram. The product of another synthesis without Se excess was impure.

In this system, in addition to the ingot, several crystals grown along the fused silica ampule were obtained. These were investigated separately from the ingots and did not contain any Cu. As was done for samples prepared with Sb_2Se_3, abbreviations are introduced for each new phase: Bi4P for a ^{4}P pavonite-type structure, Bi4P_ic for an incommensurate variant of Bi4P, Bi6P for a ^{6}P pavonite-type structure, Cann1 and Cann2 for two different cannizzarite-type structures and DiSe for a novel diselenide. The masses of the used selenides and the exact reaction conditions are summarised in Table 2.

Table 2: Overview of syntheses conducted with Cu_2Se, PbSe and Bi_2Se_3

Sample	Cu_2Se (mg)	PbSe (mg)	Bi_2Se_3 (mg)	Ratio (Cu:Pb:Bi)	Time at 600 °C (h)	Cooldown time (h)	Identified Crystals
51	10.2	45.4	130	0.62:1:2.5	192	20	Cann1
51A	Ingot from sample above						
52	10.0	27.6	194	1.01:1:6.15	220	1	Bi4P
52A	Ingot from sample above						
53	41.7	115	69.5	1.01:1:0.53	220	1	
53A	Ingot from sample above						Bi6P
54	15.2	14.7	146	2.87:1:8.70	220*	2*	CuBiSeO, Bi_2O_2Se
55	15.5	15.4	148	2.80:1:8.41	990	2	
55A	Ingot from sample above						Bi4P, Bi4P_ic

56	23.5	62.8	151	1.04:1:2.10	990	2	
56A	Ingot from sample above						
57	15.2	21.9	150	1.93:1:5.98	990	2	Cann2
57A	Ingot from sample above						DiSe

* reaction in air-filled ampule due to preparation error, homogenisation at 800 °C

2.2 Single Crystal X-Ray Diffraction

The prime method for determining crystal structures is single crystal x-ray diffraction (SCXRD). It was employed to screen the samples by determining the unit cells of crystals and if the cell did not match any known cell in the inorganic structure database (ICSD) [24] or that known cell corresponded to a structure that did not solely contain the elements used for the synthesis, a full data collection was performed.

Sample mounting was done with Kapton-micromounts by MiTeGen using the perfluorinated polyether Fomblin or the more viscous NHVO-1. Measurements generally were conducted at 300 K regulated by an Oxford Cryosystems Cryostream 800.

The instrument used for all measurements was a STOE Stadivari equipped with a Dectris EIGER 1M CdTe detector and a Mo microsource by Axo with a K_α-wavelength of 0.71073 Å. Data analysis was carried out using the manufacturer's software X-Area and absorption correction performed with LANA [25].

2.3 Refinement

ShelXT [26] was used to solve the structures from intensity values using the Olex2 [27] interface. Afterwards, refinement was done with ShelXL [28] using the ShelXle Graphical User Interface [29]. The incommensurately modulated structure was refined with the JANA2020 [30] suite after importing a structure prepared with ShelXT and ShelXL.

The general procedure for refinements was to assume that every Se position was fully occupied by Se. For the andorite-type structures, assuming full occupation by Sb often lead to excess electron density while it was the opposite for Pb. Some positions showed different coordinates for occupational disordering of Sb and Pb. In this case, the total occupancy was restrained to 1, whereas the coordinates of both atoms were refined freely. For atoms in the centre of [(Pb,Sb)Se_8] polyhedra, both the coordinates and the atomic displacement parameters (ADPs) usually had to be restrained to the same values. Sometimes, ADPs had to be restrained if one of the atoms' ADPs were non-positive definite (NPD) after a refinement cycle.

2.4 High-temperature SCXRD

For x-ray measurements at higher temperatures, our standard method for mounting crystals with polymer loops and oil is not viable. Instead, crystals had to be mounted with fused silica

capillaries with a diameter of 0.2 mm. To prevent oxidisation, these capillaries were filled with Ar before sealing them with a CH_4/O_2 burner.

For heating the crystals on the goniometer, the STOE HeatStream was used. This device heats the samples with a hot N_2 gas stream and is useable from room temperature up to 800 °C. The heating was controlled via the voltage which was calibrated using a thermoelement. From 160 °C to 590 °C increasing the voltage of the heater had a linear impact on temperature change (see Figure 7). The calibration was checked with KNO_3, Ag_2SO_4 and K_2CrO_4 powders filled in capillaries because they undergo solid phase transitions at 128 °C, 430 °C and 587 °C, respectively. All the powders behaved as expected and underwent a phase transition after the voltage was set to a point that corresponded to a slightly higher temperature than the phase transition points. The diameter of the gas stream was slightly below 2 mm which was determined after a part sublimation of a crystal and its resublimation in the cold area (see Figure 8). The crystal decomposed during the process, only PbSe remained in the hot area.

2.5 Electron Probe Microanalysis

In addition to SCXRD, the elemental compositions of our samples were measured using an electron microprobe (JEOL JXA 8530F) in WDS mode, at 25 kV, 20 nA, 2 µm beam diameter with selenide and metal standards and ZAF correction procedure.

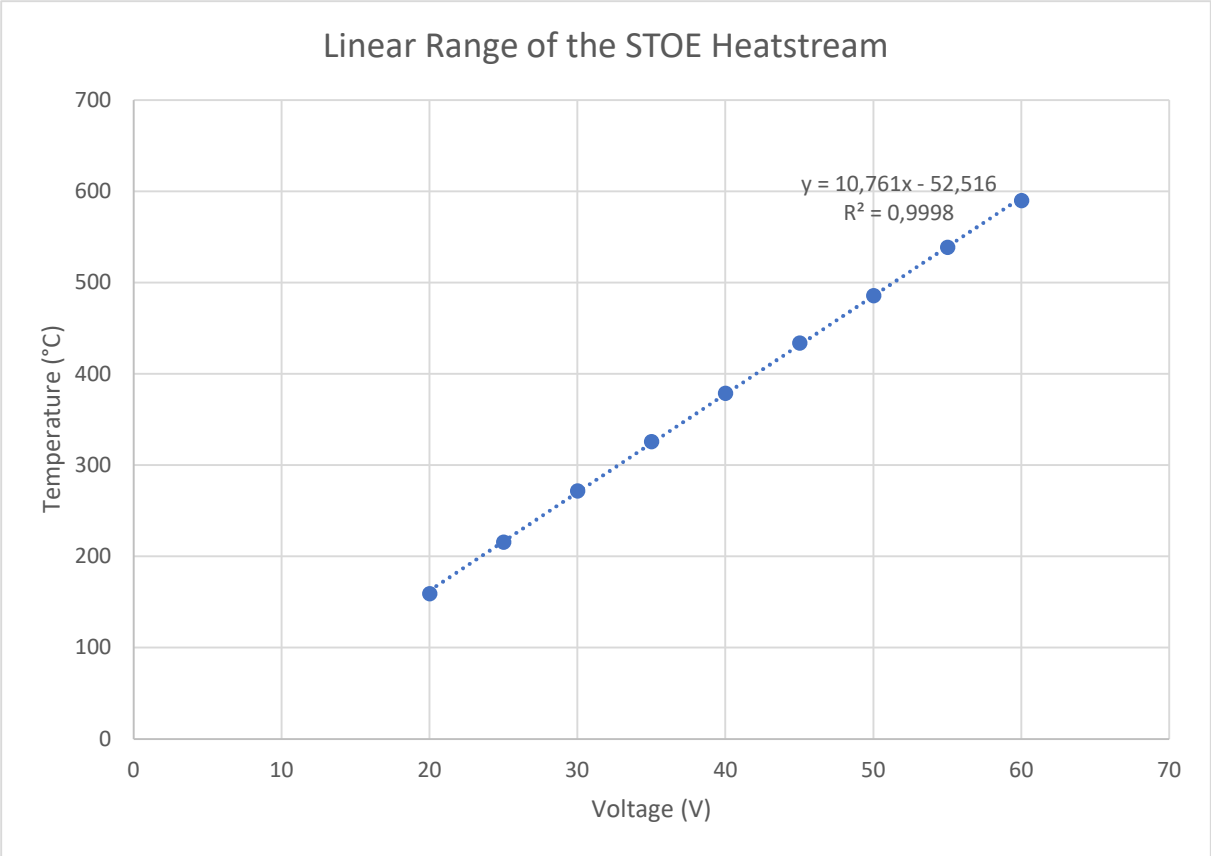

Figure 7: Calibration curve of the Heatstream used for high-temperature SCXRD measurements

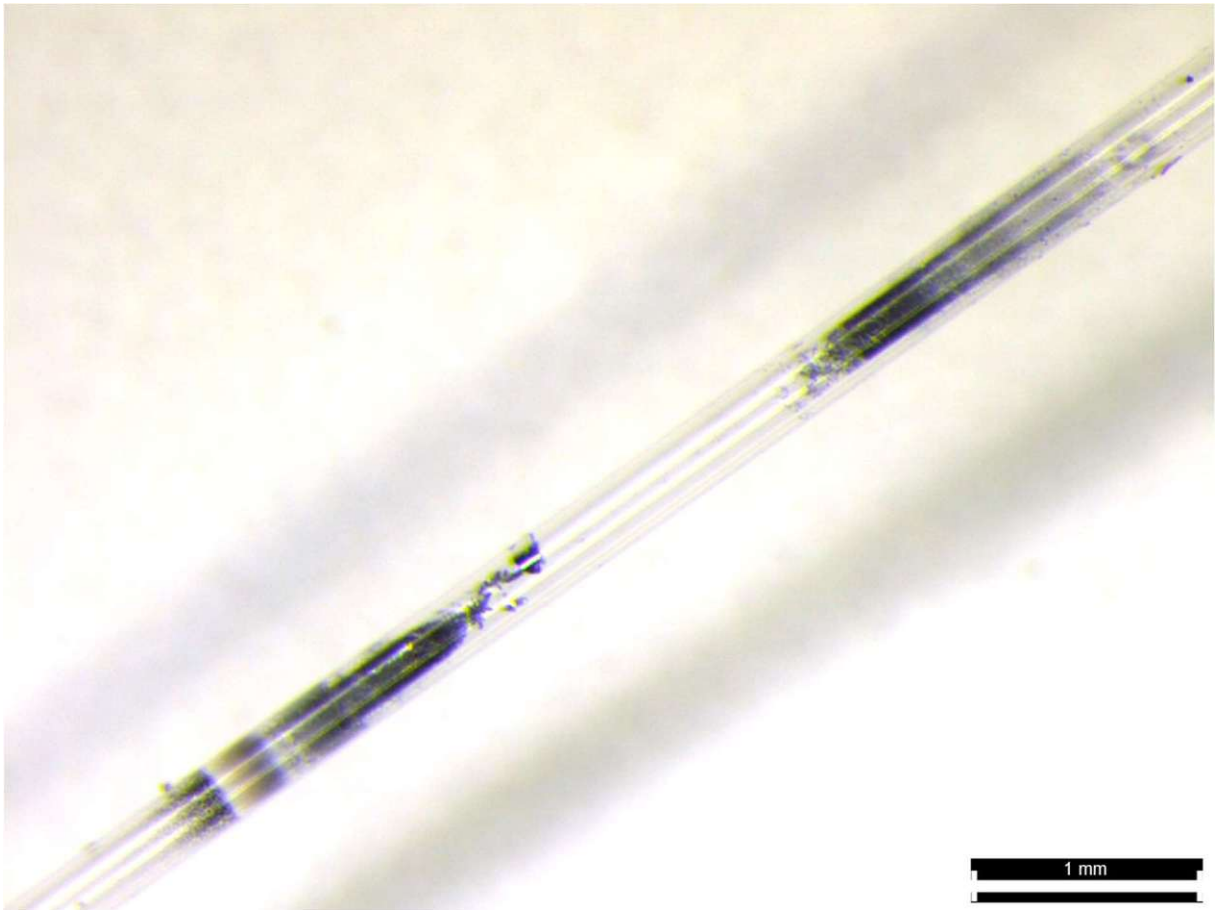

Figure 8: Capillary after decomposition of a crystal: The clear section is where the capillary was heated

3 Results

The resulting structures will be grouped by their mineral analogues which were discussed in the introduction.

3.1 Andorite-type Structures

Because the general composition of the following compounds ($CuPbSb_3Se_6$) is very similar to the one of andorite ($AgPbSb_3S_6$) and they mostly show the same structural features, they are referred to as andorite-type structures. However, they do not follow the general substitution 2 Pb ↔ Ag + Sb or in this case 2 Pb ↔ Cu + Sb. This is especially valid for the Pb-rich incommensurate structure where the charges are balanced by an interstitial Cu-position. Similar to natural andorite minerals, these synthetic compounds exhibit superstructures.

At room temperature, three different modulated superstructures of the same basic structure were found: two commensurate structures and one incommensurate structure. High-temperature SCXRD measurements have been conducted and all the modulated superstructures exhibited an order-disorder phase transition that led to a common high-temperature structure which corresponds to the basic structure. The transformation temperature is different for each structure, however. An exceptional find was a crystal that did only show weak diffuse satellites at room temperature and was thus used to refine a basic structure at room temperature.

3.1.1 Basic Structure

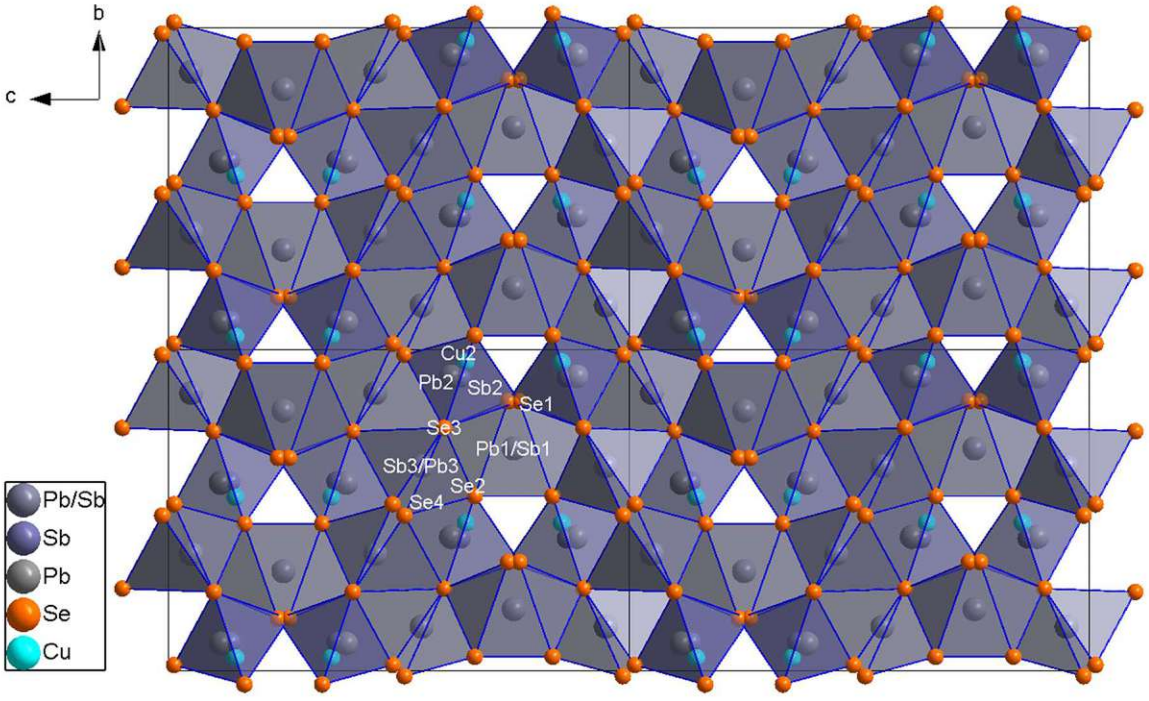

Figure 9: Common basic structure of the andorite-type phases projected on (100) with labeled atoms

The basic structure refined from a crystal with diffuse satellites showed cell parameters of *a* = 4.1535(2) Å, *b* = 13.9911(6) Å and *c* = 20.0727(13) Å and crystallises in the space group *Cmcm* at 300 K. Because of the small parameter *a*, the structure can be understood from a (100)-projection such as the one shown in Figure 9. There are three different metal positions occupied by two (Pb1/Sb1 and Sb3/Pb3) or three (Sb2/Cu2/Pb2) atoms and four different selenium positions, two of which are disordered around a symmetry element: Se1 around m_{001} and Se4 around 2_{100}.

Just like in the structure of lillianite, there are two different coordination polyhedra: the double-capped trigonal prism [(Pb,Sb)Se_8] and the octahedron [(Sb,Pb)Se_6]. For the position of Cu2, the polyhedron can be viewed as the same octahedron seen for Sb2 and Pb2 with Cu2 displaced from the centre or as a tetrahedron with two Se-atoms being no longer included in the coordination polyhedron. In any case, this andorite-type structure would be classified as ^{4}L since the slabs are 4 octahedra thick and are equivalent resulting in an orthorhombic symmetry.

The stoichiometry from refinement of this crystal worked out to $Cu_{0.636}Pb_{1.173}Sb_{3.191}Se_6$; however, it is not certain that this is the correct elemental composition for this crystal since it could not be referenced with any other data. The charge balance is far from neutral with 4.6% more positive charge than negative charge from Se^{2-}.

3.1.2 Twofold Commensurate Structure (2x)

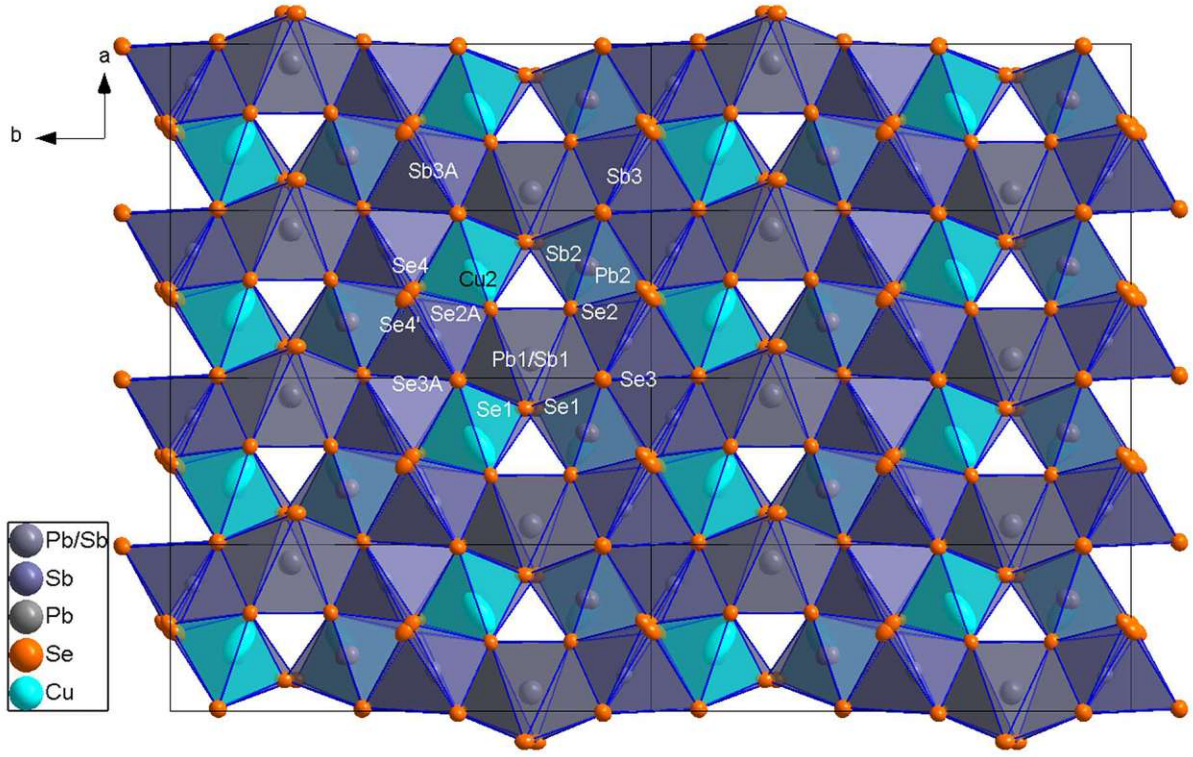

Figure 10: Twofold superstructure viewed down [001] drawn with 90%-ellipsoids

This superstructure transforms the orthorhombic basic structure into a monoclinic one with the modulation wave vector $\mathbf{q}_{2x}$ = (1/2, -1/2, 0) which orders the Sb2/Cu2/Pb2-position by separating them into a Cu-position and a Sb/Pb-position. The two different thick layers result in a ^{4,4}L andorite-type structure. The cell parameters are *a* = 7.2041(8) Å, *b* = 19.9163(16) Å, *c* = 8.2859(10) Å and β = 106.825(9)° at 300 K with the space group $P2_1/c$. The parameter *a* from the basic structure is doubled, although it is denoted as *c* for this superstructure because the standard space group is used ($P2_1/a$ retains the coordinate system). With a doubled cell size and a halving of point group symmetry (mmm to 2/m), the symmetry is reduced four times. While the Pb1/Sb1-position with its double-capped trigonal prism stays the same, the other positions undergo changes. An overview is shown in Figure 10, for more details see Table 3.

The biggest change is the existence of the Cu2-position that is not disordered with another element (the calculated electron density fits only Cu) and the large atomic displacement parameters (ADPs) of the Cu2-atom. The position of Sb3/Pb3 in the basic structure is split in Sb3 and Sb3A while the disordering of the position with Pb atoms is not observed here. Similarly, Se2 and Se3 now have to be modelled as Se2 and Se2A and Se3 and Se3A, respectively. This is different for the positions of Se1 and Se4 since they were disordered around symmetry elements in the basic structure. Because the symmetry element m_{010} was lost, it now occupies both positions in one unit cell. The same could have been observed for Se4 since 2_{001} is not retained as well, instead the Se4 position stays disordered with the symbol Se4' being used to denote the second position. The disordering differs from the basic structure as four different positions are visible from [001]. 84(3)% of the Se-atoms are situated on Se4 with the 16(3)% following the position modelled as Se4'. An overview of these positional differences from [100] is shown in Figure 11. The ordering of the Sb2/Cu2/Pb2-position of the basic structure to two separate positions becomes more apparent there as well.

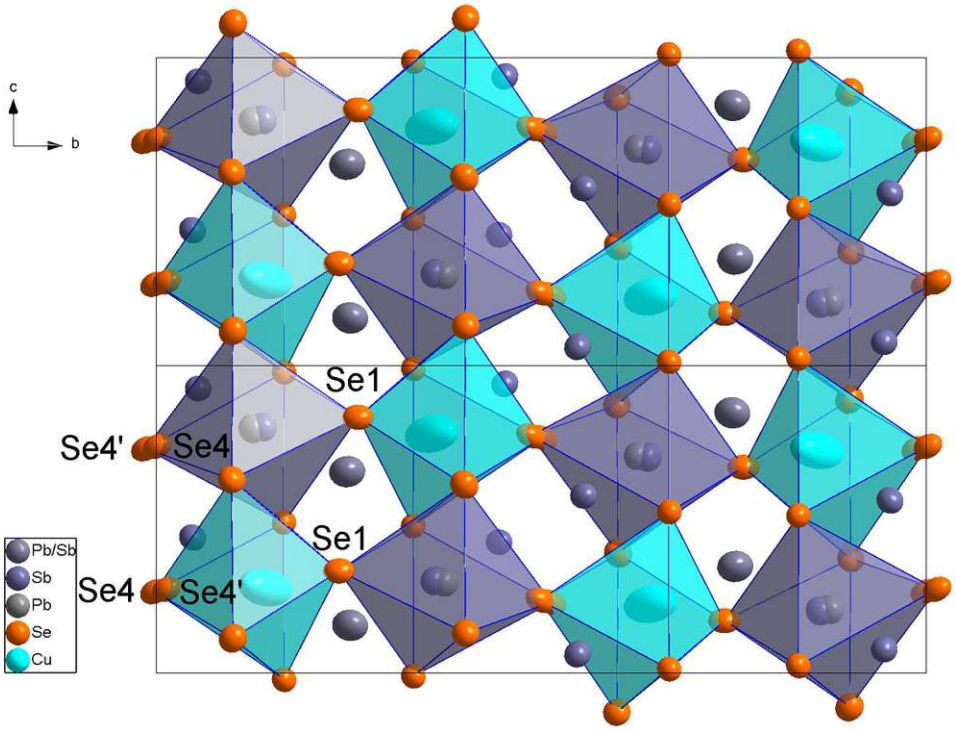

Figure 11: Twofold superstructure viewed down [100] with some Se-positions labelled

Table 3: Crystal data for the twofold superstructure

Crystal data	
Chemical formula	$CuPbSb_3Se_6$
M_r	1109.79
Crystal system, space group	Monoclinic, $P2_1/c$
Temperature (K)	300
a, b, c (Å)	7.2041(8), 19.9163(16), 8.2859(10)
β (°)	106.825(9)
V (Å^3)	1138.0(2)
Z	4
Radiation type	Mo $K\alpha$
μ (mm^{-1})	42.74
Crystal size (mm)	0.03 × 0.03 × 0.02
Data collection	
Diffractometer	STOE STADIVARI
Absorption correction	Multi-scan, STOE LANA
T_{min}, T_{max}	0.395, 0.553
No. of measured, independent and observed [$I > 2\sigma(I)$] reflections	16645, 4489, 1635
R_{int}	0.155
$(\sin \theta/\lambda)_{max}$ (Å^{-1})	0.793
Refinement	
$R[F^2 > 2\sigma(F^2)]$, $wR(F^2)$, S	0.040, 0.068, 0.74
No. of reflections	4489
No. of parameters	110
No. of restraints	1
$\Delta\rho_{max}$, $\Delta\rho_{min}$ (e Å^{-3})	2.72, −2.39

The reason for the existence of this separate Cu-position is probably the stoichiometry. The sum formula works out to be exactly $CuPbSb_3Se_6$, which marks a significant increase in Cu content from the basic structure described above. In principle, twinning should occur for crystals of this superstructure as it is possible for another modulation vector $\mathbf{q}'_{2x}$ = (1/2, 1/2, 0) to exist alongside $\mathbf{q}_{2x}$. This was not the case for crystals form our syntheses, although twins were obtained during high-temperature examinations (see chapter 3.1.5).

3.1.3 Threefold Commensurate Structure (3x)

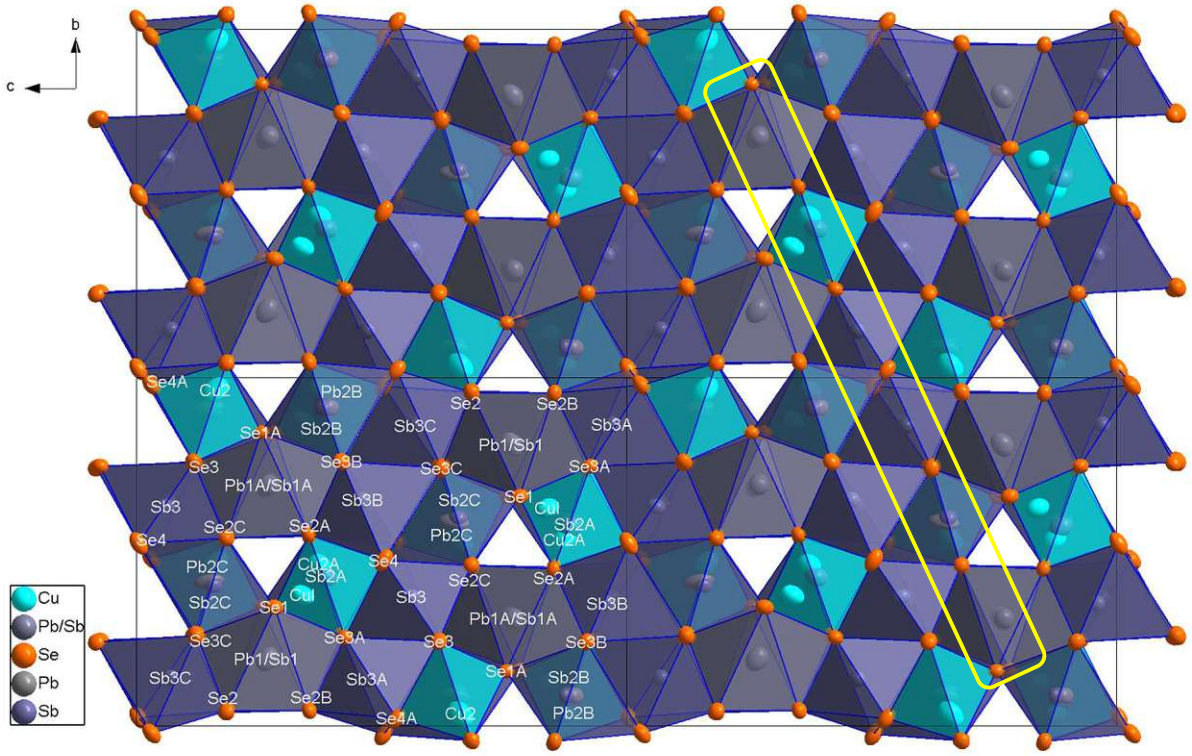

Figure 12: Threefold superstructure projected onto (100) drawn with 90% ellipsoids, the equivalent of the yellow marked area is shown in another projection in Figure 13

In this superstructure $\mathbf{q}_{3x}$ = (2/3, 0, 0) is responsible for a tripling of the cell parameter *a* of the basic structure and the transformation of the space group *Cmcm* to *Cmc*2_1 where the threefold superstructure crystallises in. Since the point symmetry is halved (mmm to mm2) and the cell volume tripled, it is considered a six-fold symmetry loss. The positions explained for the basic structure are split up to two or four different positions. Still, this structure is denoted as a ^{4}L andorite-type structure because the PbS-slabs are equivalent. The lattice parameters are *a* = 12.3821(3) Å, *b* = 14.0182(4) Å and *c* = 19.7551(8) Å at 300 K, for more details see Table 4. A (100)-projection is pictured in Figure 12, a depiction of the positions along [100] can be seen in Figure 13.

Regarding coordination polyhedra, Pb/Sb-positions still have a coordination number of 8 with [(Pb,Sb)Se_8] double-capped trigonal prisms and Sb- and Sb/Pb-positions still coordinate octahedrally in PbS-slabs. However, there is now an interstitial Cu-position that unambiguously forms [$CuSe_4$] tetrahedrons instead of [$CuSe_6$] pseudo-octahedrons (see Figure 14).

Most positions from the basic structure are split into four different ones. With the exceptions of Pb1/Sb1, Se1 and Se4, every original position now needs to be described by four different positions. One doubling is needed because of the loss of the reflection plane parallel to (001) of the *Cmcm* symmetry, the other one is required by the tripled lattice parameter *a*. This tripling of *a* could cause a tripling of the positions but does not because of symmetry: The m_{100} reflection plane runs through the atom positions Pb1/Sb1, Cu2, Sb2B/Pb2B, Sb3 and Sb3B

and another through Se1A, Se2A, Se3A, Se4A, Se2C and Se3C. These atoms are only repeated once per unit cell while others are repeated twice: once as themselves and once as their mirror image (see Figure 13).

The disordering in this structure is similar to the twofold superstructure in that the Pb1/Sb1 or the Pb1A/Sb1A respectively show the same behaviour. Likewise, the way Cu2 and Sb2C/Pb2C are arranged is identical. The main structural difference lies in the new interstitial CuI-position that sometimes replaces the two adjacent Cu2A/Sb2A-positions like shown in Figure 14. With an occupancy of 0.115(6), CuI is realised in about 5.6% of cases. The probability is half of the occupancy because CuI replaces two positions which together with CuI have an occupancy sum of 2. Cu2A has an occupancy of 0.856(7) and Sb2A one of 0.086(6) which makes this double position mostly occupied by Cu. It is thus not an actual interstitial position although the possibility of CuI being realised alongside Cu2A/Sb2A cannot be ruled out. Since the refinement residuals are lower if the interstitial position is modelled as replacing Cu2A/Sb2A, it is assumed to be more likely that in fact it does.

The other position in the sequence along [100] is occupied by the disordered atoms Sb2B and Pb2B with occupancies of 0.950(10) and 0.025(5) respectively. These occupancies still sum up to 1 because the occupancy of Pb2B has to be doubled, because Pb2B can exist on two slightly different positions around the Sb2B-position due to its disordering around the (100) reflection plane.

Furthermore, the disordering of the Se4-position in the way it is observed in the basic structure or the twofold superstructure with the Se4- and Se4'-positions is not observed in the threefold superstructure. Instead, Se4 is ordered as Se4 and Se4A with both positions having full occupancy just like Se1 and Se1A.

The stoichiometry from the refinement is given as $Cu_{11.31}Pb_{12.15}Sb_{36.54}Se_{72}$. It would be tempting to correct the stoichiometry to $Cu_{12}Pb_{12}Sb_{36}Se_{72}$, a neutral multiple of $CuPbSb_3Se_6$, by removing Sb2A which would accomplish this goal. However, such modelling attempts led to significant electron peaks between 3.5 and 4 $eÅ^{-3}$ in the difference Fourier map in the centre of two Se-octahedra, one next to Cu2 and one next to Cu2A. Ideally, one would model Cu2 and Cu2A the same way as Cu2 was modelled in the twofold superstructure. However, the residuals are higher when the ADPs of Cu2 and Cu2A are as large as they are for Cu2 in the twofold superstructure. Placing additional Cu-atoms there would be another possibility, however, this does not reflect the crystal chemistry of Cu. Since the charge balance is only tipped slightly with only 0.85% more positive charge than would be expected from the negative charge from Se^{2-}, the structure is described here as-is with a small caveat that some of the occupancies might not be totally accurate or that some disordered positions are not modelled correctly. It is possible that the error is even caused by vacancies which cannot reliably be investigated with SCXRD. Even the refinement of site occupancy factors is imperfect because ADPs and occupancies correlate.

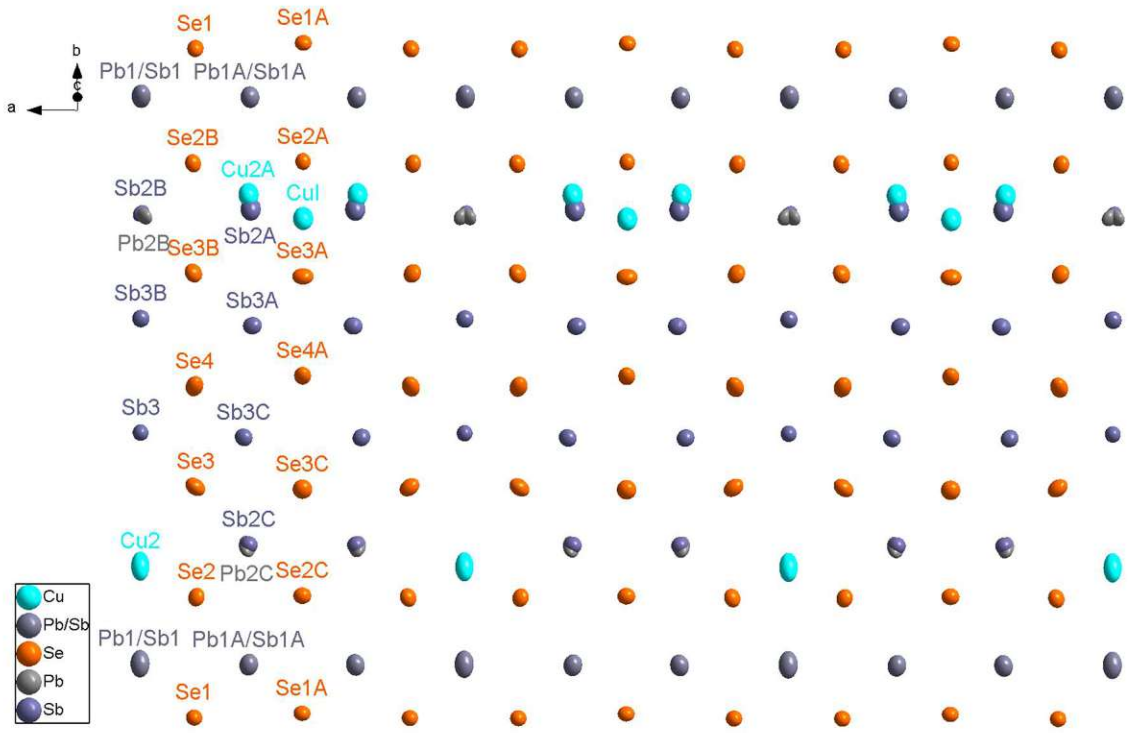

Figure 13: Part of the threefold superstructure projected onto (013) to show the different sequences along [100] drawn with 90% ellipsoids

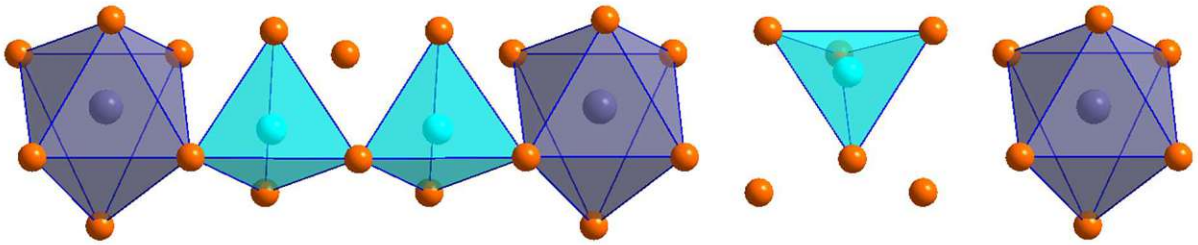

Figure 14: A possible sequence of Sb2B, Cu2A and CuI, highlighting the way CuI was modelled

Table 4: Crystal data for the threefold superstructure

Crystal data	
Chemical formula	$Cu_{11.31}Pb_{12.15}Sb_{36.54}Se_{72}$
M_r	13369.92
Crystal system, space group	Orthorhombic, *Cmc*2_1
Temperature (K)	300
a, *b*, *c* (Å)	12.3821(3), 14.0182(4), 19.7551(8)
V (Å^3)	3428.99(19)
Z	1
Radiation type	Mo *K*α
μ (mm^{-1})	42.74
Crystal size (mm)	0.10 × 0.08 × 0.06

Data collection	
Diffractometer	STOE STADIVARI
Absorption correction	Multi-scan, STOE LANA
T_{min}, T_{max}	0.394, 0.854
No. of measured, independent and observed [$I > 2\sigma(I)$] reflections	29786, 8226, 5943
R_{int}	0.054
$(\sin \theta/\lambda)_{max}$ (Å^{-1})	0.835
Refinement	
$R[F^2 > 2\sigma(F^2)]$, $wR(F^2)$, S	0.043, 0.105, 0.97
No. of reflections	8226
No. of parameters	191
No. of restraints	2
$\Delta\rho_{max}$, $\Delta\rho_{min}$ (e Å^{-3})	3.33, −3.31
Absolute structure	Refined as an inversion twin.
Absolute structure parameter	0.509(12)

3.1.4 Intergrown Commensurate Structures (2x/3x)

In our synthesis experiments, the twofold and threefold superstructures were more commonly found as oriented intergrowths than individually with satellites stemming from both $\mathbf{q}_{2x}$ and $\mathbf{q}_{3x}$. This results in precession images like the one in Figure 15 in which the different reflections are marked for better legibility. The main reflections' intensities of both structures lie on the same points in reciprocal space which means that determining the structures one at a time is not possible. However, Jana2020 is able to refine two phases at the same time while also determining their ratio.

There are structural differences in the refinement of the intergrown phases to the refinements of the pure crystals, the main one being that the interstitial position found in the threefold superstructure is not found in the 2x/3x-phase. Overall, the structures are more ambiguous than those obtained from pure crystals since main reflections are shared. A direct result is the ambivalence of the Pb/Sb-positions in the centres of the double-capped prisms. In principle, every one of these positions in both structures should have the same Pb:Sb ratio. However, if every position is refined with the restrictions that the sum of the occupancies of Pb and Sb must be 1 and that they share the same coordinates as well as ADPs, the Pb1/Sb1-position in the twofold superstructure will have a negative occupancy for Sb1. To solve this, the occupancy was fixed to 0.875 for Pb1 and 0.125 for Sb1, which are values that result in the Pb1/Sb1- and Pb1A/Sb1A-position from the threefold superstructure having similar occupancies which makes most sense. No change in the residuals is observed for changes here since the information about the electron density on these Pb/Sb-positions is extracted from the shared main reflections.

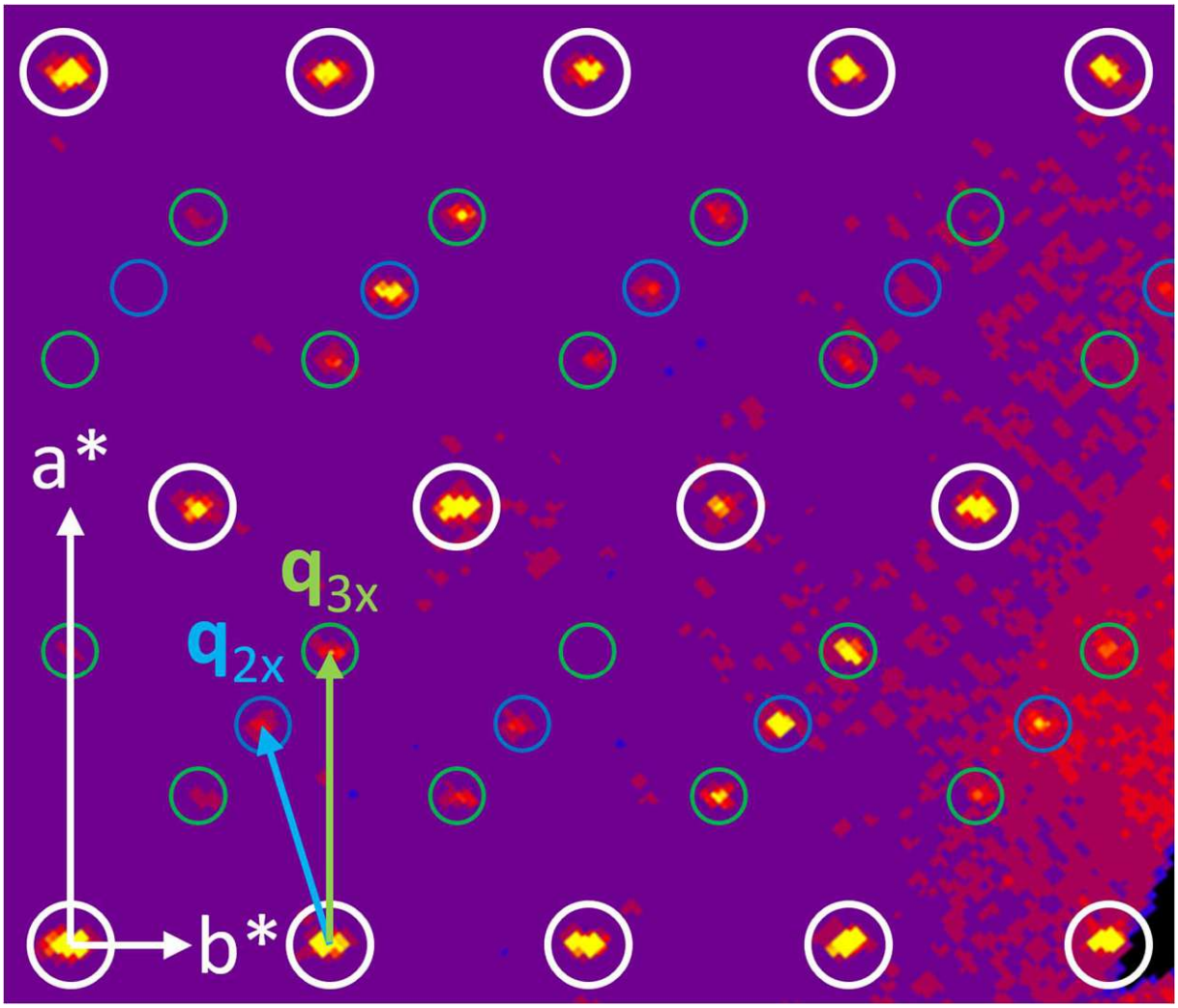

Figure 15: Precession image obtained from an oriented intergrowth of two superstructures in one crystal with the main reflections marked with white circles, the satellites from the twofold superstructures marked with blue circles and satellites from the threefold superstructure marked in green. $\mathbf{q}_{2x}$ and $\mathbf{q}_{3x}$ are the modulation vectors for their respective commensurate structures.

The monoclinic part was refined in a way that would yield a sum formula of $CuPbSb_3Se_6$ which does not only make it neutral but also is most realistic since the structure then has the same composition as the one from the pure crystal. To achieve this, the Sb2/Cu2/Pb2-position from the basic structure was split in the same way as in the 2x-structure. Accordingly, a Cu2-position with large ADPs and a Sb2/Pb2-position were defined. To fit the (arbitrary) occupancies of the Pb1/Sb1-position of 0.875 and 0.125, the same occupancies were defined for the Sb2/Pb2-positions but in reverse; Sb2 has the higher occupancy value. Deviating from the structure obtained from the pure 2x-phase, a Se1'-position analogous to Se4' exists (see Figure 16).

For the refinement of the pure two- and threefold superstructures, no EPMA data was available since the crystals constituted a minority phase. Here, this is different since sample 4 was almost exclusively composed of these 2x/3x intergrown crystals. In Table 5, the data are outlined. While no clear sum formula can be determined since crystals with the same structure do not have the same elemental composition, the averaged results from measuring six phases and 21 points in total show the general direction in which the refinement should head.

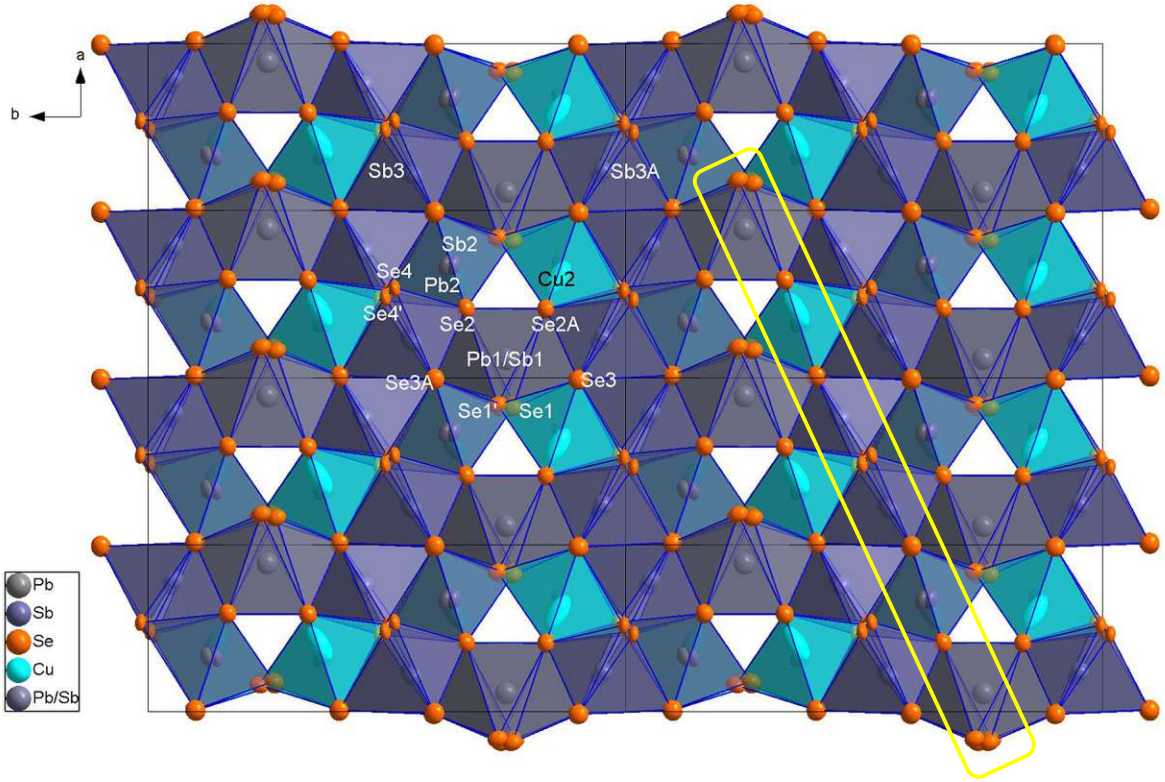

Figure 16: (001)-projection of the monoclinic part of a 2x/3x intergrown phase, the structure along [001] is shown with the marked atoms in Figure 17

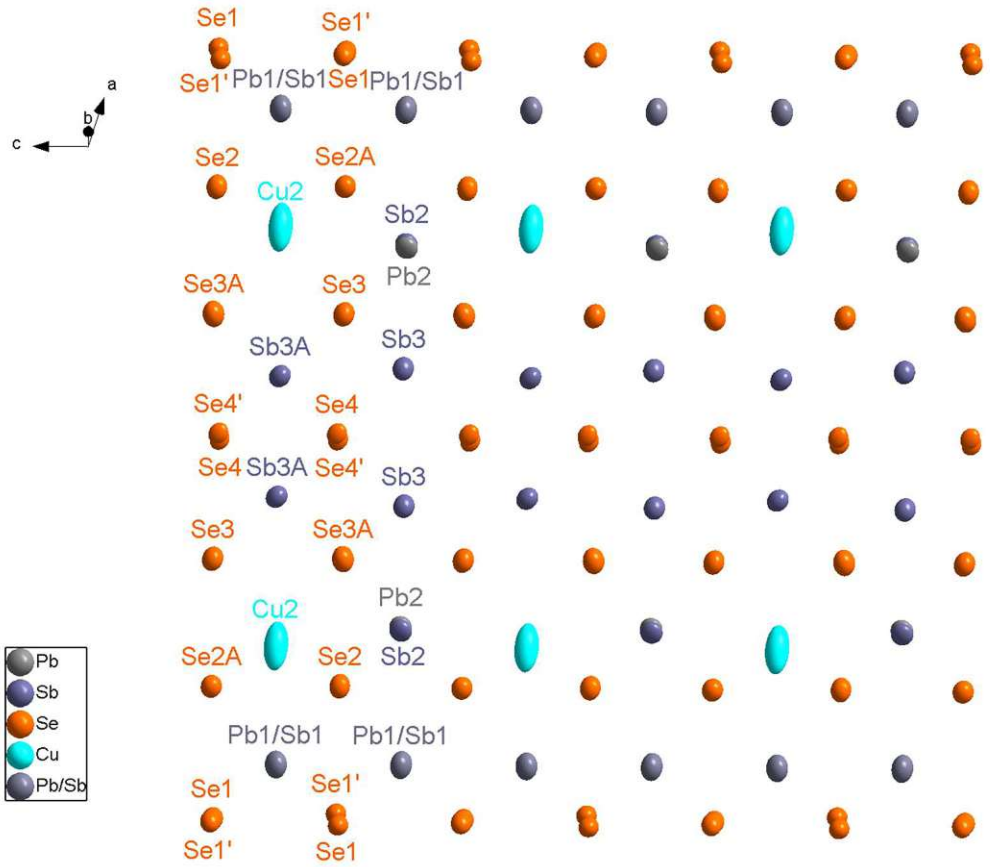

Figure 17: Atoms and labels of the monoclinic part of a 2x/3x intergrown phase between two Pb1/Sb1-positions located as shown with a yellow rectangle in Figure 16

Table 5: EPMA results for sample 4 with charge balance denoting excess positive or negative charge. Mol% values relate to cations only; Se is omitted here.

Grain-Phase	Cu (mol%)	Pb (mol%)	Sb (mol%)	Charge Balance
1-1	19.1(3)	21.9(8)	59.0(5)	1.00%
1-2	20.57(11)	19.0(4)	60.4(5)	0.76%
2-1	21.6(4)	18.5(4)	59.85(13)	0.59%
2-2	19.77(16)	22.84(14)	57.39(11)	-0.08%
3-1	19.1(2)	23.0(2)	57.88(9)	0.20%
3-2	21.49(19)	19.73(18)	58.78(19)	-0.19%
Average	20.4(1.1)	20.7(1.9)	58.9(1.1)	-0.38%

With $CuPbSb_3Se_6$ being set as the sum formula for the 2x-part of the intergrown crystal, the 3x-part's sum formula is expected to look the same way with marginally less Sb and more Cu and Pb from the EPMA data. A first version of our refinement had a sum formula of about $Cu_{0.75}Pb_{0.75}Sb_{3.5}Se_6$ which does not fit the EPMA data at all. After changing the model in a way that would yield less Sb, the here presented structure with the sum formula $Cu_{0.90}Pb_{1.09}Sb_{3.01}Se_6$ was obtained. After combination with the sum formula from the 2x-part of the structure and the information from Jana2020 that 54.8% of our crystal consists of the 3x-part, the sum formula $Cu_{0.94}Pb_{1.05}Sb_{3.01}$ was obtained. With 18.9% Cu, 21.02% Pb and 60.1% Sb, this elemental composition is not far from the EPMA results given in Table 5. The charge balance is tipped by 0.53% more positive charge which is satisfactory.

As mentioned before, the biggest difference in this model to the one used to describe the pure 3x-structure is the missing interstitial Cu-position. Additionally, Sb2A which was disordered with Cu2A is now modelled as a Pb-atom and called Pb2A. Down along [100], Pb2B and Sb2B are now restricted to the same coordinates since their ADPs were too small to warrant them different positions. On the position of Sb3A, an excess of electron density was detected, and the position refined accordingly as Sb3A/Pb3A. In Figure 18 and Figure 19, the structure is depicted with labels, however, they carry the suffix _2 from the refinement due to technical limitations regarding atoms names in Jana2020.

After the chemistry of these intergrown crystals was solved, the way the crystals were intergrown was investigated. Back-scatter electron (BSE) images did not reveal any pattern of intergrowth (see Figure 20 as an example). Since the chemical differences between the phases are small, this was not expected anyway. Instead, selected area electron diffraction (SAED) was employed. By orientating a crystal in a way that approximately shows a pattern as seen in Figure 15, but with only one kind of satellites present, dark-field images could have been produced by scanning over the crystal and looking for this satellite. While no useful dark-field images could be obtained yet, the diffraction patterns were obtained separately (see Figure 21) which shows that the two superstructures are at least separate on a µm-level.

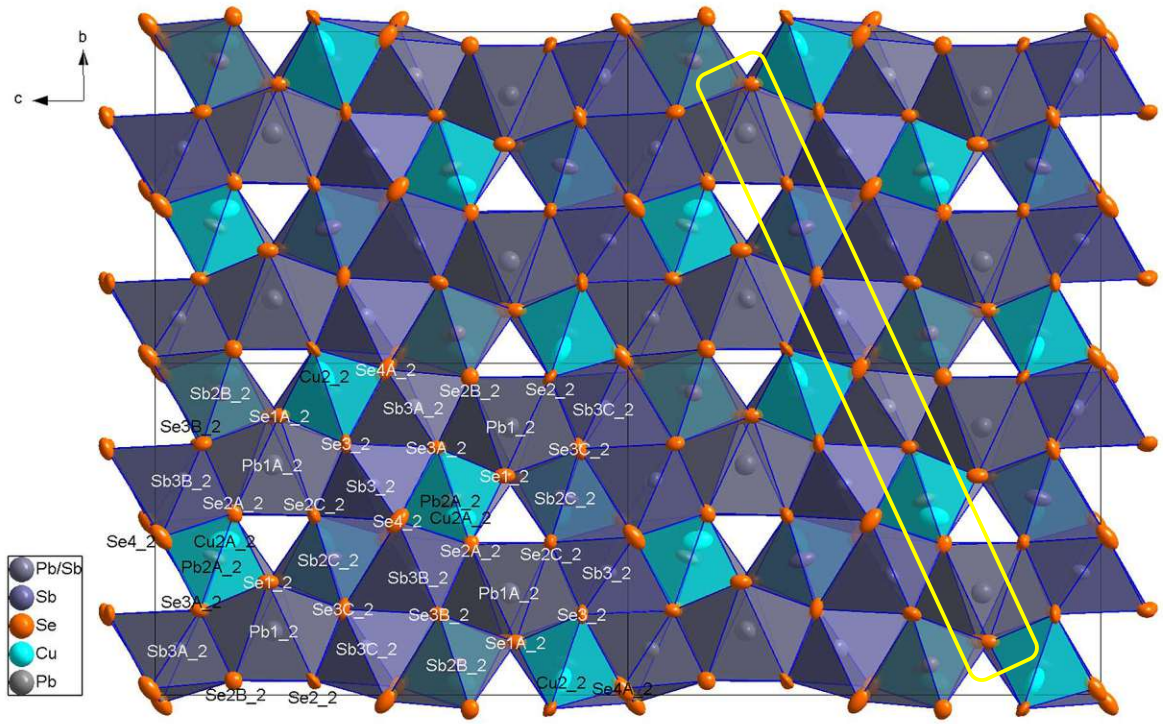

Figure 18: (001)-projection of the orthorhombic part of a 2x/3x intergrown phase, the structure along [001] is shown with the marked atoms in Figure 19

Figure 19: Atoms and labels of the orthorhombic part of a 2x/3x intergrown phase between two Pb1/Sb1-positions located as shown with a yellow rectangle in Figure 18

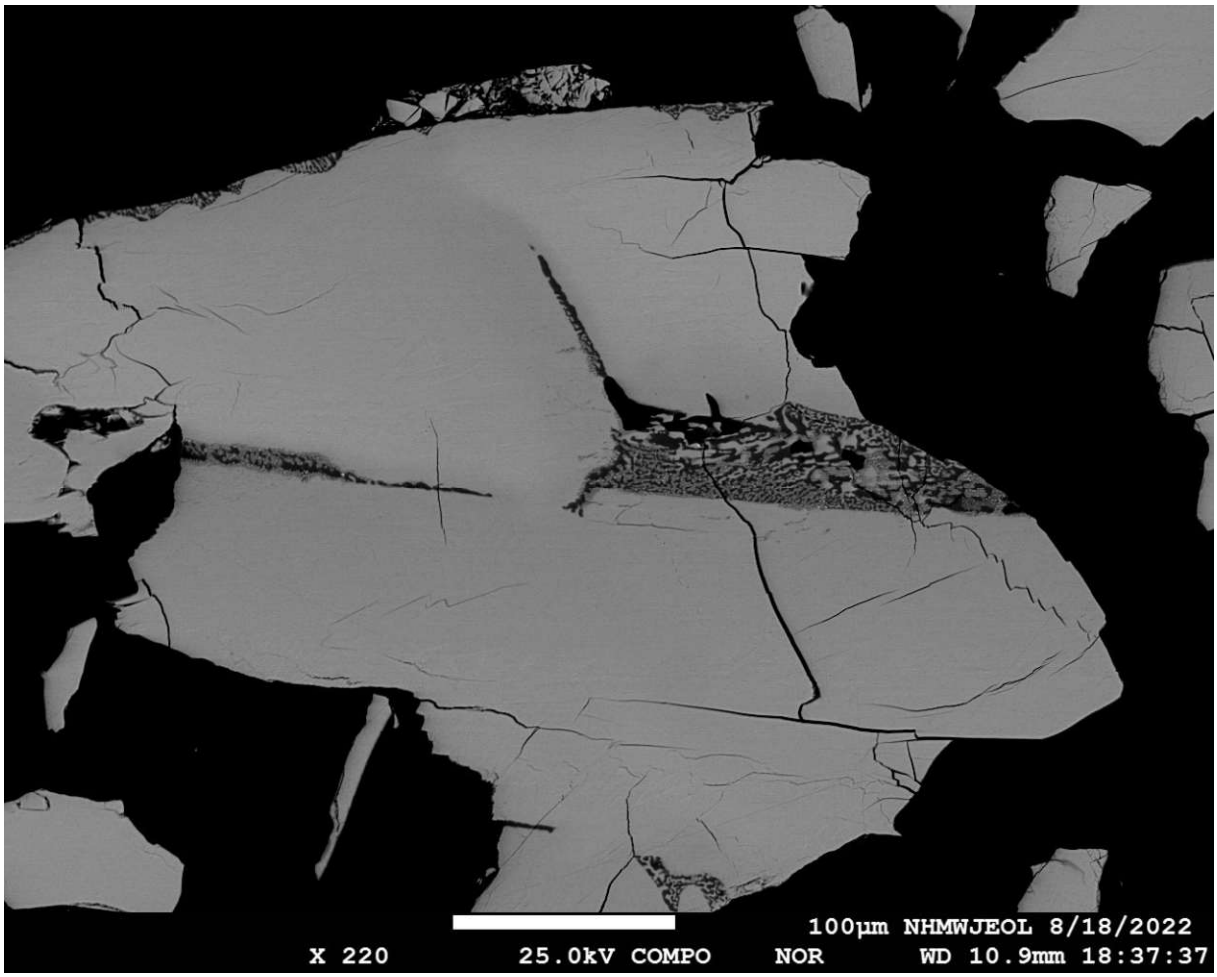

Figure 20: EPMA BSE-image of several crystals from sample 4

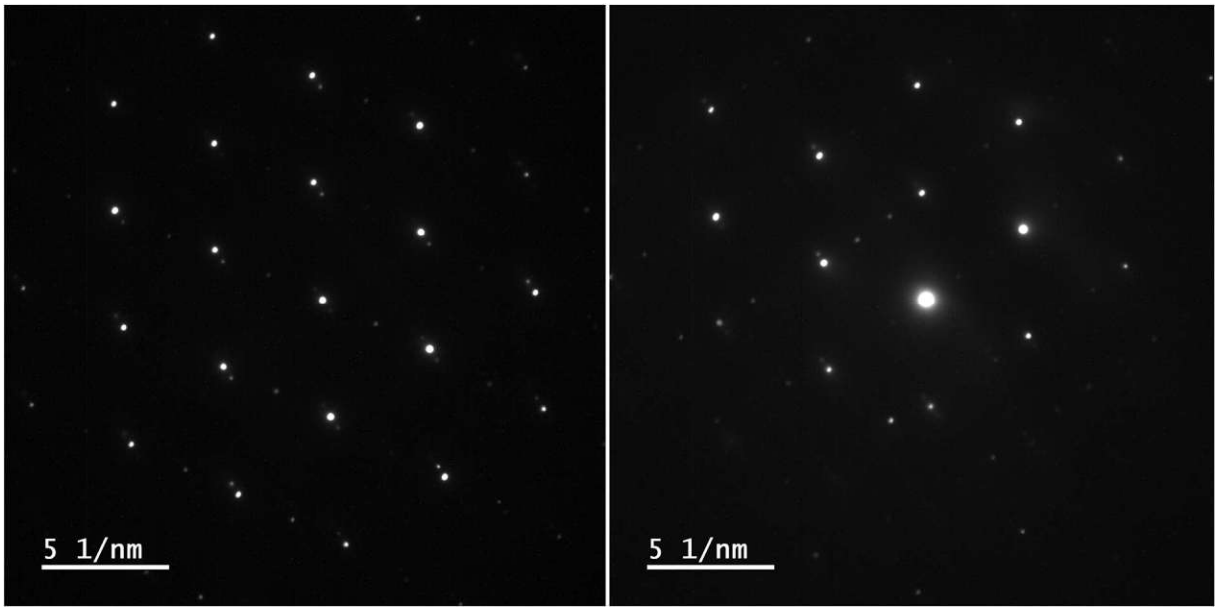

Figure 21: Diffraction patterns from SAED of the same crystal face showing that the different superstructures are separate enough for an electron beam to only detect one

Table 6: Crystal data for the twofold superstructure as part of the combined refinement done with Jana2020

Crystal data	
Chemical formula	$CuPbSb_3Se_6$
M_r	1109.7
Crystal system, space group	Monoclinic, $P2_1/c$
Temperature (K)	300
a, b, c (Å)	7.2635, 19.8883, 8.2975
β (°)	106.414
V (Å^3)	1149.80
Z	4
Radiation type	Mo $K\alpha$
μ (mm^{-1})	42.30
Crystal size (mm)	0.04 × 0.03 × 0.02
Data collection	
Diffractometer	STOE STADIVARI
Absorption correction	Multi-scan, STOE LANA
T_{min}, T_{max}	0.426, 0.561
No. of measured, independent and observed [$I > 3\sigma(I)$] reflections	40275, 22992, 7639
R_{int}	0.415
$(\sin \theta/\lambda)_{max}$ (Å^{-1})	0.837
Refinement	
$R[F^2 > 2\sigma(F^2)]$, $wR(F^2)$, S	0.038, 0.085, 0.98
No. of reflections	22992
No. of parameters	285
$\Delta\rho_{max}$, $\Delta\rho_{min}$ (e Å^{-3})	6.19, −4.31

To conclude the description of the intergrown phases, detailed data is given in Table 6 and Table 7. The R_{int} values of 0.415 are very high because the absorption correction was done in a big sixfold cell encompassing all reflections. A low R_{int} is neither expected nor needed. The results of this combined refinement are plausible and redundant for most atom positions. This is valuable because it confirms the results from pure crystals outlined in previous chapters and shines some light on structural differences between the pure commensurate phases and the oriented intergrowth.

Table 7: Crystal data for the threefold superstructure as part of the combined refinement done with Jana2020

Crystal data	
Chemical formula	$Cu_{0.896}Pb_{1.092}Sb_{3.011}Se_6$
M_r	1123.5
Crystal system, space group	Orthorhombic, $Cmc2_1$
Temperature (K)	300
a, b, c (Å)	12.44, 13.9479, 19.9026
V (Å^3)	3453.34
Z	12
Radiation type	Mo $K\alpha$
μ (mm^{-1})	43.43
Crystal size (mm)	0.04 × 0.03 × 0.02
Data collection	
Diffractometer	STOE STADIVARI
Absorption correction	Multi-scan, STOE LANA
T_{min}, T_{max}	0.669, 0.891
No. of measured, independent and observed [$I > 3\sigma(I)$] reflections	40275, 22992, 7639
R_{int}	0.415
$(\sin \theta/\lambda)_{max}$ (Å^{-1})	0.837
Refinement	
$R[F^2 > 2\sigma(F^2)]$, $wR(F^2)$, S	0.039, 0.086, 0.99
No. of reflections	22992
No. of parameters	282
$\Delta\rho_{max}$, $\Delta\rho_{min}$ (e Å^{-3})	6.19, −4.31
Absolute structure	1686 of Friedel pairs used in the refinement

3.1.5 Heating and Cooling of 2x/3x-Phases

Sample 4 consisted almost entirely of intergrown crystals which is why a crystal from this sample (it will be called 4h12) was used for a temperature dependent SCXRD measurement series. While heating, the satellites of the threefold superstructure disappeared first after 346 °C and the satellites of the twofold superstructure after 357 °C. The sample was cooled, and the satellites reappeared at the same temperature levels of 346 °C and 357 °C. In the case of the twofold superstructure, the previously missing twinning occurred. For pure twinned 2x phases, orthorhombic symmetry is retained with the twin operation. Furthermore, the intensities of the satellites relative to the main reflections changes after heating. These changes are shown in Figure 22. Instead of only seeing the satellites of the twofold superstructure according to the modulation wave vector $\mathbf{q}_{2x}$ like it was the case before heating (see Figure 15), a second group of satellites appears according to the vector $\mathbf{q}'_{2x}$. Satellites of the threefold superstructure remain unchanged in their position.

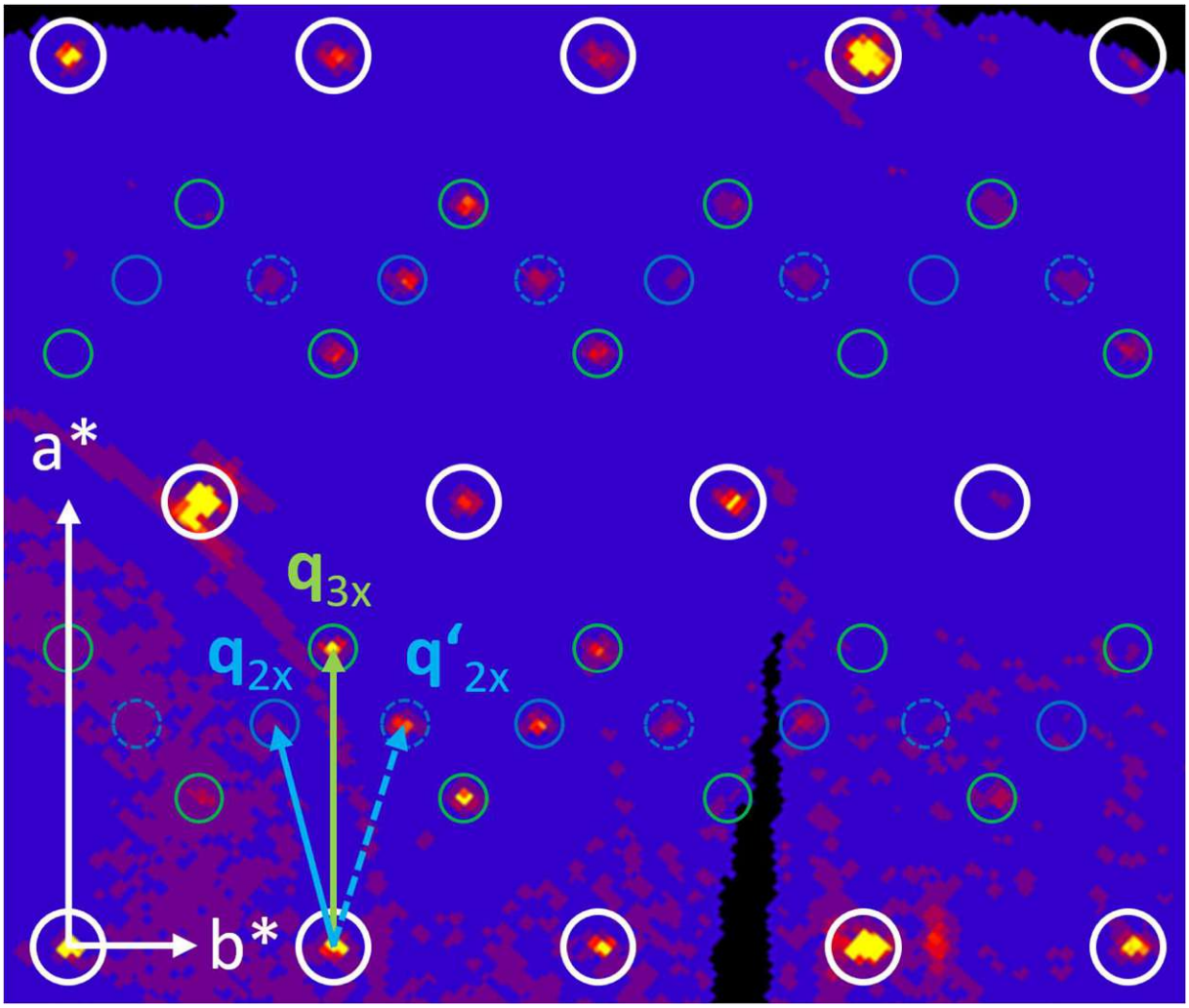

Figure 22: Section of a precession image recorded from crystal 4h12 at 303 °C. Present and absent reflections are marked with circles.

High-temperature structures were recorded; however, they are equal to the basic structure already shown in chapter 3.1.1 but with larger ADP tensors. The high-temperature structure of 4h12 at 357 °C has the cell parameters *a* = 4.1657(3) Å, *b* = 13.9127(8) Å, *c* = 20.2952(11) Å

and a sum formula of $Cu_{0.77}Pb_{0.87}Sb_{3.37}Se_6$ (4.3% excess charge). The structure was refined to an R_{obs} of 4.73%

To quantify these changes, the ten most intensive satellites and, respectively, main reflections were averaged for each measurement. To compare the results for different temperatures, only the ratios were used. As the graph in Figure 23 shows, before heating the crystal to the point where satellites disappeared, the satellites from the twofold superstructure had an intensity equivalent to 40‰ of the main reflections at 303 °C while the satellites from the threefold superstructure only had an intensity of 5.4‰. Conversely, after heating the crystal over the point where all satellites disappeared and cooling it back down to 303 °C, the intensity of the satellites of the twofold superstructure was 11.8‰ (5.7‰ for one domain, 6.1‰ for the other) at while threefold superstructure was at 13.5‰.

This is remarkable as it shows a change in the ratio of the superstructures in the intergrown crystal and means that elemental composition is either no factor or only a minor factor in determining what superstructure the crystal will exhibit. In other examinations, pure twofold superstructures sported satellites of a threefold superstructure after heating which further proves a certain ambiguity during the formation of such crystals. No twinning as seen in Figure 22 was observed in crystals after the formation at 600 °C which makes this result even more interesting. The reason for this difference is either the condition of the syntheses (long tempering, slow cooling) or phase transitions between 400 °C and 600 °C that result in intermediate phases from which 2x crystals grow directly in only one orientation. From our experiments, neither explanation can be confirmed nor ruled out.

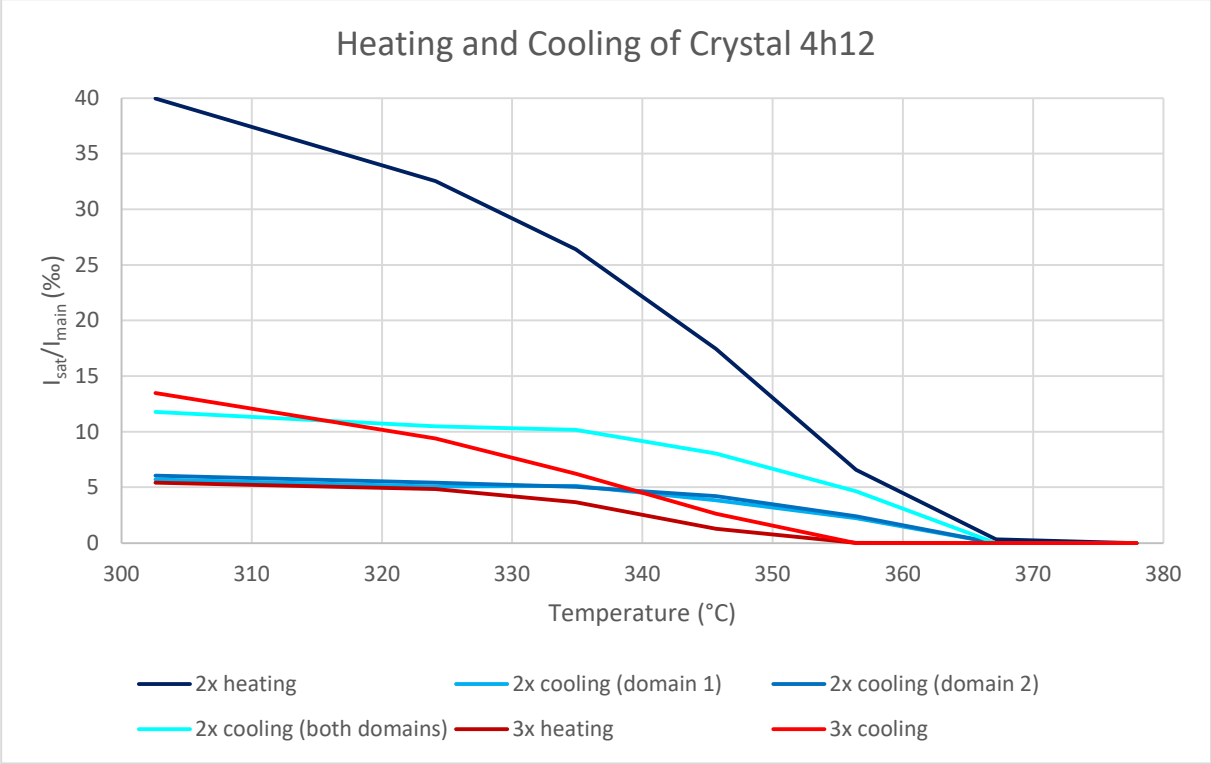

Figure 23: Temperature dependent SCXRD measurements of crystal 4h12 show that the relative intensities of satellites changes from before the disappearance of the satellites

3.1.6 Incommensurate Structure (ic)

In addition to the commensurate phases 2x and 3x, an incommensurate phase was also observed. Because of the comparatively small number of different atomic positions and the additional information provided by modelling the (3+1)-dimensional internal space, the disordering is much less ambiguous than in the previously discussed phases. It also belongs to the family of andorite-like structures with equivalent four octahedra thick slabs, the symbol ^{4}L applies.

The structure crystallises in the superspace group type *Cmcm*(*α*00)00*s* and the cell parameters are *a* = 4.1648(6) Å, *b* = 14.0608(10) Å and *c* = 19.9793 Å with the modulation vector being **q** = (0.683936, 0, 0), which is very close to $\mathbf{q}_{3x}$ = (2/3, 0, 0). The refined sum formula is $Cu_{1.03}Pb_{1.45}Sb_{2.70}Se_6$ which means that the incommensurate phase is much richer in Pb than its commensurate counterparts. This is confirmed by the EPMA results of sample 12 from which the crystal used for data collection was taken. While the compositions of the five analysed phases varied, a phase with the resulting sum formula would not be an outlier (see Table 8). The sum formula derived from the structure is closer to being neutral than most of the grain compositions as measured with EPMA, too. These somewhat divergent EPMA results also show that some variation of the elemental composition still results in ic phases.

Table 8: Elemental composition of grains from sample 12, denoted in sum formulae along the sum formula from the incommensurate structure. Charge balances are given, only one is more than a standard deviation removed from zero.

Grain-Phase	Cu	Pb	Sb	Se	Charge Balance
1-1	0.936(16)	1.637(16)	2.592(13)	6	-0.11(43)%
1-2	1.177(24)	1.304(24)	2.747(15)	6	0.21(48)%
2-1	1.077(28)	1.547(31)	2.630(21)	6	0.50(46)%
3-1	1.101(23)	1.477(54)	2.639(17)	6	-0.25(36)%
4-1	1.076(13)	1.604(41)	2.560(29)	6	-0.31(36)%
Structure	1.030	1.447	2.698	6	0.15%

The atom positions in the structure correspond to those in the basic structure, however, the positions Se4' and Pb2' are added to describe disordering and the interstitial Cu-position Cui is added because of additional electron density being detected. In Figure 24, the average structure is projected onto (100) with every position being labelled. Figure 25 shows a section of the structure along [100] to illustrate the way the Sb2/Cu2/Pb2-position from the basic structure is ordered by the incommensurate modulation. This figure illustrates the similarities to the threefold superstructure. In that structure, the Sb2/Cu2/Pb2-position is ordered in a way where two different kinds of positions repeat themselves in an ABB-pattern. If a small enough section is considered, the same happens in the incommensurate structure. However, a bigger section shows that the ABB-pattern is in fact exchanged with an AAB-pattern along [100]. The

reason for longer stretches of the structure being similar to the threefold superstructure lies in the similarities of the respective modulation vectors $\mathbf{q}_{3x}$ and $\mathbf{q}_{ic}$. The components for the first coordinate are 2/3 for $\mathbf{q}_{3x}$ and 0.683936 for $\mathbf{q}_{ic}$ which, numerically, are similar but the small difference leads to one structure having a commensurate modulation and the other an incommensurate one.

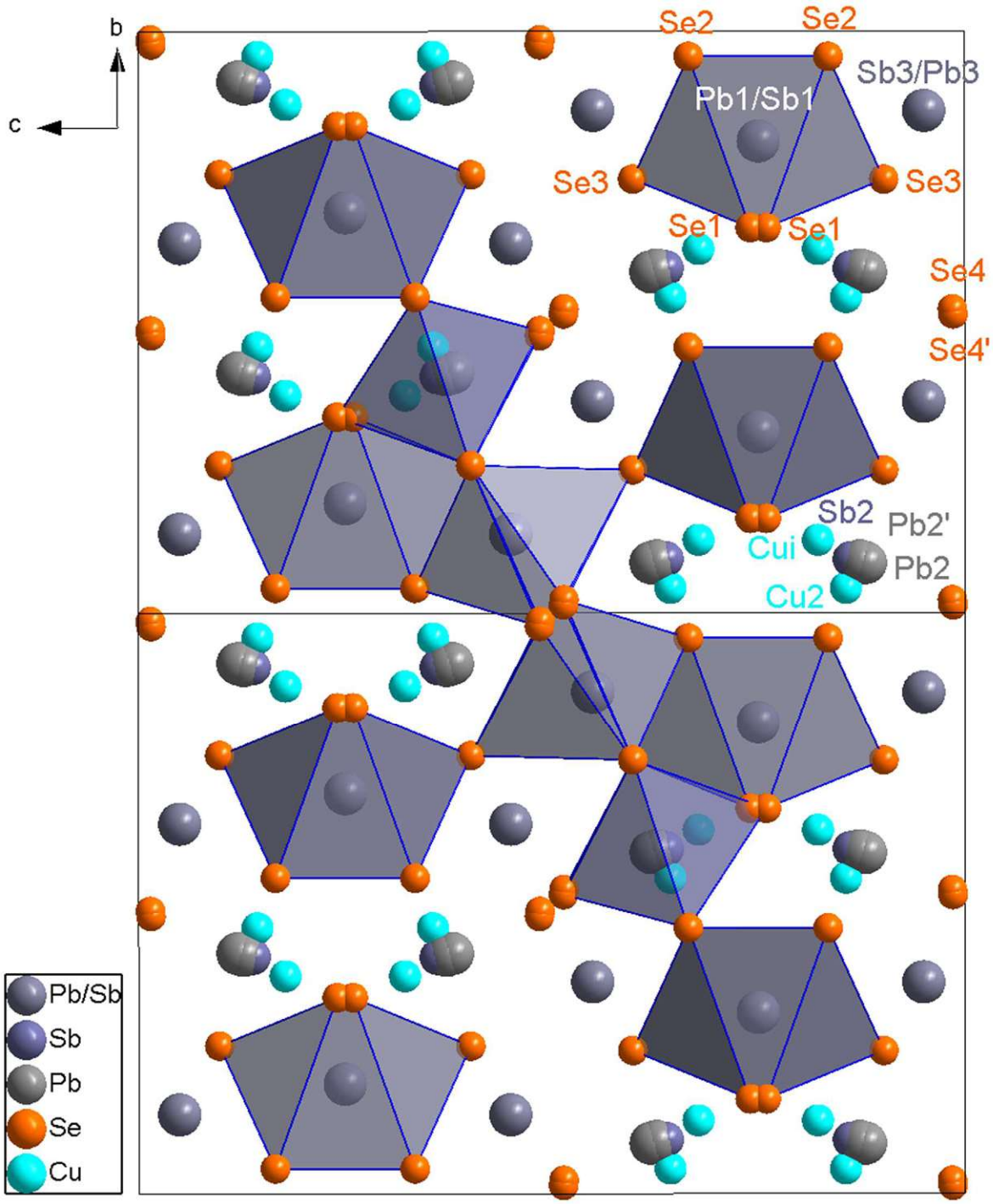

Figure 24: Average structure of the incommensurately modulated andorite phase

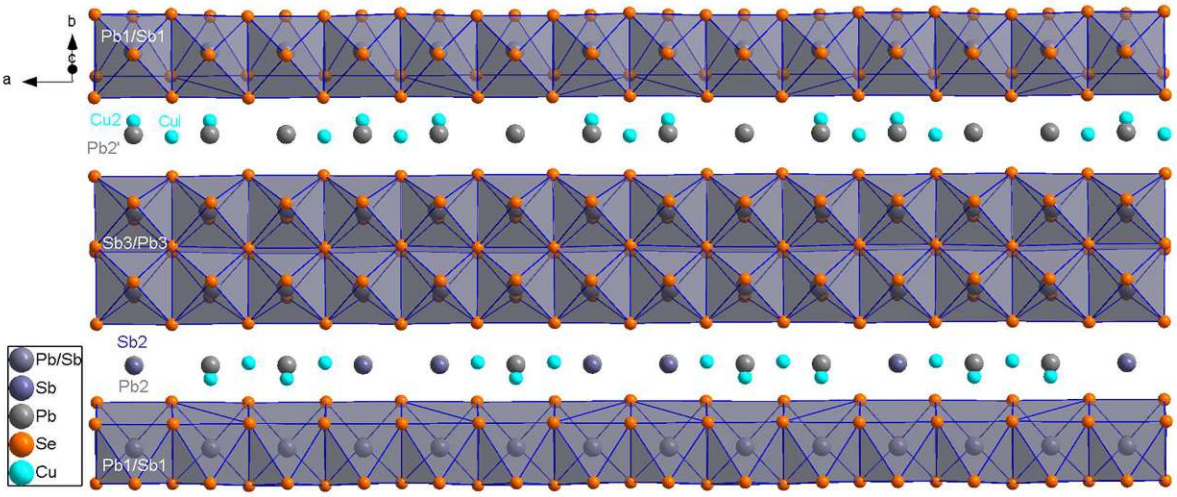

Figure 25: A section of the structure of the incommensurately modulated andorite phase showing the way the Sb2/Cu2/Pb2-position from the basic structure is ordered to Sb2/Pb2, Cu2/Pb2' and Cui

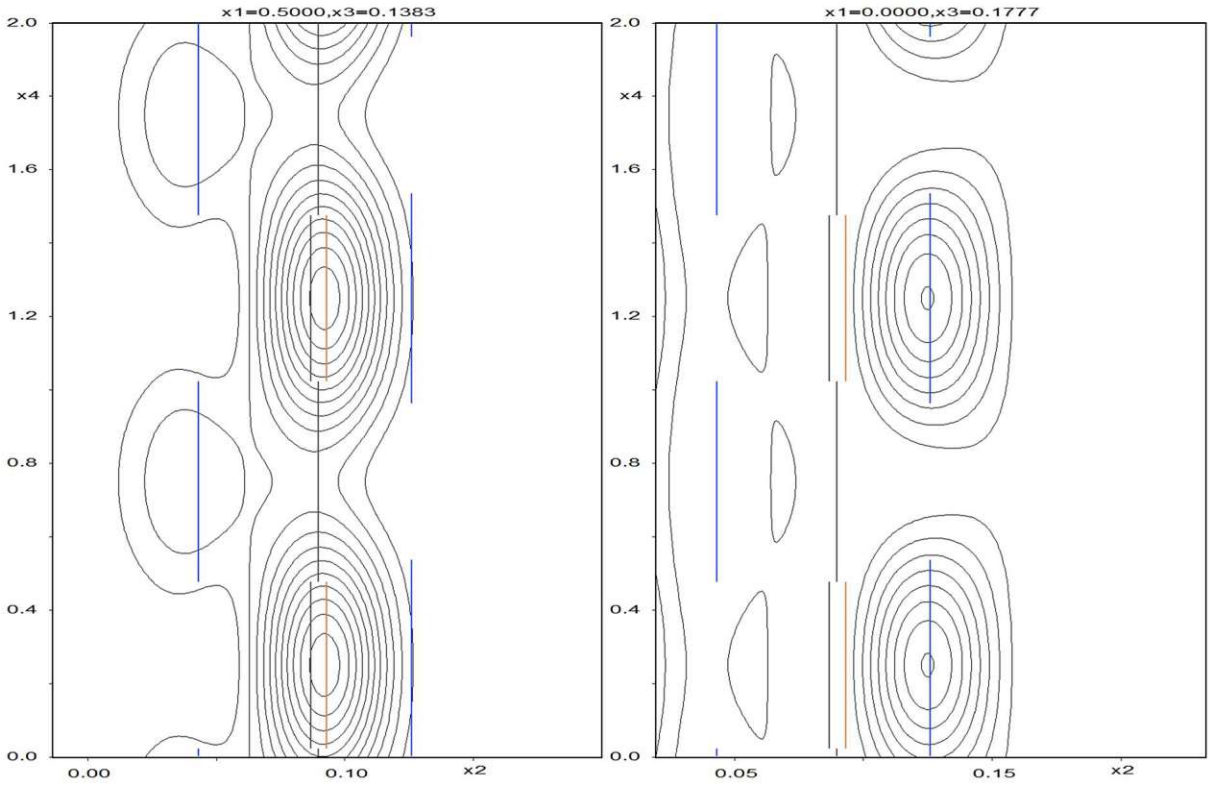

Figure 26: Cu2, Cui, Sb2, Pb2 and Pb2' in internal space, left at x_1 = 0.5 and right at x_1 = 0 where Cui lies

In internal space, most positions had to be modelled with discontinuous positional modulation functions because other variants were unstable in the refinement. For every crenel function, a x_{40} of either 0.25 or 0.75 was fixed because the electron densities were symmetric around these coordinates in x_4. The refinement of the crenels started with them having a delta of 0.5 in x_4, the crenels of Cu2 and Pb2' ended with about 0.55 and Sb2 and Pb2 correspondingly with about 0.45 (see Figure 26). The crenel of Cui has a delta of about 0.57 which does not fit with the positions of Sb2 and Pb2 although they have the same x_{40}. Consequently, Cui is not only realised between Cu2/Pb2'-atoms but between Cu2/Pb2' and Sb2/Pb2 as well. Differing

from the approach used during refinement of the threefold superstructure, a realisation of Cui does not replace the neighbouring atoms. Therefore, a distinction to CuI from the threefold superstructure is established by changing the symbol to Cui.

It is assumed that Cui is generally realised between two Cu2-atoms and in some cases with Pb2 when being realised between an Sb2/Pb2-position and a Cu2/Pb2'-position as Pb2 is further away than Sb2. In the case of a Cu2-Cui-Cu2 realisation (see Figure 27), the Cu-Cu distances are 2.4803 Å which is realistic when compared to the structure of Cu_2Se where Cu-Cu distances range from 2.325 Å to 2.847 Å. [31] In the case of Pb2-Cui-Cu2, the distance between Pb2 and Cui would be 2.4412 Å which seems too small. Cu-Pb distances in sulfosalts normally are around 3.4 Å with seligmannite being on the lower end with 3.269 Å. [32] It is thus deemed unlikely that a Pb2-Cui-Cu2 realisation exists, although it cannot be ruled out entirely. An Sb2-Cui-Cu2 realisation is even less likely as Sb-Cu distances are usually not shorter than Pb-Cu distances and Sb2 would be closer to Cui with a distance of only 2.274 Å.

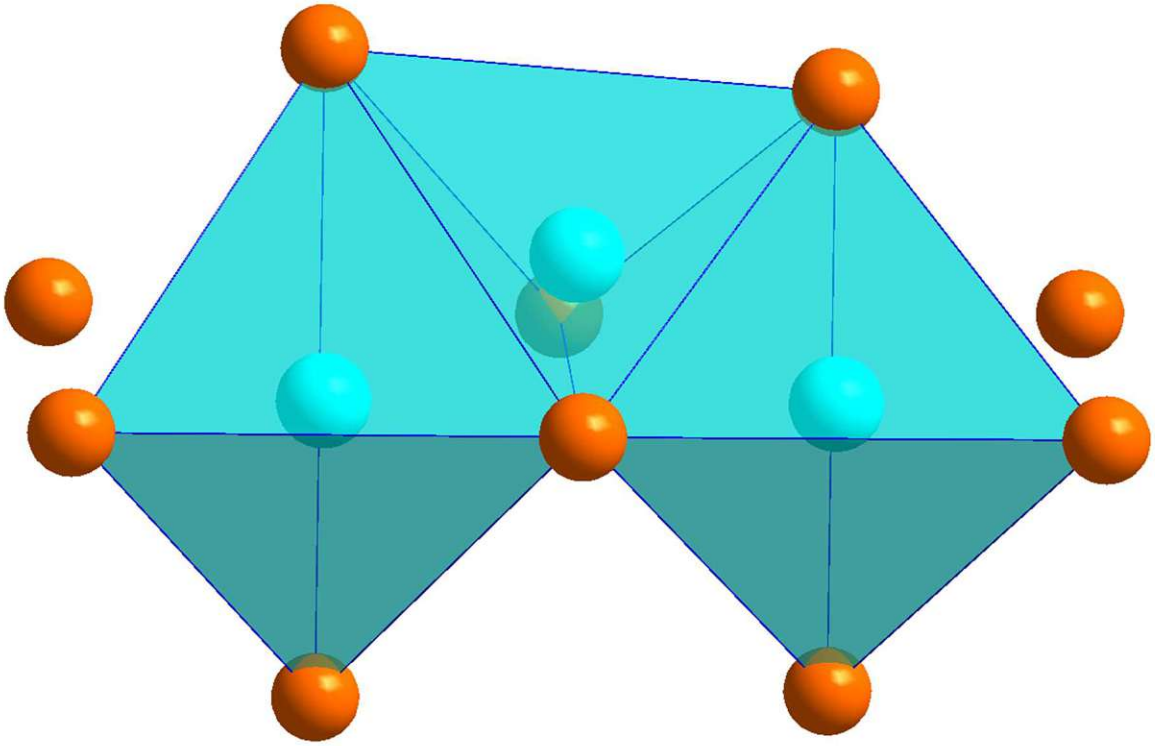

Figure 27: Justification for the interstitial position modelled as not replacing any atoms: the Cu2-Cui-Cu2 tetrahedral chain

The other modulations modelled with crenel functions are those of Se1, Se4 and Se4'. Their deltas were fixed at 0.5 with an x_{40} of 0.25 because the electron density is symmetric around this x_4. Se4 and Se4' are disordered around (2_{100}, *s*). The need for Se4' arises from the displacement in both x_2 and x_3 while Se1 is only displaced along x_3 (see Figure 28 and Figure 29). Additional positional modulation functions led to unstable refinements although Se1 should probably be modelled as such. They were successfully used to model Se2, Se3, Pb1/Sb1 and Sb3/Pb3 although these atoms only experience minor displacement.

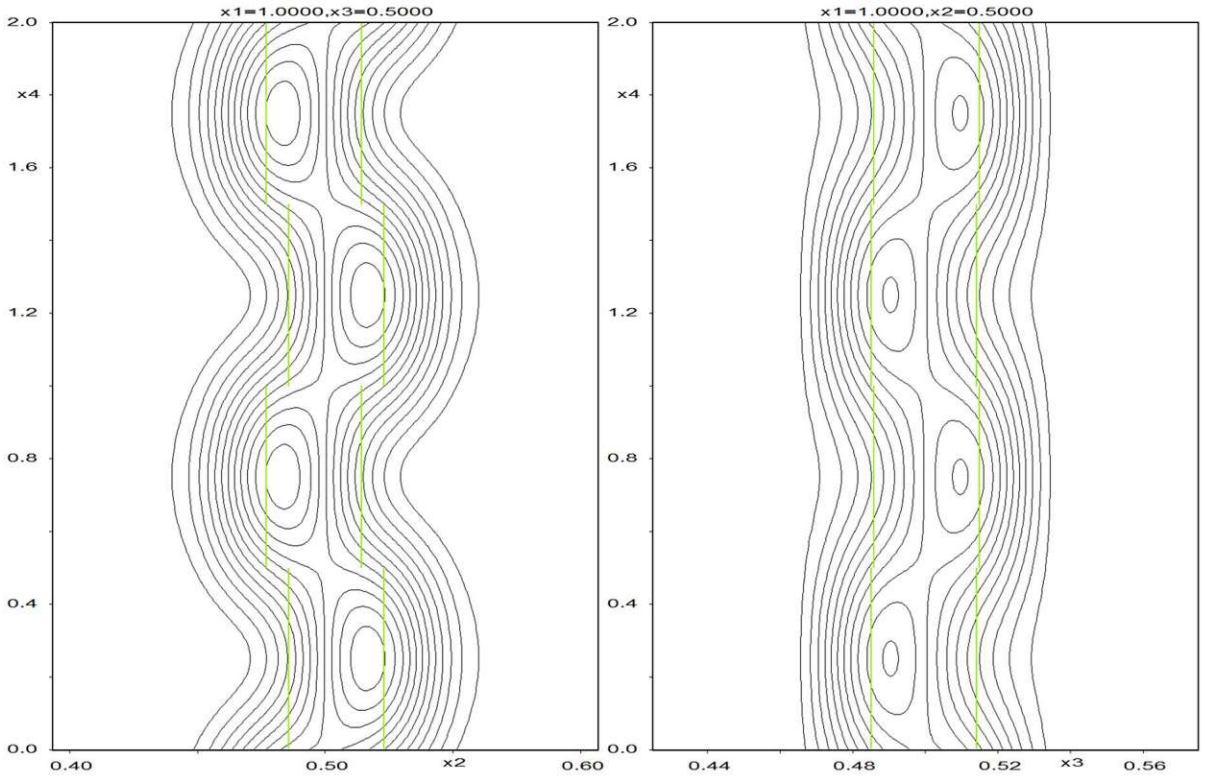

Figure 28: Modulations of Se4 and Se4' in x_2 and x_3, Se4 is the atom with higher occupancy

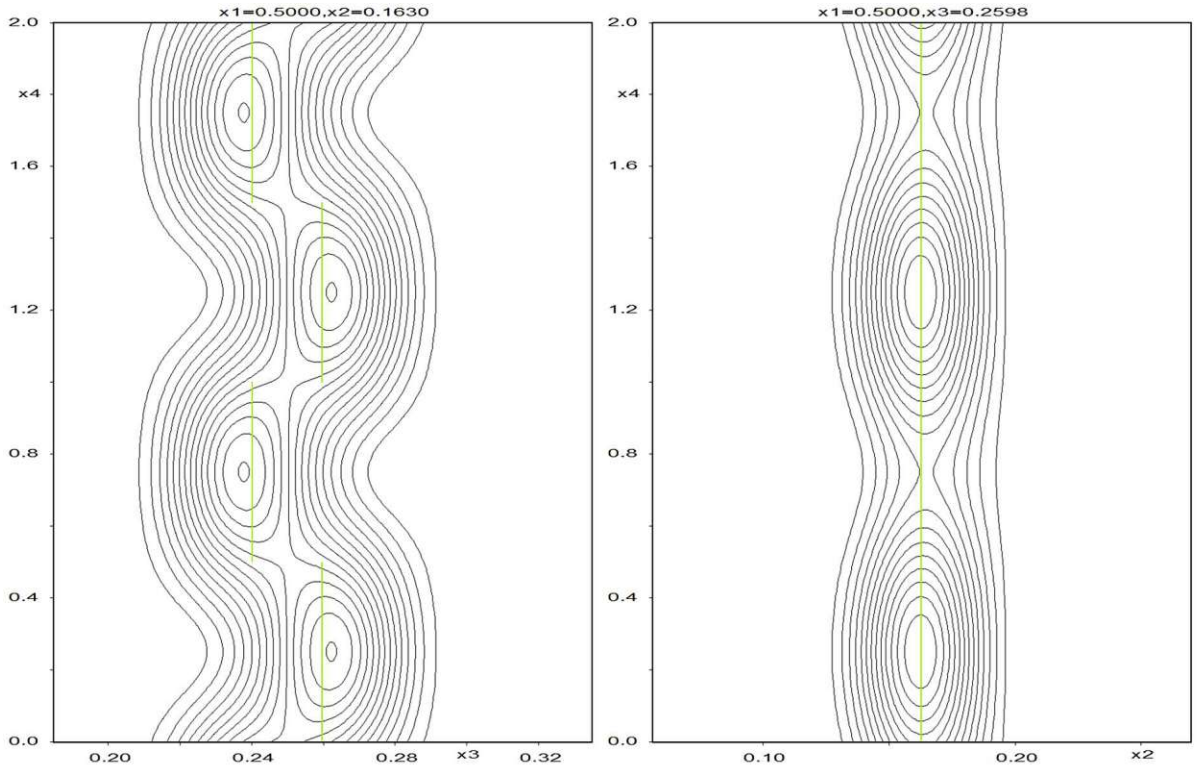

Figure 29: Modulation of Se1 along x_2 and x_3, Se1 is not displaced along x_3 and therefore appears as a line

3.1.7 Heating and Cooling of ic-Phases

Similar to the 2x/3x-phase, when heating crystals with an incommensurate superstructure, the satellites disappear after 335 °C and reappear before 324 °C. A good example for this simple disappearance is shown in Figure 30 where crystal 13h5 was used. A lowering of the intensities of satellites relative to the intensities of the main reflections could be attributed to degradation of the crystal or to structural effects. From the collected data, it is not possible to definitively determine whether only one or both given reasons apply. Looking at the cell parameters, *a* and *c* increase with temperature while the *b* direction shows a negative thermal expansion. In terms of the [(Pb,Sb)Se_8] polyhedra, this means that the uncapped side moves closer to the centre while the capped sides move further away as is expected during thermal expansion. The $\mathbf{q}_x$ component changed from 0.679 during heating to 0.676 during cooling with no temperature dependence observed. This signifies changes in the structure after the order-disorder phase transitions. These changes could however be induced by decomposition of parts of the crystal as well.

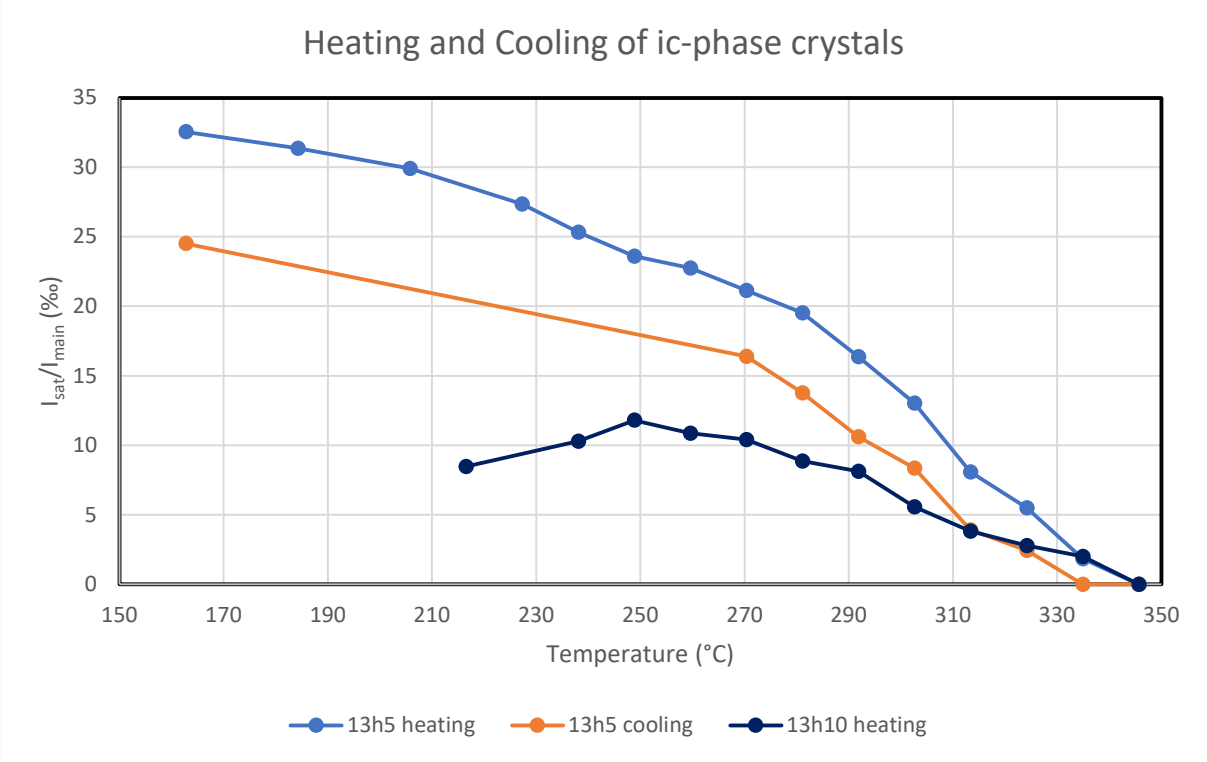

Figure 30: Changes to the intensities of the satellites relative to the main reflections during heating and cooling of a crystal with incommensurate superstructure (13h5)

A peculiar phenomenon was the crystal 13h10 with diffuse satellites whose room temperature structure was used to describe the basic structure in chapter 3.1.1. A reciprocal space reconstruction can be seen in Figure 31. When heating, the satellites became less diffuse and reached their peak ratio of 11.8‰ at 249 °C (see Figure 32). The satellites remained sharp after cooling and could be measured at room temperature. Compared to the satellite intensities of 13h5, 11.8‰ is very low since 13h5 sported a ratio of 23.6‰ at 249 °C.

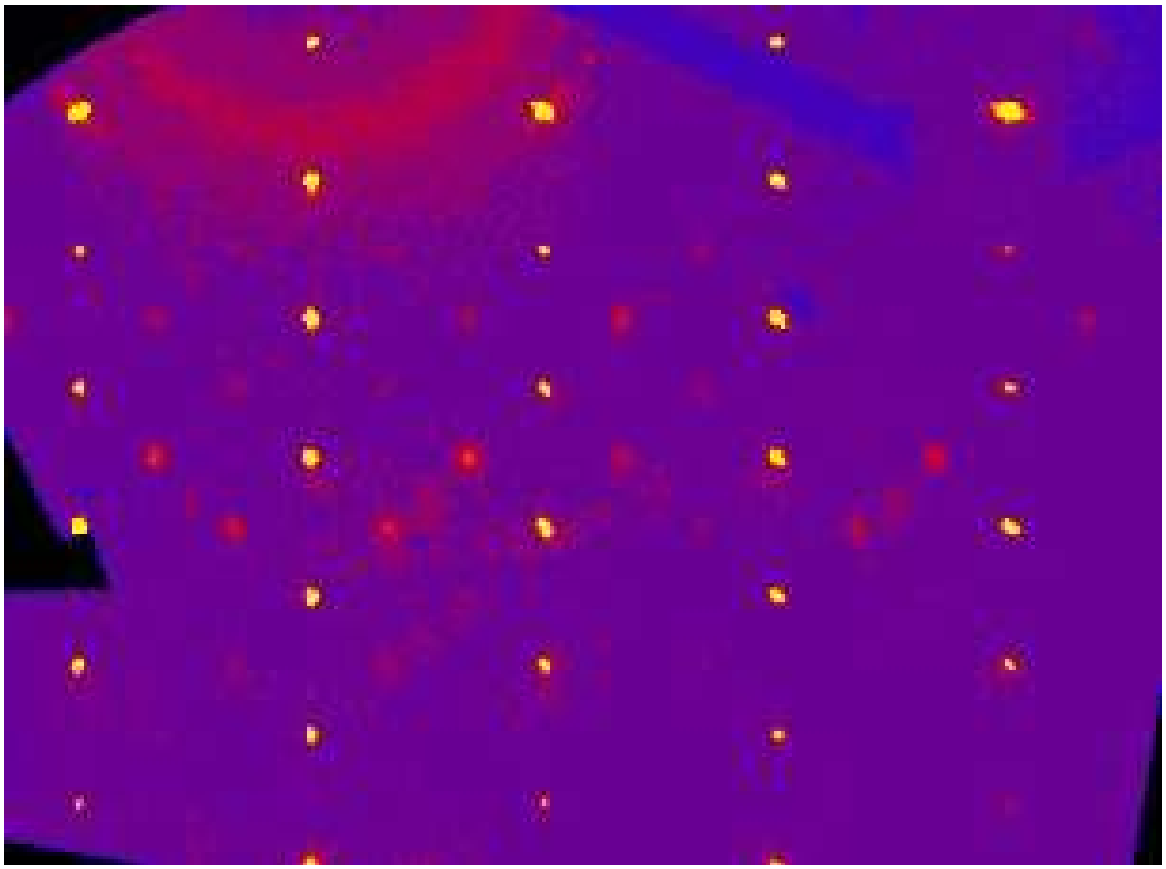

Figure 31: Diffuse satellites of 13h10 at room temperature

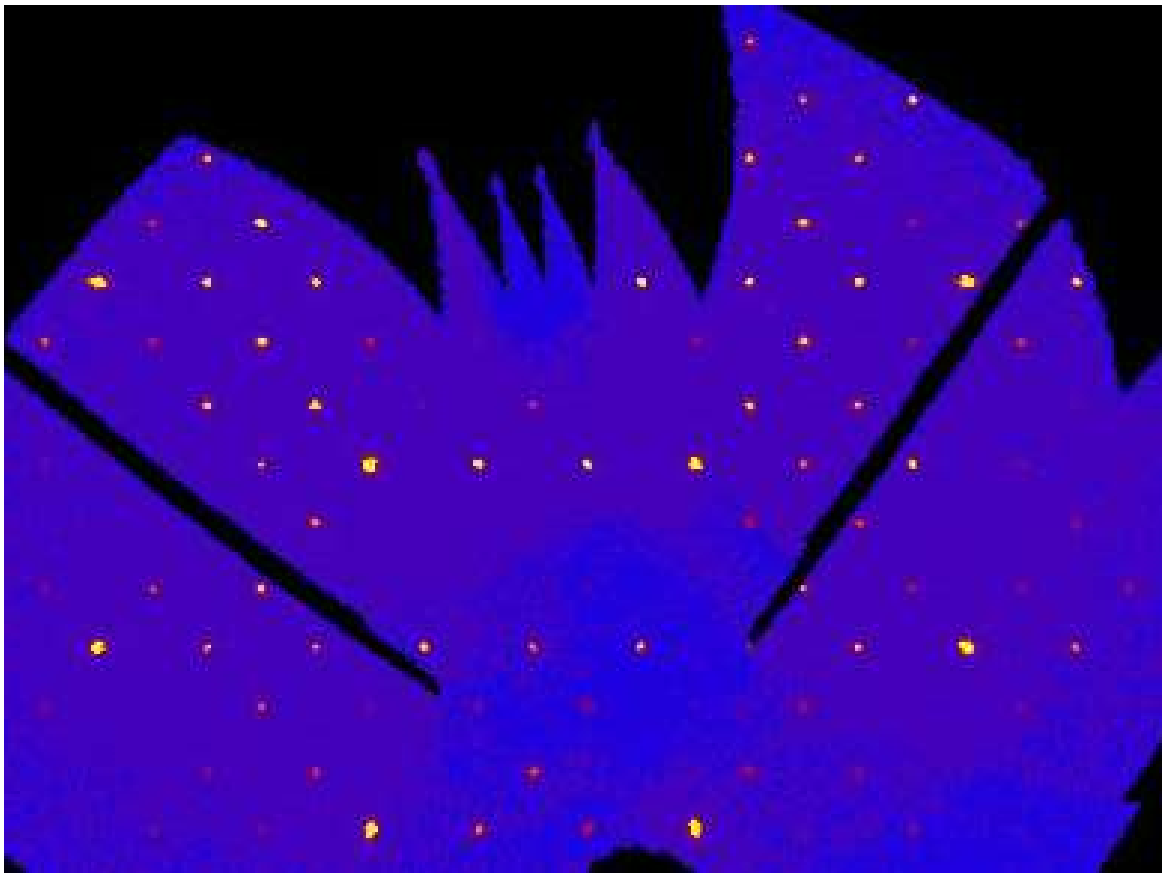

Figure 32: Sharp satellites of 13h10 at 237 °C

3.2 Orthorhombic-primitive $CuPbSb_3Se_6$ (oP)

The contents of this chapter will have already been published in Acta Crystallografica Section E. Minor changes have been made to make that article fit the style of this thesis.

Single crystals of $CuPbSb_3Se_6$ were obtained as minor phase during systematic studies of the building conditions of selenide-based sulfosalts. The crystal structure is an unusual representative of the family of sulfosalts. Instead of the expected galena-like slabs with octahedral coordination, it features mono and double-capped trigonal prismatic (Pb), quadratic pyramidal (Sb) and trigonal bipyramidal (Cu) coordination. All metal positions are occupationally and/or positionally disordered.

3.2.1 Chemical Context

Sulfosalts [4] are promising candidates as thermoelectric materials owing to their high electrical paired with a low thermal conductivity. Inspired by natural sulphur-based sulfosalts, we attempted to further increase the electrical conductivity by substituting Se for S. During systematic studies of the formation condition of sulfosalts of the andorite structure type [4] we obtained crystals of the title compound $CuPbSb_3Se_6$ as minor phase, by heating the precursor selenides Cu_2Se, PbSe and Sb_2Se_3 in evacuated fused silica ampules. Surprisingly, the title compound does not follow the expected crystal-chemistry of the structural family. In fact, crystals of the andorite family are modular structures, which are composed of galena-like slabs, with octahedral coordination of the metal atoms. This coordination is not observed for $CuPbSb_3Se_6$. Nevertheless, certain structural relationships can be established, as will be shown below. These structural relationships are reflected by andorite-like compounds of the $Sn_3Bi_2Se_6$ structure type [33] with very similar cell parameters yet a different spacegroup symmetry. The structure with the closest matching cell parameters is $SnPb_2Bi_2S_6$ [34] with a = 20.5458(12) Å, b = 4.0925(4) Å and c = 13.3219(10) Å, whereby the axes have been cyclically permuted with respect to the cell of $CuPbSb_3Se_6$ presented here. $SnPb_2Bi_2S_6$ crystallizes in a lillianite-type ^{4}L [4] structure and was investigated by the authors for its thermoelectric performance and sported a figure of merit ZT of 0.3. Since $CuPbSb_3Se_6$ shows strongly disordered positions, it is possible that it exhibits similar thermoelectric properties.

It should be noted that from a structural point of view, lillianites and andorites are interchangeable terms. However, in a mineralogical context, they define distinct sulfosalt mineral groups because the Sb that replaces Bi from the lillianite structure in andorite forms electron pair micelles that distort the structure. [9]

3.2.2 Structural Commentary

Crystals of the title compound crystallize in the *Pnnm* space group. All atoms are located on or disordered about (in the case of Sb4A) the reflection plane parallel to (001), which corresponds to the Wyckoff position 4*g*. The crystal structure comprises of three mixed Pb/Sb positions, one Sb and one Cu position (see Figure 33).

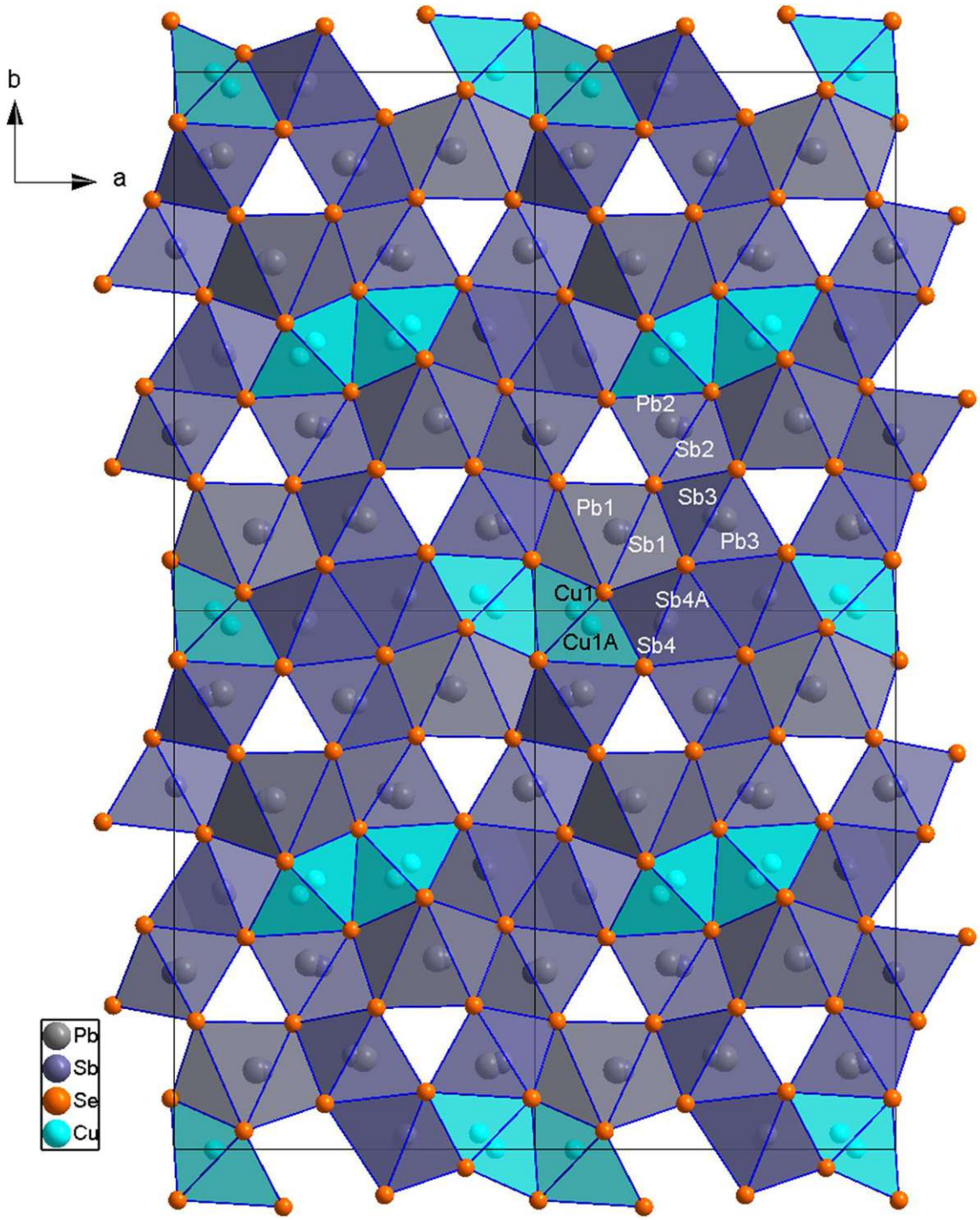

Figure 33: Crystal structure of $CuPbSb_3Se_6$ projected on (001) with every atom position labelled once

There are three different kinds of coordination polyhedra. The predominantly Pb Pb1/Sb1 position is coordinated by Se atoms forming a double-capped trigonal prism. The predominantly Sb Sb2/Pb2 and Sb3/Pb3 positions and the disordered Sb4/Sb4A are quadratic pyramids in case of Sb and mono-capped trigonal prisms in the case of Pb. Finally, the disordered Cu1/Cu1A position features trigonal bipyramidal coordination. Whereas the [PbSe8] double-capped trigonal prisms of the Pb1/Sb1 position are a defining feature of lillianite-type structures and form where the galena-like slabs meet, the remaining two coordinations are unexpected in this structural family.

It has to be noted that the description of the coordination polyhedra of the Sb2/Pb2, Sb3/Pb3 and Sb4/Sb4A positions as quadratic pyramids and capped trigonal prisms is not completely unambiguous. Both variants based on the central atom are shown in Figure 34 for Sb3 and Pb3. Since the distance from Sb3 to the two farther Se6 atoms is 3.7015(19) Å and the corresponding calculated bond valence, using the parameters R_0 = 2.60 Å and b = 0.37, is only 0.05, they are considered not to coordinate with Sb3. In contrast, the Se2 and Se3 atoms at the base of the pyramid are located at 2.9293(15) Å and 2.8835(14) Å, respectively. The Se1 atom at the apex of the pyramid is located at 2.587(2) Å from the Sb3 atom. This is different for Pb3, where the two distant Se6 atoms are much closer with the atomic distances changed to 3.35(3) Å. The other Se atoms are further away with 3.05(3) Å for Se2, 2.86(2) Å for Se3 and 3.02(4) Å for Se1. Note that the large estimated standard uncertainties (ESUs) of the Pb—Se distances here are due to Pb3 being a minor position next to Se3. Thus, in the case of Pb3 atoms, the coordination is clearly a capped trigonal prism, whereas for Sb3 it is better described as quadratic pyramidal. When considering the electron lone-pair of the Sb(III) atoms, the coordination might also be seen as ψ^1-octahedral.

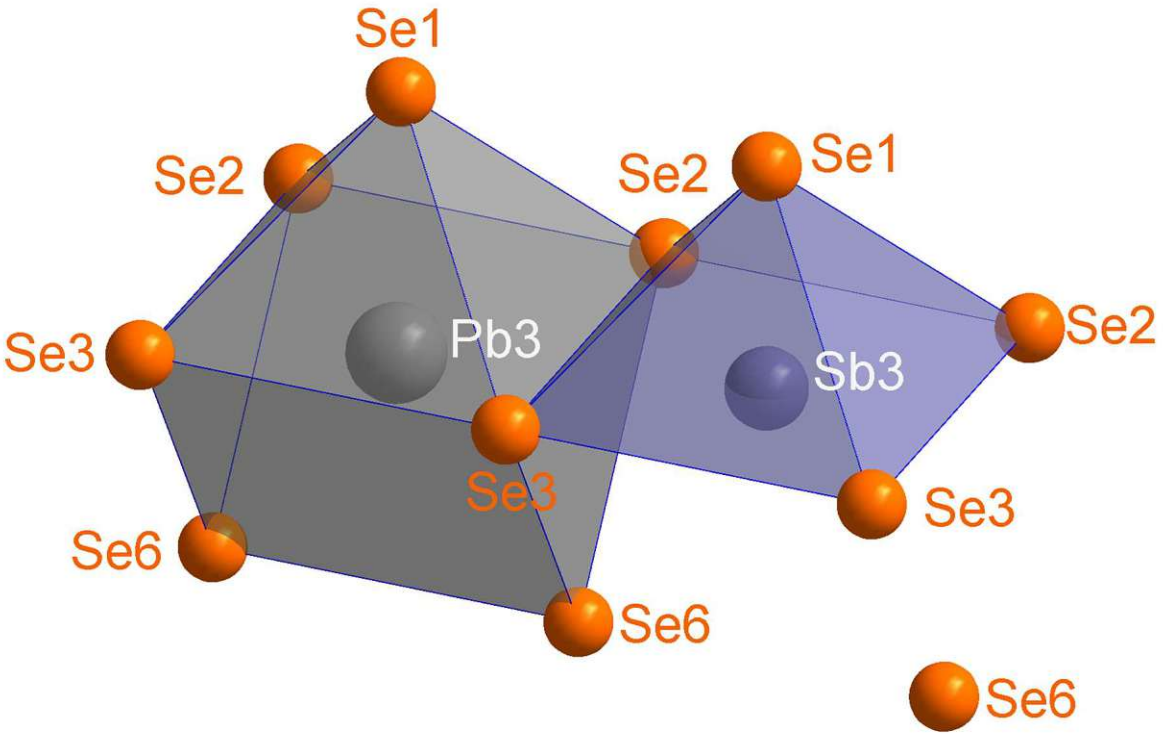

Figure 34: Coordination polyhedra of Pb3 and Sb3

For the Sb2/Pb2 position the same observation is made with slightly changed distances. The extended coordination environment of Sb2 possesses two far Se6 atoms at 3.6962(17) Å, Se1 and Se4 atoms at the square base at 3.1563(14) Å and 2.7090(12) Å and an apex Se3 atom at 2.6135(19) Å. For Pb2 these distances change to 3.283(6) Å, 3.114(7) Å, 2.900(7) Å and 3.094(10) Å, respectively.

On the Sb4/Sb4A position, the Sb atom is sometimes located on the ..*m* position (Sb4, 0.83(3)%) and sometimes to both sides of the reflection plane (Sb4A, 2×0.084(15)%). The coordination of Sb4 is similar to those of Sb2 and Sb3. The coordination polyhedron can be considered as a quadratic pyramid with the bond lengths being 2.723(2) Å (Se6), 3.166(3) Å (Se2) and 2.5945(3) Å (Se5, located at the apex). The next Se atom is Se2 located at 3.875(2) Å from Sb4, which can be considered as non-coordinating. The coordination of Sb4A is very similar, as it is located only 0.44(3) Å from Sb4.

As for the other discussed coordination polyhedra, one might also see the double-capped trigonal prisms that surround the Pb1/Sb1-position Figure 35 as a quadratic pyramid in the case of Sb because the metal atoms do not lie in the centre of the polyhedron. If the Sb1 atom is realized, one might rather think of a fivefold instead of an eightfold coordination, again with the atoms forming a quadratic pyramid. Here, the bond distances involving the Pb1 atom are 3.0553(15) Å and 3.1205(17) Å for the quadratic base (Se1 and Se5) and 2.9124(14) Å to the apex (Se2). The two Se3 atoms are located at 3.5754(15) Å from the Pb1 atom and the last Se4 atom, which forms second cap of the prism is distanced by 3.4061(16) Å. The coordination of Sb1 is very similar (distance to Pb1: 0.26(2) Å), with a slightly more pronounced quadratic pyramidal coordination.

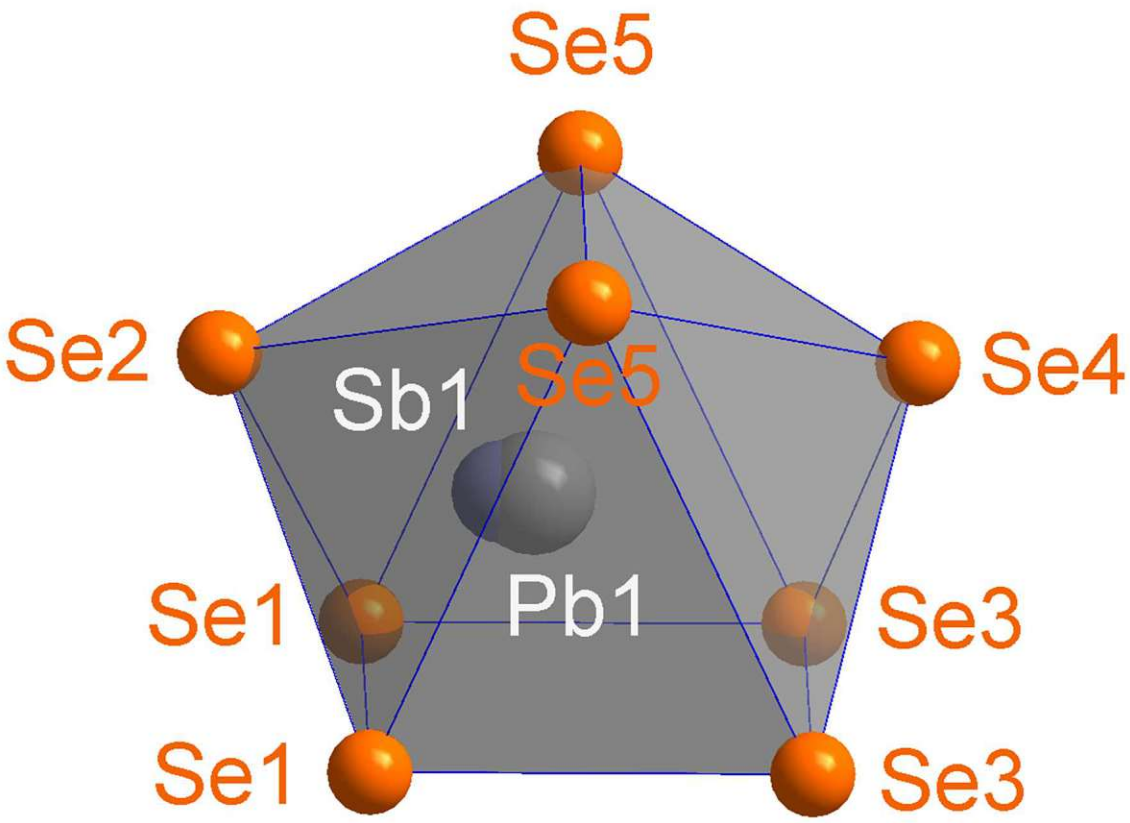

Figure 35: Coordination polyhedron of Pb1 with Sb1 shown as well

The (double-)capped trigonal prism is, as stated above, a defining structural element of the lilianite-family. It is interesting to note that whereas the 90° angles of all the prisms are perfectly

realized owing to the ..*m* reflection plane, the triangular bases deviate significantly from an ideal trigonal symmetry. The prism around Pb1/Sb1 is formed from a triangle with 48.31(2)°, 66.60(3)° and 65.09(3)° angles. The other prisms are closer to regular with the angles most different from 60° being 54.53(3)° for Pb2 and 65.57(3)° for Pb3.

Finally, the trigonal bipyramidal coordination of Cu is unusual as Cu is usually encountered as coordinated tetrahedrally or in a planar square. This is still somewhat true for Cu1/Cu1A, as the disordering takes place over the trigonal base of the pyramids, placing them both in their own tetrahedron. However, the position closer to the base (Cu1), i.e. with the more trigonal bipyramidal-like coordination, has a higher occupancy of 59.5(17)% than the position further removed from the centre of the trigonal bipyramid (Cu1A).

Despite the clearly different coordination polyhedra, CuPbSb3Se6 can nevertheless be described as a distorted ^{4}L andorite-type structure, since there are four polyhedra between two double-capped trigonal prisms as shown in Figure 36. However, the spatial distribution of the Se/S atoms is fundamentally different, leading not only to different coordination polyhedra, as described above, but also an altered connectivity of the polyhedra.

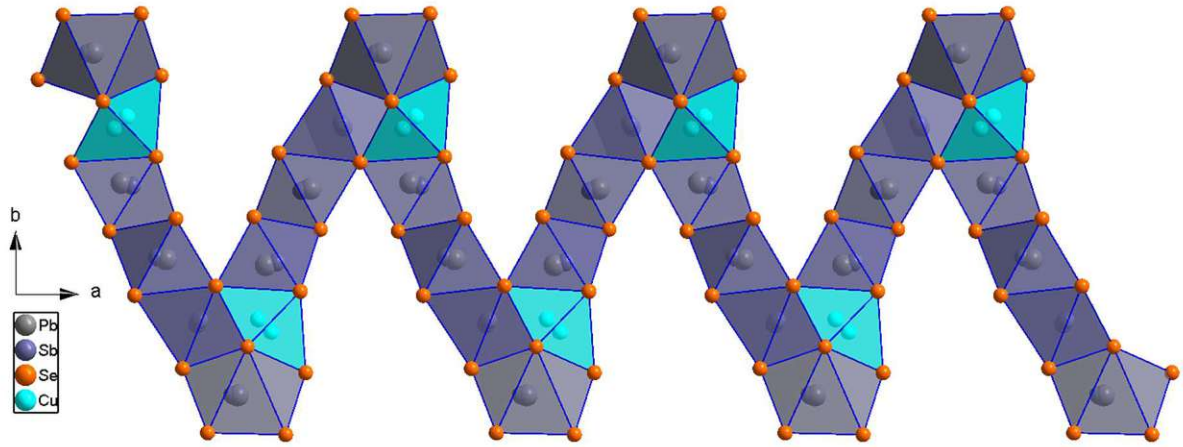

Figure 36: $CuPbSb_3Se_6$ seen as a distorted lillianite-like structure

3.2.3 Database Survey

No compounds containing only copper, lead, antimony and selenium have been deposited in the Inorganic Crystal Structure Database (ICSD) as of December 2022. [24]

3.2.4 Synthesis and Crystallization

40.0 mg Cu_2Se, 47.6 mg PbSe and 125 mg Sb_2Se were intimately mixed and transferred into a fused silica ampoule, which was sealed under vacuum. The ampoule was heated at 1223 K for 2 h, cooled to 873 K over 7 h and held at that temperature for 149 h. After cooling to 473 K over 5 h and quenching in air, the ampoule was opened, and the obtained ingot crushed. Among other phases in the andorite family, single crystals of the title compound $CuPbSb_3Se_6$ were isolated.

3.2.5 Refinement Details

Crystal data, data collection and structure refinement details are summarized in Table 9. All atoms were refined with anisotropic atomic displacement parameters (ADPs). It was necessary to model the Cu-position as positionally disordered to avoid non-positive definite (NPD) ADP tensors. Modelling the positions of Pb1, Sb2 and Sb3 as mixed Pb/Sb-positions as well as the position of Sb4 as positionally disordered improved the residuals significantly. The pairs Pb1/Sb1, Sb2/Pb2, Sb3/Pb3 and Sb4/Sb4A were refined with identical ADP tensor elements, though distinct coordinates. Furthermore, the site occupancies were constrained to full occupancy and the Pb occupancies were restrained to fit the sum formula $CuPbSb_3Se_6$, corresponding to an electroneutral structure.

Table 9: Experimental details for $CuPbSb_3Se_6$

Crystal data	
Chemical formula	$CuPbSb_3Se_6$
M_r	1109.7
Crystal system, space group	Orthorhombic, *Pnnm*
Temperature (K)	300
a, *b*, *c* (Å)	13.7217(5), 20.5149(8), 4.0716(2)
V (Å^3)	1146.15(8)
Z	4
Radiation type	Mo *K*α
μ (mm^{-1})	42.44
Crystal size (mm)	0.08 × 0.06 × 0.04
Data collection	
Diffractometer	STOE STADIVARI
Absorption correction	Multi-scan, STOE LANA
T_{min}, T_{max}	0.428, 0.654
No. of measured, independent and observed [$I > 3\sigma(I)$] reflections	15049, 2534, 1472
R_{int}	0.079
$(\sin \theta/\lambda)_{max}$ (Å^{-1})	0.792
Refinement	
$R[F^2 > 2\sigma(F^2)]$, $wR(F^2)$, S	0.042, 0.110, 1.40
No. of reflections	2534
No. of parameters	86
$\Delta\rho_{max}$, $\Delta\rho_{min}$ (e Å^{-3})	2.96, −2.68

3.3 Pavonite-type Structures

As mentioned in chapter 1.1.3, pavonites ^{N}P are structurally close to lillianites and can be seen as ^{1,N}L structures. Contrary to the andorite-type structures shown before, some of the presented structures contain Bi instead of Sb. Generally, no superstructures were found as every monoclinic structure had one lattice parameter about 4 Å long. However, some crystals of Bi4P showed satellite reflections of an incommensurate superstructure which has not yet been fully solved. The complexities of doing so are described in chapter 3.3.4.

3.3.1 Pavonite Structure containing Sb (SbP)

Crystals forming this pavonite structure were obtained when using Pb-poor reaction mixtures. It was however not possible to synthesise them using only Sb_2Se_3 and Cu_2Se which points to Pb being important for the formation of the structure. The monoclinic structure depicted in Figure 38 belongs to the space group type *C*2/*m* and has the cell parameters *a* = 13.6646(16) Å, *b* = 4.0881(4) Å, *c* = 15.0210(17) Å and β = 98.031(9)° at 300 K. The refined sum formula is $Cu_{1.52}Pb_{0.29}Sb_{5.45}Se_9$ with an excess positive charge of 2.4%.

The quadratic pyramidal [$BiSe_5$] polyhedra in original pavonite are replaced by 92% [$SbSe_5$] quadratic pyramids and 8% [$PbSe_8$] double-capped trigonal prisms at the Sb1/Pb1-position. The main structural feature are copper crosses formed by Cu4 and Cu4' along with an interstitial Cu position called Cu5 (see Figure 37). These originate from an octahedron that would usually have one metal atom located at its centre, which is not possible in this case owing to the crystal chemistry of Cu. This results in two pairs of symmetrically equivalent tetrahedral positions alongside which one pair of symmetrically equivalent interstitial Cu5 positions exists. Their occupancies were refined as free variables giving a cross with an occupation of 53% for Cu4 and 51% for Cu4'. Therefore, either 4% of the octahedra are occupied with two Cu atoms or there is some disordering with Sb or Pb. Considering the charge balance, Pb would fit better as less positive charge is added to the Cu position. Additionally, one of the Cu5 positions is occupied 10% of the time.

Four octahedra are grouped along the diagonal of the thick layer, this pavonite structure is thus denoted as ^{4}P. Apart from the Cu-cross, two different octahedral positions exist in the asymmetrical unit: The positionally disordered Sb2/Cu2 with 87% Sb and Sb3/Pb3 with 94% Sb. There are five different Se positions, none of them show any remarkable features.

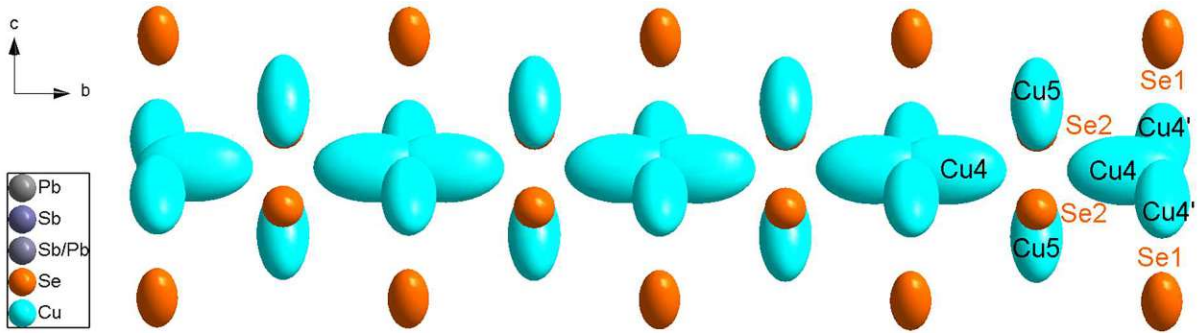

Figure 37: Copper crosses as found in SbP at 300 K

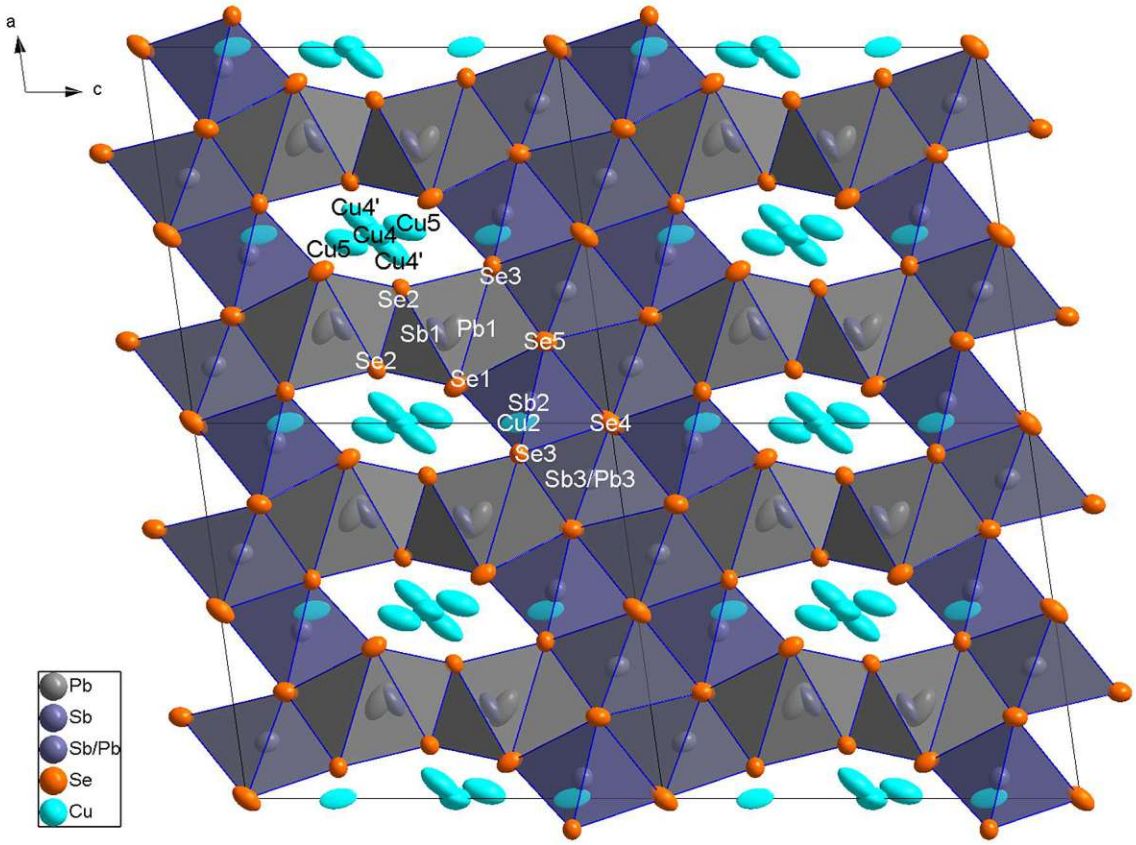

Figure 38: Pavonite-type structure of SbP at 300 K projected onto (010) drawn with 90% probability ellipsoids

Table 10: Experimental details for SbP at 300 K

Crystal data	
Chemical formula	$CuPbSbSe_3$
M_r	629.36
Crystal system, space group	Monoclinic, *C*2/*m*
Temperature (K)	300
a, *b*, *c* (Å)	13.6646(16), 4.0881(4), 15.0210(17)
β (°)	98.031(9)
V (Å^3)	830.88(16)
Z	1
Radiation type	Mo *K*α
μ (mm^{-1})	9.75
Crystal size (mm)	0.02 × 0.02 × 0.02
Data collection	
Diffractometer	STOE STADIVARI
Absorption correction	Multi-scan, STOE LANA
T_{min}, T_{max}	0.8227, 0.8227
No. of measured, independent and observed [$I > 2\sigma(I)$] reflections	7755, 2178, 679
R_{int}	0.196
$(\sin \theta/\lambda)_{max}$ (Å^{-1})	0.840

Refinement	
$R[F^2 > 2\sigma(F^2)]$, $wR(F^2)$, S	0.035, 0.130, 0.49
No. of reflections	2178
No. of parameters	82
$\Delta\rho_{max}$, $\Delta\rho_{min}$ (e Å^{-3})	2.01, −1.61

3.3.2 Temperature-dependent examination of SbP

A structural feature with high ADP tensors is a candidate for low-temperature and high-temperature measurements. The former to test whether these ADP tensors become smaller, thus proving that this is a dynamical effect, the latter to check whether the Cu4 and Cu4' position unite to form a pseudo-octahedral position or drift even further apart, which would imply better ion conductivity. Jana2020 was used to calculate the electron densities around the central point of the Cu crosses directly.

Experimentally, this was easy for 100 K as the same crystal could be measured on the same pin with the same instrument settings save for the temperature of the nitrogen stream. For the measurement at 500 K, the crystal had to be pushed into a capillary during which it broke. Therefore, only a fragment of the original crystal was measured. Collecting data at 600 K was tried but did not turn out successful because the crystal underwent a phase transition that did not result in another single crystal.

As expected, the cell parameters decreased (changes in brackets) at 100 K from the 300 K structure and were *a* = 13.5901(15) Å (-0.6%), *b* = 4.0838(2) Å (-0.1%), *c* = 14.946(2) (-0.5%) and β = 98.047(10)°. Apart from changes in the ADP tensors and minor differences for occupancies, no changes to the structure occur (see depiction in Figure 39). The cell parameters increase when heating to 500 K and are *a* = 13.6649(12) Å (±0%), *b* = 4.1007(3) Å (+0.3%), *c* = 15.0970(14) Å (+0.5%) and β = 98.240(7)°. The big structural change occurring is the disappearance of the Cu5 position while the ADP tensor of Cu2 enlarges significantly. The fragment used in this measurement contained less Cu and Pb (sum formula $Cu_{1.26}Pb_{0.08}Sb_{5.66}Se_9$, 2.2% excess positive charge).

Details regarding the examined crystal, data collection and refinement are given in Table 11 and Table 12, respectively.

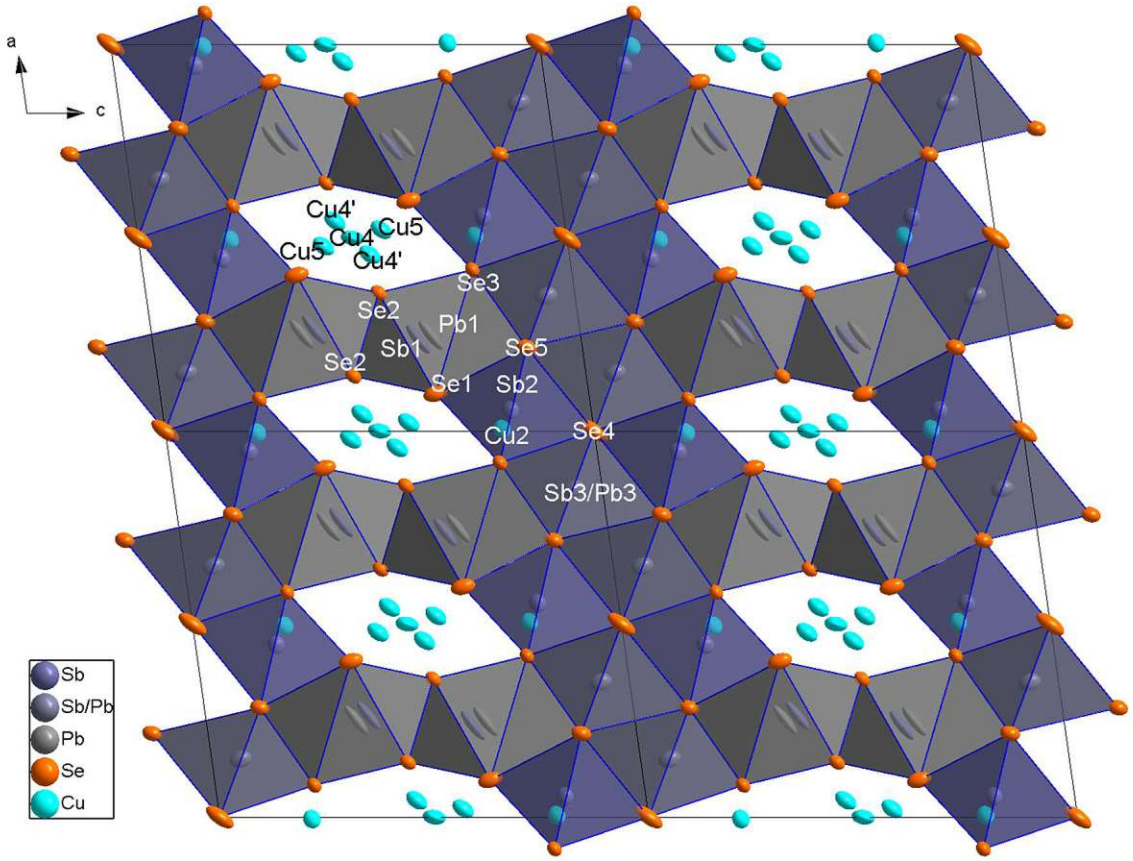

Figure 39: Pavonite-type structure of SbP at 100 K projected onto (010) drawn with 90% probability ellipsoids

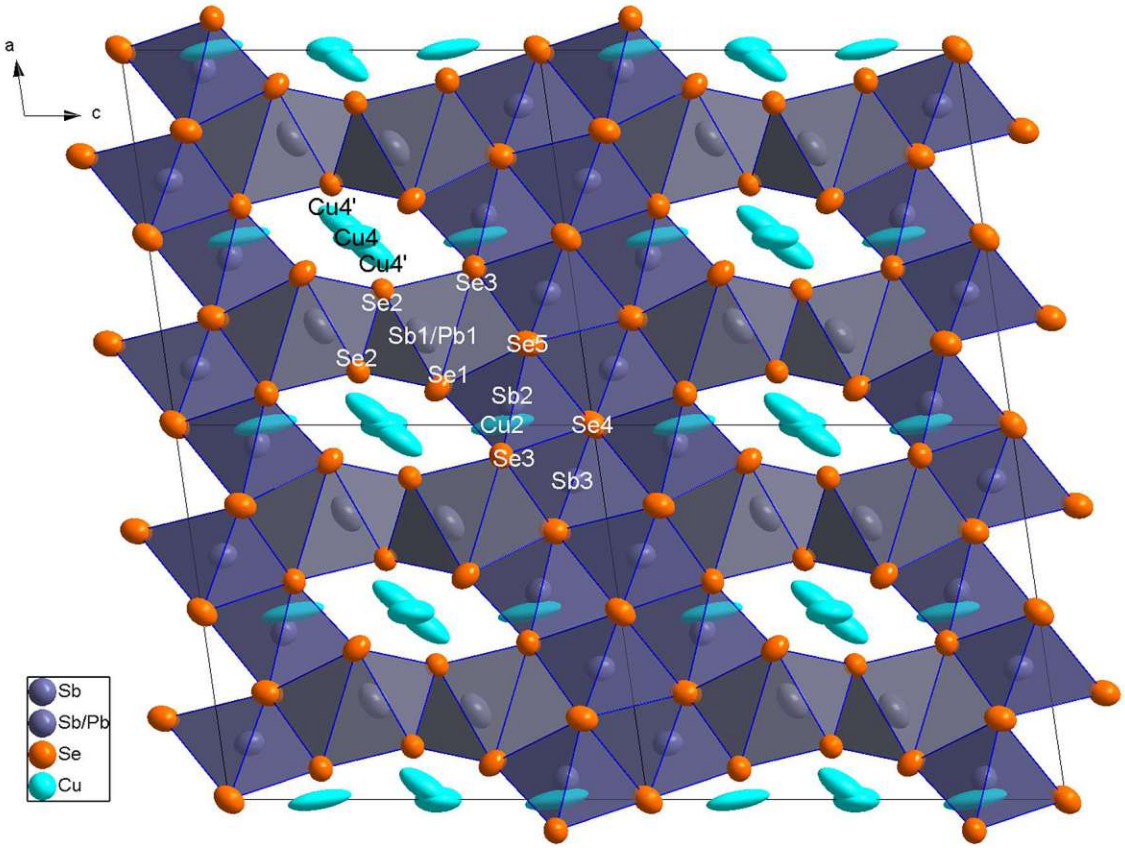

Figure 40: Pavonite-type structure of SbP at 500 K projected onto (010) drawn with 90% probability ellipsoids

Table 11: Experimental details for SbP at 100 K

Crystal data	
Chemical formula	$Cu_{2.97}Pb_{0.54}Sb_{10.86}Se_{18}$
M_r	3044.51
Crystal system, space group	Monoclinic, *C*2/*m*
Temperature (K)	100
a, *b*, *c* (Å)	13.5901(15), 4.0838(5), 14.946(2)
β (°)	98.047(10)
V (Å^3)	821.32(18)
Z	1
Radiation type	Mo *K*α
μ (mm^{-1})	33.35
Crystal size (mm)	0.02 × 0.02 × 0.02
Data collection	
Diffractometer	STOE STADIVARI
Absorption correction	Multi-scan, STOE LANA
T_{min}, T_{max}	0.821, 0.821
No. of measured, independent and observed [$I > 2\sigma(I)$] reflections	7751, 2178, 1115
R_{int}	0.134
$(\sin \theta/\lambda)_{max}$ (Å^{-1})	0.845
Refinement	
$R[F^2 > 2\sigma(F^2)]$, $wR(F^2)$, S	0.050, 0.094, 0.92
No. of reflections	2178
No. of parameters	70
$\Delta\rho_{max}$, $\Delta\rho_{min}$ (e Å^{-3})	3.55, −3.60

Table 12: Experimental details for SbP at 500 K

Crystal data	
Chemical formula	$Cu_{2.53}Pb_{0.15}Sb_{11.32}Se_{18}$
M_r	2991.85
Crystal system, space group	Monoclinic, *C*2/*m*
Temperature (K)	500
a, *b*, *c* (Å)	13.6649(12), 4.1007(3), 15.0970(14)
β (°)	98.240(7)
V (Å^3)	837.24(12)
Z	1
Radiation type	Mo *K*α
μ (mm^{-1})	30.87
Crystal size (mm)	0.08 × 0.05 × 0.02

Data collection	
Diffractometer	STOE STADIVARI
Absorption correction	Multi-scan, STOE LANA
No. of measured, independent and observed [$I > 2\sigma(I)$] reflections	7915, 2154, 666
R_{int}	0.152
$(\sin \theta/\lambda)_{max}$ (Å^{-1})	0.829
Refinement	
$R[F^2 > 2\sigma(F^2)]$, $wR(F^2)$, S	0.052, 0.267, 0.65
No. of reflections	2154
No. of parameters	67
$\Delta\rho_{max}$, $\Delta\rho_{min}$ (e Å^{-3})	2.70, −1.44

3.3.3 Electron Density at the disordered Cu4/Cu4'-Position

The electron density around the centre of the Cu4/Cu4' cross splits into four different positions at 100 K (see Figure 41) while it mostly lies in the centre at 500 K (see Figure 43). At 300 K, an intermediate state exists where the electron density at Cu4 positions is higher than in the centre. However, the electron density at the Cu4' positions is lower than in the centre (see Figure 42). This explains why the 90% probability ellipsoids of Cu4 and Cu4' do not overlap at 100 K (see Figure 39); the four disordered positions really are four disordered positions. At 300 K and 500 K this is not as simple. As the ellipsoids of Cu4 and Cu4' in Figure 37 already suggest by their overlapping, a significant part of the electron density lies in the centre at higher temperatures.

Changing the model from the Cu4/Cu4' cross to a central Cu atom had to be considered, especially in the case of the structure at 500 K. Using Jana2020, anharmonic ADP tensors up to the fourth level were calculated. However, these probability density functions did not resemble the F_{obs} map. While imperfect, the model with four distinct positions performs well and will be used for Bi4P, too. These kinds of disordered structure elements could show good thermoelectric performance since Cu atoms in Cu_2Se have already shown liquid-like ion mobility while maintaining low lattice thermal conductivity. [20] In the structure of Cu_2Se, Cu is disordered in tetrahedra in an antifluorite structure.

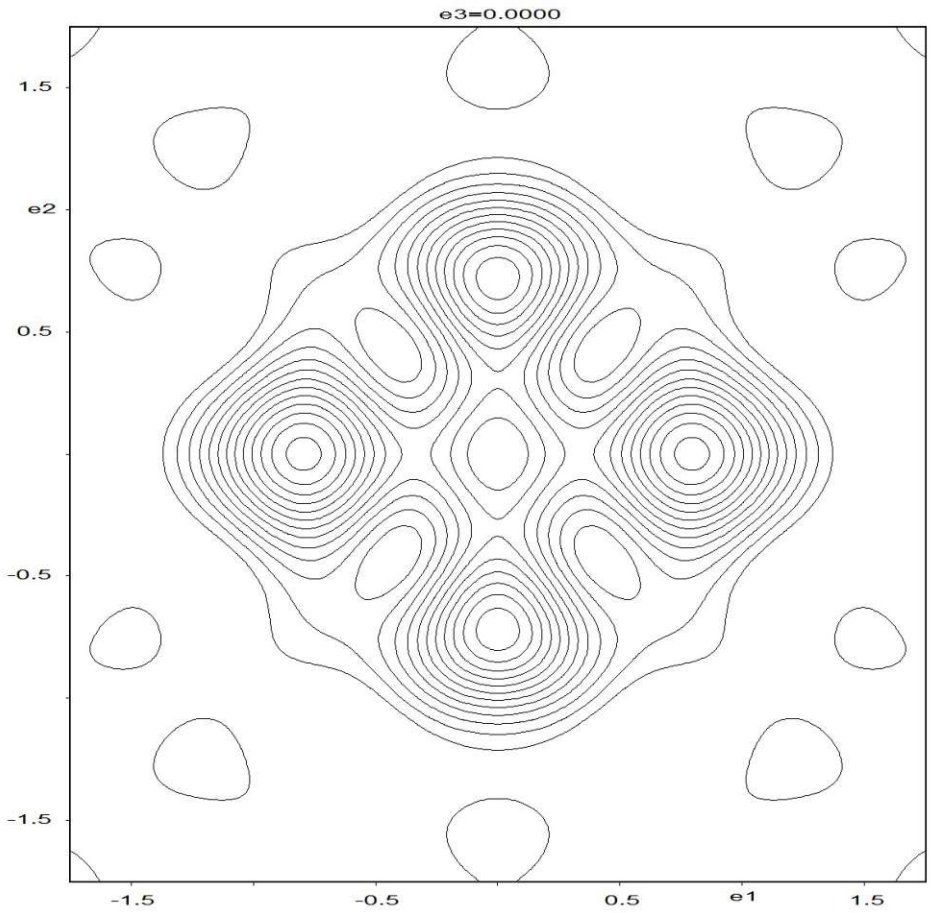

Figure 41: Contour plot of an F_{obs} section of SbP at 100 K parallel to (-101) centred around (0.5, 0.5, 0.5)

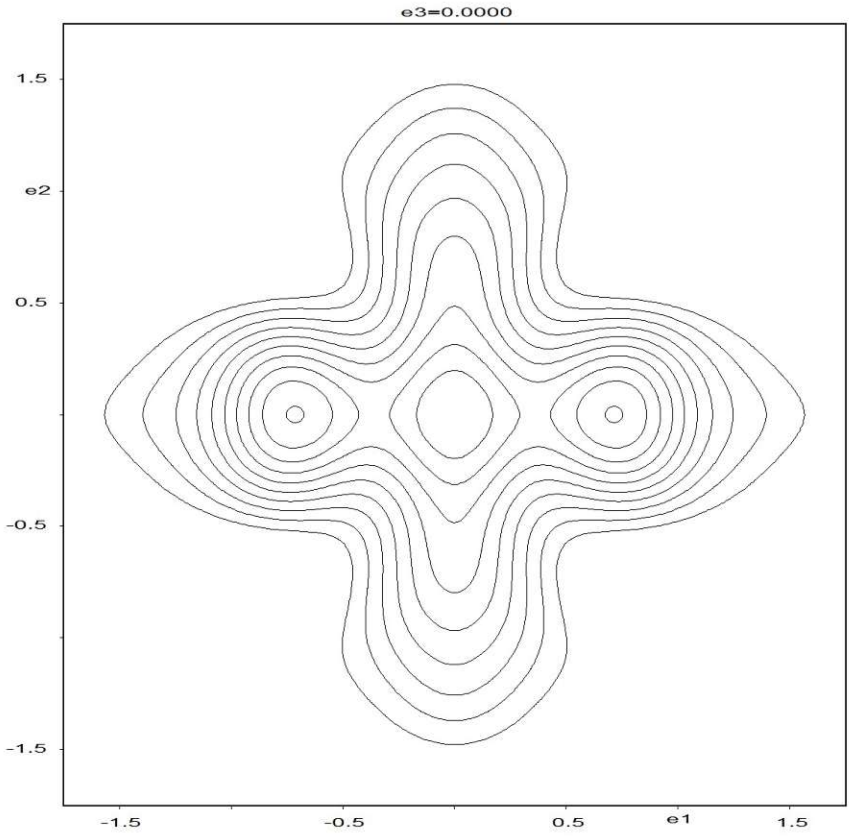

Figure 42: Contour plot of an F_{obs} section of SbP at 300 K parallel to (-101) centred around (0.5, 0.5, 0.5)

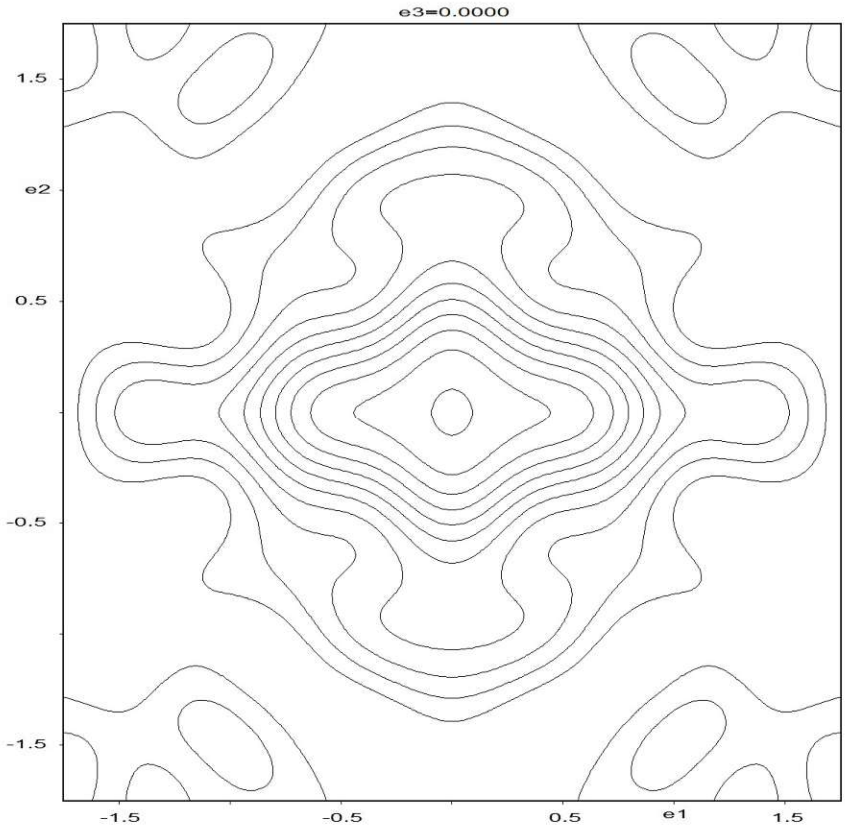

Figure 43: Contour plot of an F_{obs} section of SbP at 500 K parallel to (-101) centred around (0.5, 0.5, 0.5)

3.3.4 ^{4}P-type Pavonite containing Bi (Bi4P)

Lead-poor mixtures with Bi_2Se_3 lead to a ^{4}P-type pavonite which is isotypic to SbP. Its sum formula is $CuPbBi_5Se_9$ with cell parameters (changes to SbP in brackets) a = 13.7749(8) Å (+0.8%), b = 4.1985(2) Å (+2.7%), c = 15.3426(7) Å (+2.1%) and β = 99.284(4)° (+1.2%), space group type $C2/m$. A view along [010] is depicted in Figure 44. The structure is very similar to the one of SbP with the main difference being the absence of Cu2 and Cu5. The disordering observed in SbP at the Sb1/Pb1 and Sb3/Pb3 positions could not be quantified as Pb and Bi could not be distinguished from our data, since both elements possess nearly identical atomic form factors with Mo K_α radiation. Instead, the Bi1/Pb1 position was modelled with an occupancy ratio of 1:1. This way, the charges are balanced. The Bi1 position was chosen for disordering because the polyhedron resembles the $[PbSe_8]$ double-capped trigonal prism found in the andorite-type structures, although the polyhedron is better described as a square pyramid. As the Pb content is now accounted for, the remaining Bi positions were refined as pure Bi.

The Cu4/Cu4' cross is similar to the cross found in SbP but not equal. Firstly, the ratio of occupancies of Cu4 and Cu4' is 2:1. Furthermore, the positions are much more distinct at the measurement temperature of 300 K as Figure 45 shows (see Figure 42 for contrast): While there are obvious maxima for Bi4P, only the electron density of Cu4 produces maxima in SbP. Since Sb-containing andorites are known for their lone-pair micelles that distort the octahedra in the thick layer while this generally does not occur in Bi-containing lillianites, the distortions

seen in SbP were expected to lessen or disappear. While they certainly lessened, there are still visible distortions (see Figure 44) in Bi4P.

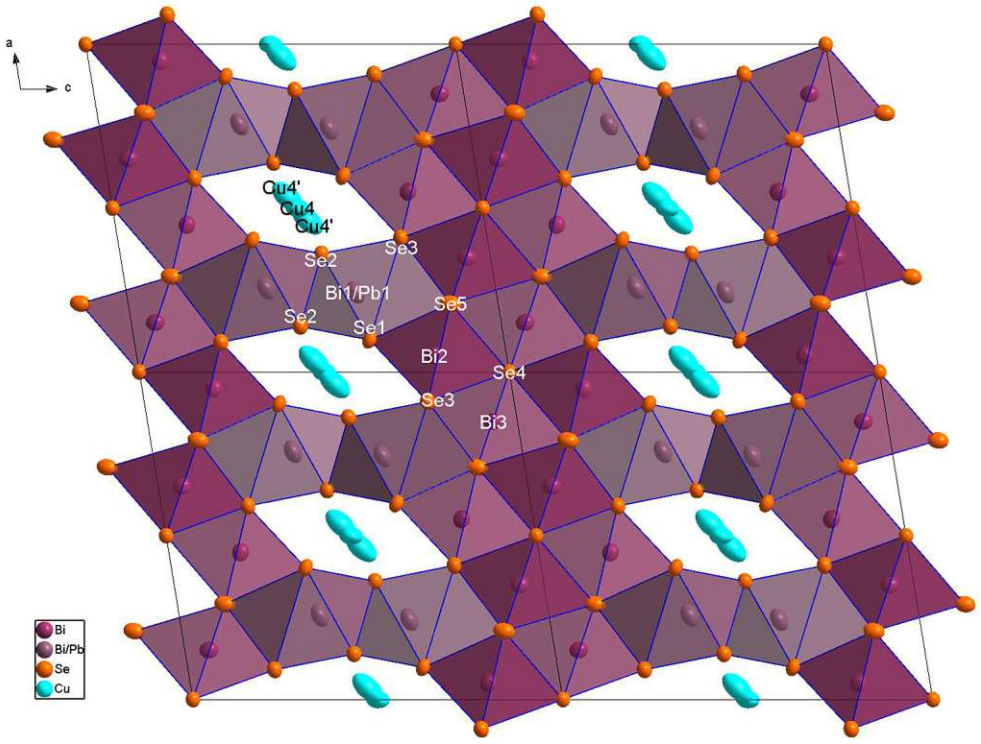

Figure 44: Pavonite-type structure of Bi4P at 300 K projected onto (010) drawn with 90% probability ellipsoids

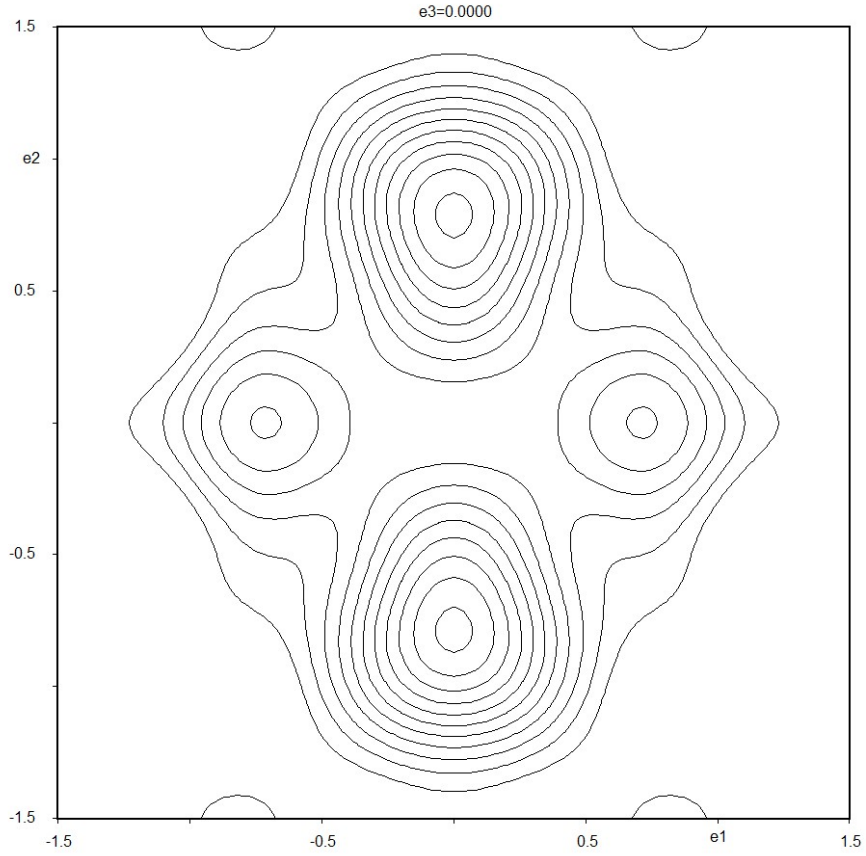

Figure 45: Contour plot of an F_{obs} section of Bi4P at 300 K parallel to (-101) centred around (0.5, 0.5, 0.5)

Table 13: Experimental details for Bi4P

Crystal data	
Chemical formula	$Cu_2PbBi_{11}Se_{18}$
M_r	4054.33
Crystal system, space group	Monoclinic, *C*2/*m*
Temperature (K)	300
a, *b*, *c* (Å)	13.7749(8), 4.1985(2), 15.3426(7)
β (°)	99.284(4)
V (Å^3)	875.70(8)
Z	1
Radiation type	Mo *K*α
μ (mm^{-1})	79.71
Crystal size (mm)	0.07 × 0.05 × 0.01
Data collection	
Diffractometer	STOE STADIVARI
Absorption correction	Multi-scan, STOE LANA
T_{min}, T_{max}	0.2862, 0.8194
No. of measured, independent and observed [$I > 2\sigma(I)$] reflections	10367, 2297, 1770
R_{int}	0.084
$(\sin \theta/\lambda)_{max}$ (Å^{-1})	0.838
Refinement	
$R[F^2 > 2\sigma(F^2)]$, $wR(F^2)$, S	0.047, 0.137, 1.03
No. of reflections	2297
No. of parameters	61
No. of restraints	1
$\Delta\rho_{max}$, $\Delta\rho_{min}$ (e Å^{-3})	2.84, −6.66

3.3.5 Incommensurate Bi4P (Bi4P_ic)

Besides crystals of Bi4P without any additional reflections (see Figure 46), some exhibited modulation as evidenced by weak satellite reflections (see Figure 47). The modulation wave vector has not yet been quantified likely owing to diffuse scattering which hinders the exact determination of the satellite coordinates in reciprocal space; however, it is close to (1/4, 0, 1/4) which would follow the green line in Figure 47 and retain the monoclinic structure since **q***b** = 0. There is a deviation as shown by the white lines which follow the vector resulting from reflections on this plane. As these white lines do not cross another main reflection, the structure is incommensurate. An analysis of these satellites could provide information about the disordering of Cu4/Cu4' in Bi4P which would be interesting regarding SbP as well.

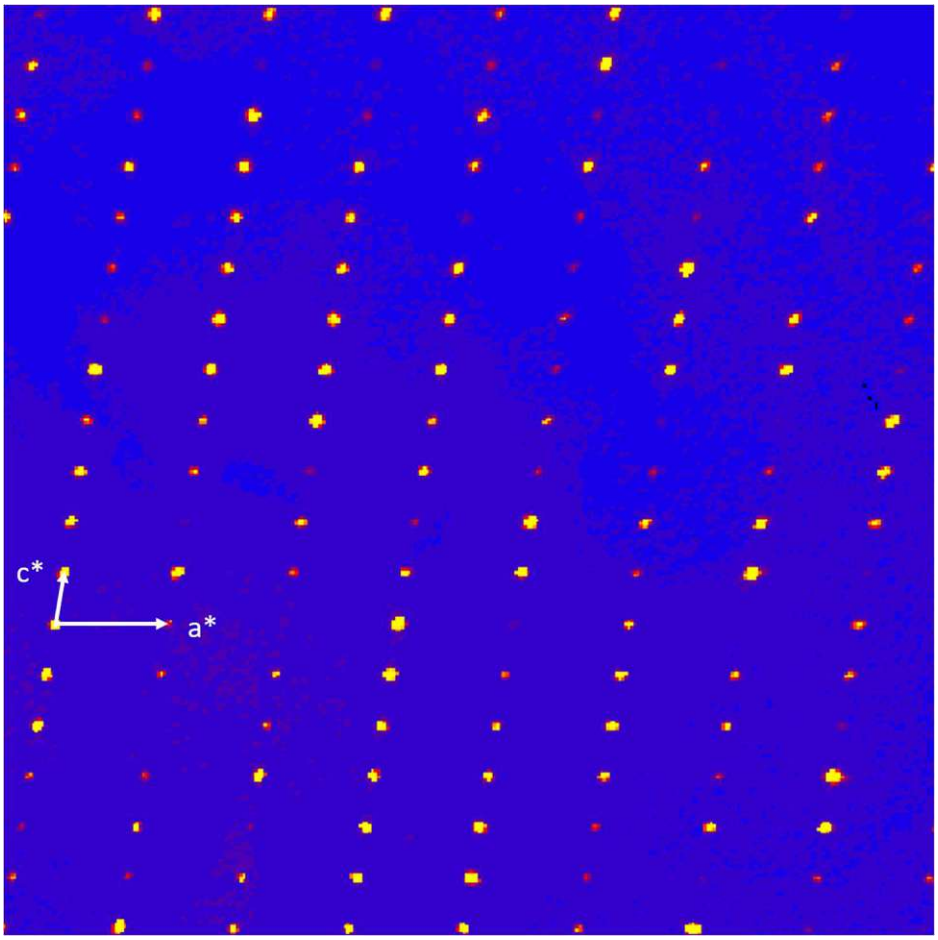

Figure 46: Exemplary reciprocal space reconstruction of Bi4P (precession image of layer h-1l)

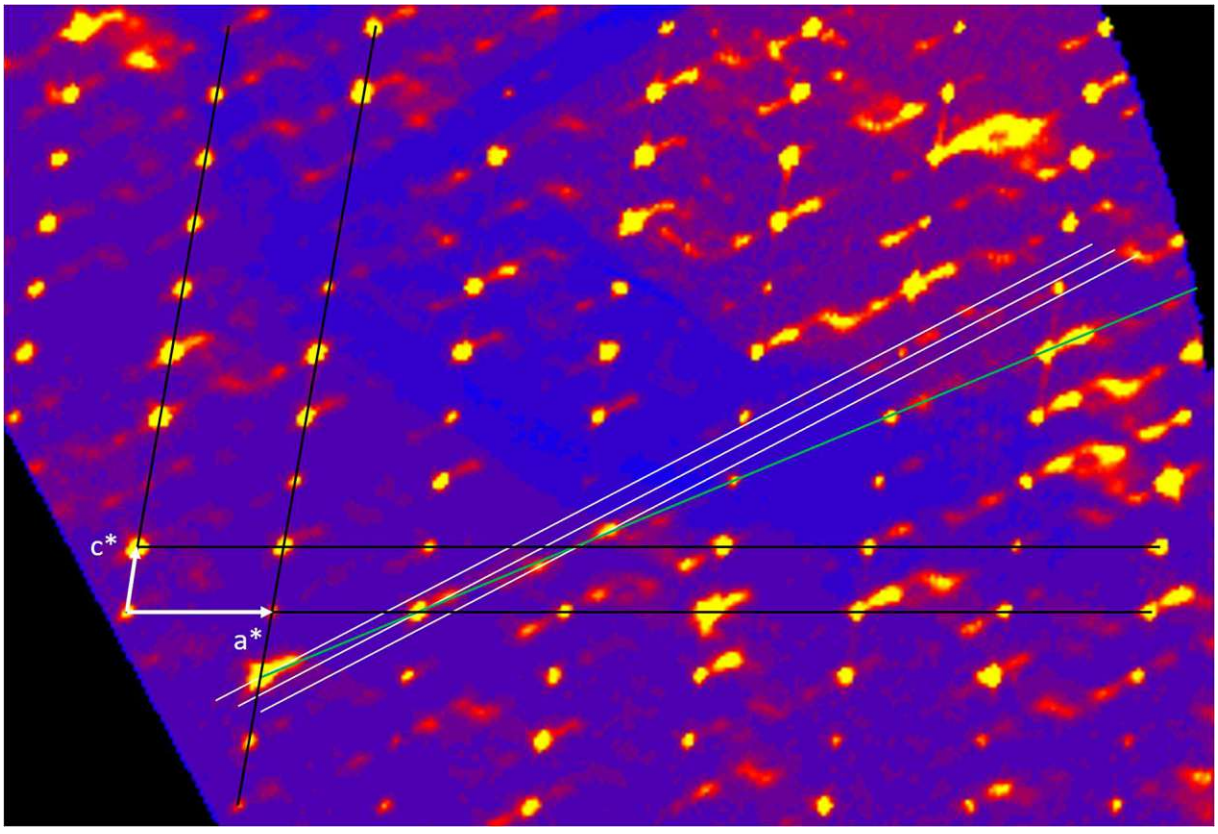

Figure 47: Exemplary reciprocal space reconstruction of Bi4P_ic: Main reflections according to coordinate system along black lines, satellites in direction of white lines, green line in direction of [101] (precession image of h0l)

3.3.6 ^{6}P-type Pavonite containing Bi (Bi6P)

This ^{6}P-type structure crystallises in the space group type *C*2/*m* with lattice parameters *a* = 14.0556(7) Å, *b* = 4.1844(2) Å, *c* = 19.6610(10) Å and β = 104.422(4)° with the sum formula $Cu_2Pb_4Bi_4Se_{11}$. A view along [010] is depicted in Figure 48. There are four positions in the structure that could be occupied by either Pb or Bi. Since there is the equivalent of two fully occupied Cu positions replacing the Cu4/Cu4' cross seen in SbP and Bi4P, the sum formula would be balanced at $Cu_2Pb_4Bi_4Se_{11}$. From there, two of the four Bi/Pb positions had to be marked as Pb and the other two as Bi. The placement of Pb at Pb1/Pb1' and Pb2 at the edge of the thick layer and Bi at Bi3 and Bi4 inside the thick layer is purely arbitrary and does not necessarily represent the reality of the structure. One possibility to differentiate these elements is the δ synthesis. [35] Some disordering is to be expected here which is not possible to model between Pb and Bi using data collected with only Mo K_α radiation.

The disordering of the Pb1 position is peculiar regarding the shapes of the ADP tensors. A possible explanation is disordering with Bi in a way where either Pb1 or Pb1' would be Bi. Pb1 has a site occupancy of 54% and Pb1' one of 46%. The site occupancies of Cu4' and Cu5/Cu5' are 46% and 54%, respectively, as well.

The structure of the chain of Cu4' and Cu5/Cu5' can better be understood when Cu5' (site occupancy 8.8%) and Se1' (site occupancy 7.1%) are taken out of the picture as in Figure 49. Every position is tetrahedral and only one of the copper atoms on the same y-coordinate is realised. The choice of name for Cu4' might seem odd since there is no Cu4 in this structure. However, this position is equivalent to the Cu4' position in SbP and Bi4P while Cu5 is equivalent to Cu5 in SbP. This sequence of Cu4' and Cu5 positions is similar to the proposed Cu2-Cui-Cu2 chain for the incommensurate andorite structure (Figure 27). Concludingly, experimental details are given in Table 14.

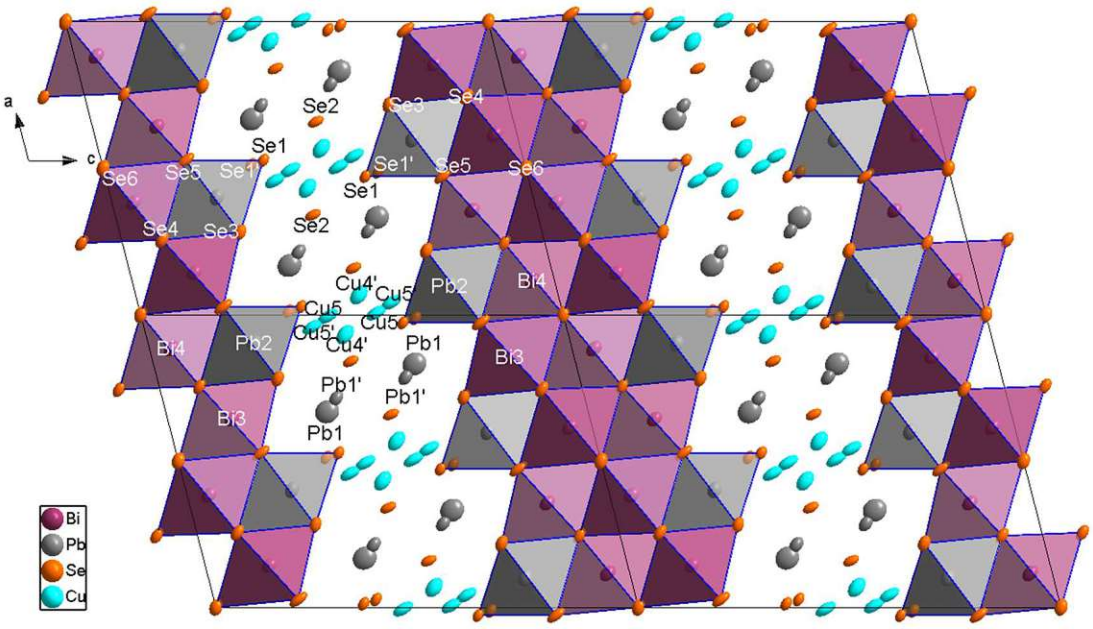

Figure 48: Pavonite-type structure of Bi6P at 300 K projected onto (010) drawn with 90% probability ellipsoids

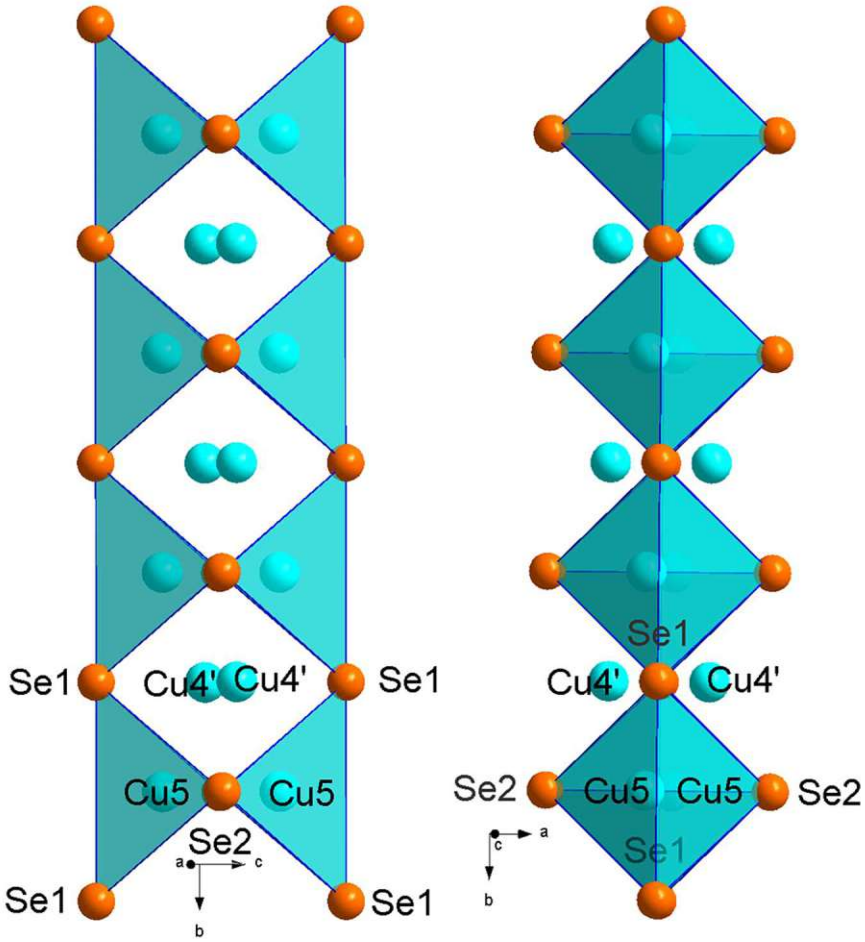

Figure 49: Cu chain with Cu5‘ and Se2‘ removed for easier understanding, only one of Cu4’ or Cu5 is occupied at the same time

Table 14: Experimental details for Bi6P

Crystal data	
Chemical formula	$Bi_8Cu_4Pb_8Se_{22}$
M_r	5320.66
Crystal system, space group	Monoclinic, *C*2/*m*
Temperature (K)	300
a, *b*, *c* (Å)	14.0556(7), 4.1844(2), 19.6610(10)
β (°)	104.422(4)
V (Å^3)	1119.91(10)
Z	1
Radiation type	Mo *K*α
μ (mm^{-1})	80.97
Crystal size (mm)	0.05 × 0.03 × 0.02
Data collection	
Diffractometer	STOE STADIVARI
Absorption correction	Multi-scan, STOE LANA
T_{min}, T_{max}	0.324, 0.723
No. of measured, independent and observed [$I > 2\sigma(I)$] reflections	10732, 2909, 2169
R_{int}	0.066
$(\sin \theta/\lambda)_{max}$ (Å^{-1})	0.835
Refinement	
$R[F^2 > 2\sigma(F^2)]$, $wR(F^2)$, S	0.103, 0.230, 1.23
No. of reflections	2909
No. of parameters	87
No. of restraints	1
$\Delta\rho_{max}$, $\Delta\rho_{min}$ (e Å^{-3})	6.86, −9.95

3.4 Composite Structures

The following structures differ from the others by their layers being only loosely connected to each other. The andorite and pavonite structures described before are layer structures but the bonds inside the layers are of similar strength to the bonds between the layers.

3.4.1 Cannizzarite-type $(PbSe)_5(Bi_2Se_3)_3$ (Cann1)

This cannizzarite-type [16] structure was refined against intensity data from a mediocre crystal in $P2_1/m$ with cell parameters a = 15.9476(12) Å, b = 4.1829(2) Å, c = 21.5059(13) Å and β = 97.613(6)°. This is the reason for the relatively high R_{obs} of 0.1625. Nevertheless, there is no reason to doubt the general structure as it is a compound known to literature where the distribution of Pb and Bi was already determined with resonant data. [17] In this reference, disordering of Pb and Bi is discussed at length with unsatisfactory results. For ease of comprehension, our data is depicted without disordered positions. In chapter 1.1.4, such a structure is presented based on data from minerals.

To describe the structure, it suffices to describe its two layers. There is one PbSe-layer where Pb generally is coordinated in square pyramids, although when Se atoms of the Bi_2Se_3 layer are considered, some Pb atoms show octahedral coordination which makes these metal positions prone to disordering with Bi. The Bi_2Se_3 layer consists of octahedrally coordinated Bi atoms and only has Se atoms on its edge. A projection of the structure is shown in Figure 50.

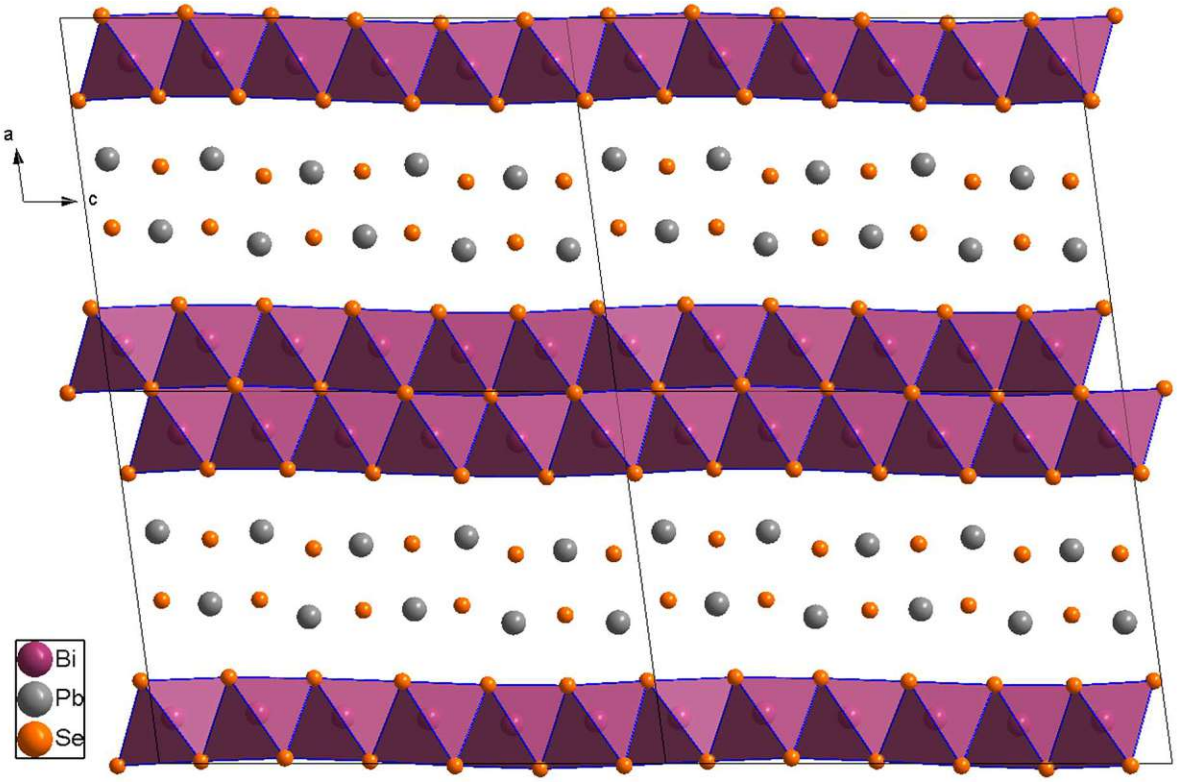

Figure 50: Structure of $(PbSe)_5(Bi_2Se_3)_3$ projected on (010)

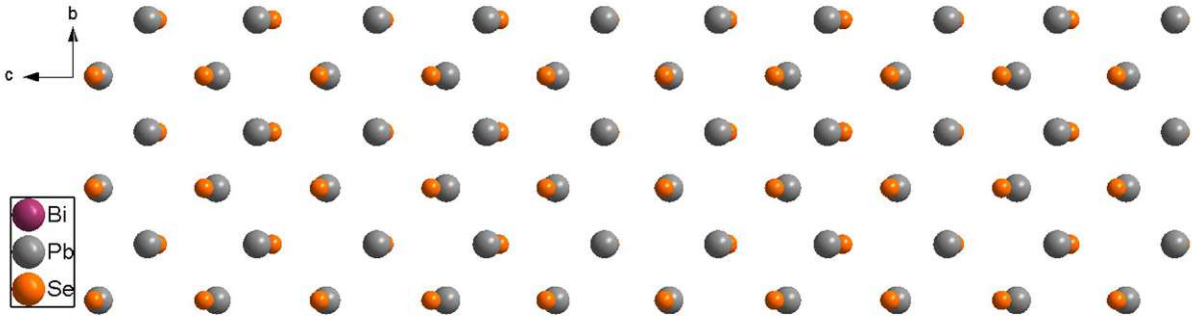

Figure 51: Pseudotetragonal PbSe layer of Cann1 viewed along [100]

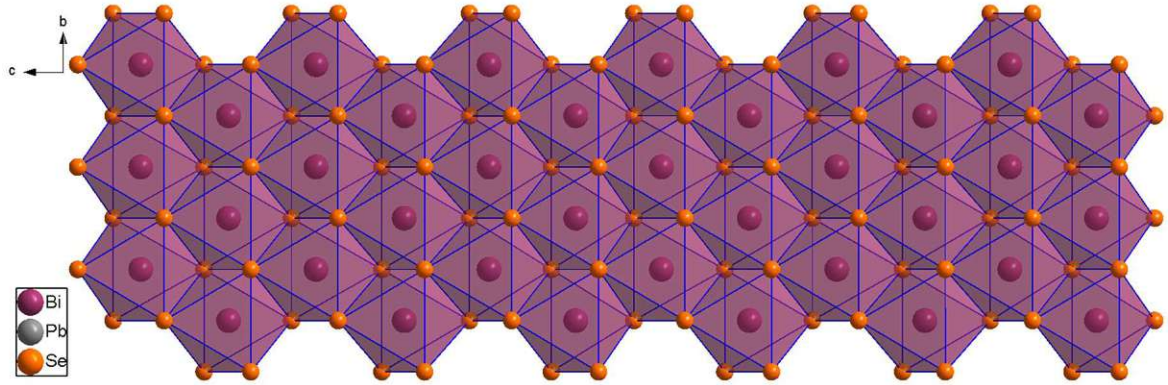

Figure 52: Pseudohexagonal Bi_2Se_3 layer of Cann1 viewed along [100]

Figure 51 and Figure 52 show the layers of Cann1 viewed from the top. The PbSe layer is pseudotetragonal (mineralogists typically call it a Q layer) and the Bi_2Se_3 layer pseudohexagonal (an H layer). The idealised symmetries are not realised because both layers are commensurately modulated. As seen in Figure 50, inside one unit cell there are five Pb atoms and 6 Bi atoms along [001] which means the pseudotetragonal layer has a fivefold superstructure while the pseudohexagonal layer's superstructure is sixfold. The fivefold superstructure can be recognised from Figure 51, if the positions of the Se atoms relative to Pb atoms are taken into consideration. The only effect of the sixfold superstructure are displacements along [100], therefore it cannot be appreciated in Figure 52; however, the wave-like shape of the layer is obvious in Figure 50.

The modulation stems from the fact that the hexagonal and square layer lattices are incompatible. The structure can be considered as a commensurate layer composite which means that two modulated structures are described together in one unit cell. The example of Cann1 is commensurate, but incommensurate variants of these composite structures exist, too. [21] An example would be a cylindrite-type structure called merelaniite whose modulation is described by two wave vectors. [36]

Experimental details are omitted here and for the other cannizzarite-type phase because the quality of the crystal and the resulting data were not satisfactory.

3.4.2 Cannizzarite-type $(PbSe)_5(Bi_2Se_3)_6$ (Cann2)

Contrary to the other cannizzarite homologue, this compound crystallises in the space group type *C*2/*m* with cell parameters *a* = 53.233(4) Å, *b* = 4.1728(2) Å, *c* = 21.5252(15) Å and β = 107.401(5)°. Here, only a structure with an R_{obs} of 0.1855 could be refined from our data and, even worse, it is missing one Se atom entirely. Therefore, structural data from literature was used to draw Figure 53. This compound has even been investigated for its thermoelectric properties. [37] Structurally it is very similar to $(PbSe)_5(Bi_2Se_3)_3$, the main difference being that the Bi_2Se_3 layer is doubled. The change from $P2_1/m$ to $C2/m$ stems from the layers not being aligned the same way. While in Cann1 only one type of Bi_2Se_3 and PbSe layer form the structure, these layers experience a displacement of 0.5 *b* in Cann2 every second time if two neighbouring Bi_2Se_3 layers are seen as one. Therefore, there are six layers (or four depending on whether two neighbouring Bi_2Se_3 layers are seen as two or one) in one unit cell which is the reason for the large cell parameter *a*.

It should be reiterated that the locations of Pb and Bi are not known from our data nor did the authors of reference [37] collect resonant diffraction data. Their bond valence calculations show disordering with some positions labelled as Pb being almost fully occupied by Bi. This might be disadvantageous from a crystallographic point of view; however, these disordered positions likely contribute to the low thermal lattice conductivity exhibited by this compound.

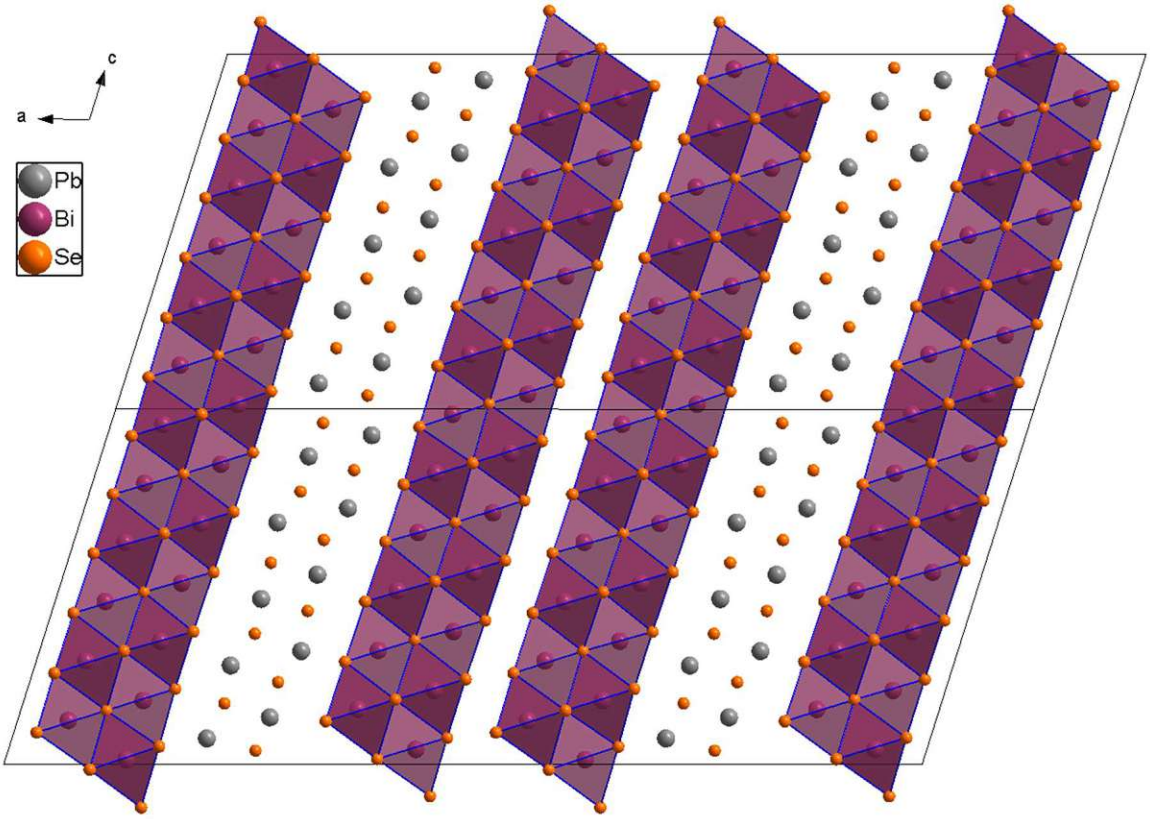

Figure 53: Structure of $(PbSe)_5(Bi_2Se_3)_6$ projected onto (010) drawn with cif data from [37]

3.4.3 Trigonal $(Cu_2Se_2)(Bi_2Se_3)$ (DiSe)

This structure is unknown to literature and crystallises in *P*-3*m*1 with cell parameters *a* = 4.0737(2) Å and *c* = 15.4530(10) Å. The sum formula $Cu_2Bi_2Se_5$ does not look balanced at first glance, however, this structure contains Se_2^{2-} dumbbells between the Cu tetrahedra with Se being reduced form -II to -I during the synthesis. To avoid confusion, the sum formula is better expressed as $(Cu_2Se_2)(Bi_2Se_3)$. In Figure 54, an unusual projection of the structure is depicted that is more useful in showing the connection of the Se_2^{2-} dumbbells along the cell edges. Even though the Bi_2Se_3 layer looks different in this projection, it is the same layer as in the two cannizzarite-type structures described before.

Notably, the layers are of similar thickness with the (Bi_2Se_3) layer stretching 45.64% of *c* (7.053 Å) and the (Cu_2Se_2) layer accordingly 54.36% of *c* (8.400 Å). Some residual electron density peaks in the (Bi_2Se_3) layer indicated disordering with another Cu layer, possibly resulting in a structure with the sum formula $(Cu_2Se_2)_{1+x}(Bi_2Se_3)$. This could also be seen as an intergrowth of $(Cu_2Se_2)(Bi_2Se_3)$ with Cu_2Se_2. In Figure 55 a precession image of DiSe is shown where some diffuse scattering is visible in direction of c*. This lends credibility to the stacking faults suspected from residual electron density in the refinement. Experimental details are given in Table 15.

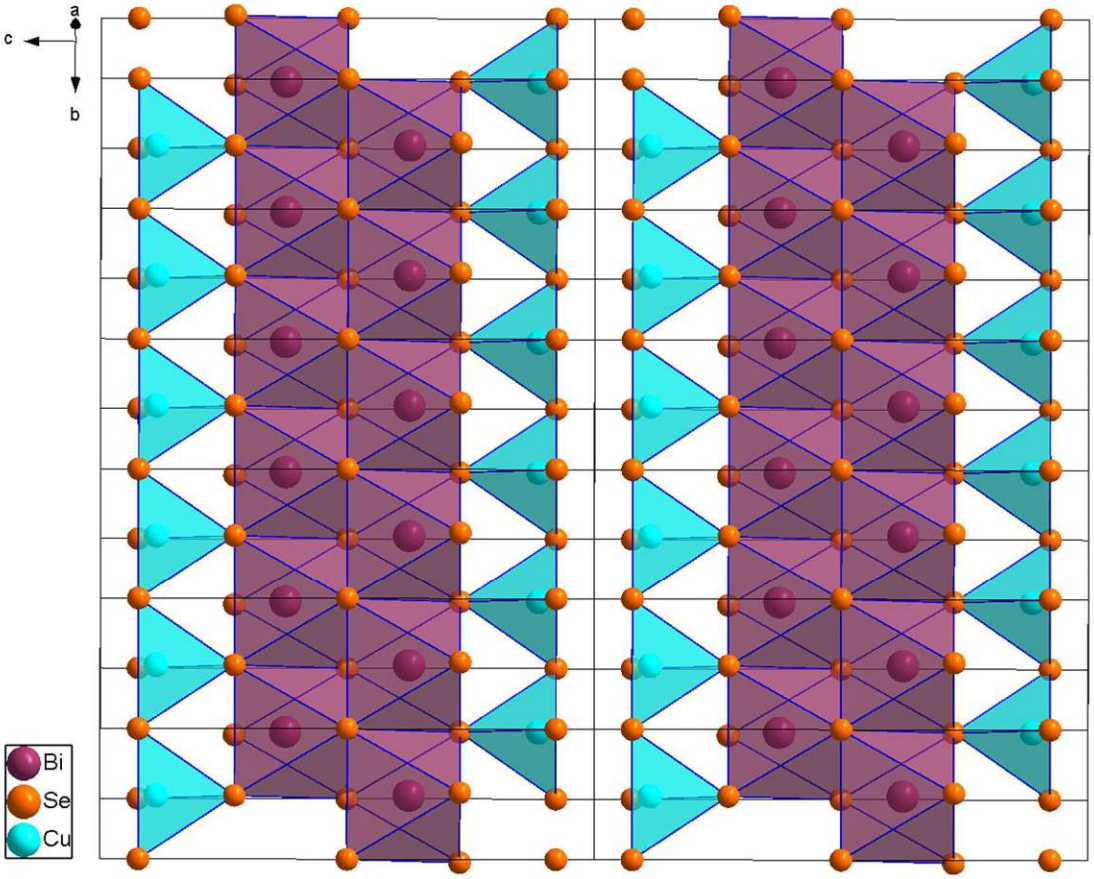

Figure 54: Structure of $(Cu_2Se_2)(Bi_2Se_3)$ projected onto (120)

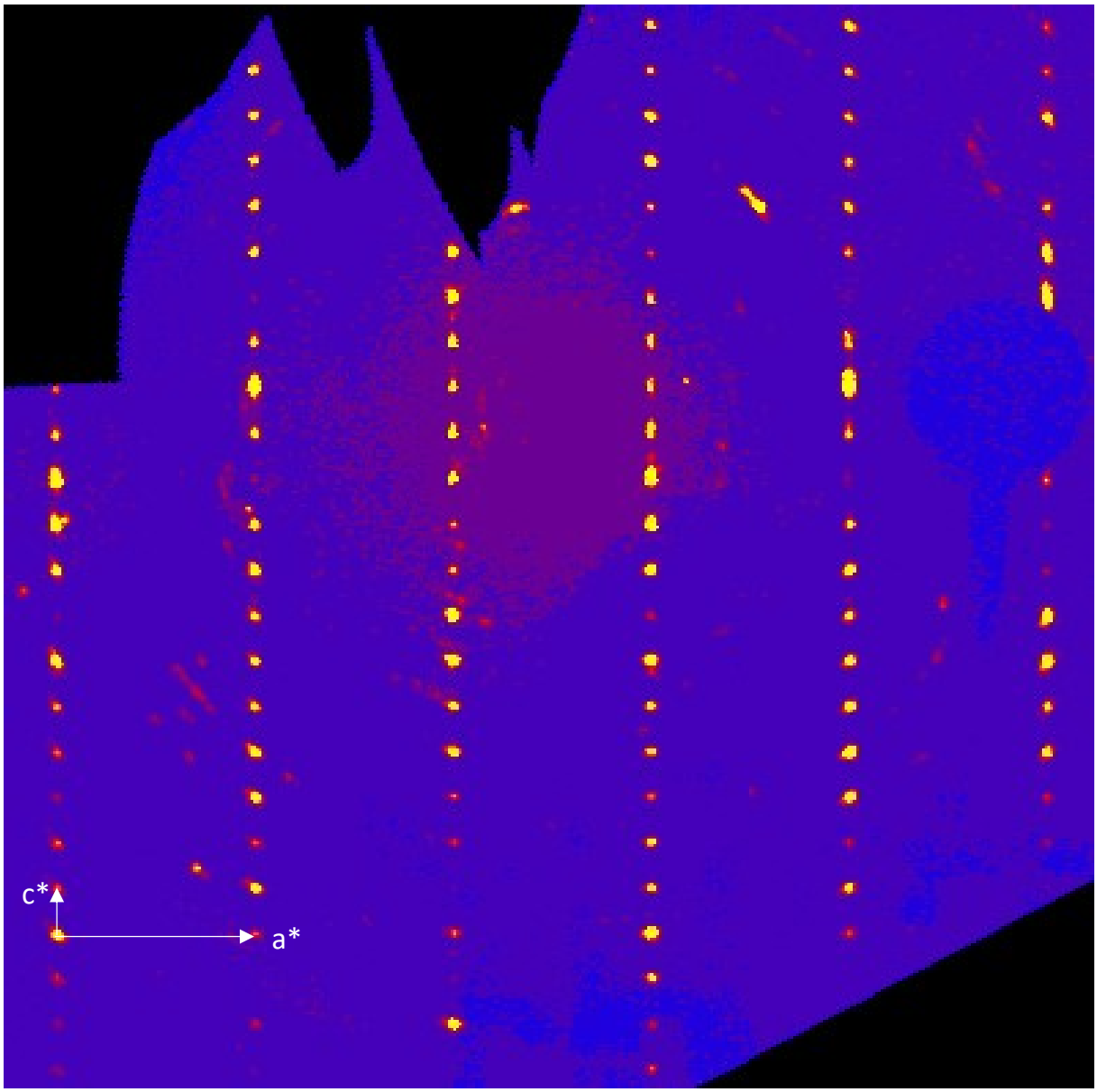

Figure 55: Precession image of DiSe (layer h1l) showing diffuse scattering around some reflections

Table 15: Experimental details for DiSe

Crystal data	
Chemical formula	$Bi_2Cu_2Se_5$
M_r	939.84
Crystal system, space group	Trigonal, *P*-3*m*1
Temperature (K)	300
a, *c* (Å)	4.0737(2), 15.4530(10)
V (Å^3)	222.09(3)
Z	1
Radiation type	Mo *K*α
μ (mm^{-1})	64.62
Crystal size (mm)	0.06 × 0.05 × 0.02
Data collection	
Diffractometer	STOE STADIVARI
Absorption correction	Multi-scan, STOE LANA
T_{min}, T_{max}	0.0671, 0.4063
No. of measured, independent and observed [$I > 2\sigma(I)$] reflections	3217, 302, 286
R_{int}	0.127
$(\sin \theta/\lambda)_{max}$ (Å^{-1})	0.699
Refinement	
$R[F^2 > 2\sigma(F^2)]$, $wR(F^2)$, S	0.078, 0.214, 1.23
No. of reflections	302
No. of parameters	16
$\Delta\rho_{max}$, $\Delta\rho_{min}$ (e Å^{-3})	12.90, −2.29

4 Conclusion

As expected, new compounds could be synthesised that add to the plethora of sulfosalt compounds currently known. With the system of compounds having the approximate sum formula $CuPbSb_3Se_6$, a complex system was uncovered that contains not only a new incommensurate structure but two commensurate andorite-like structures and one new structure type with *Pnnm*-$CuPbSb_3Se_6$. Obtaining single-phase samples of the latter compound or the commensurate compounds seems impossible from the standpoint of this thesis but hopefully, further research can disprove this assumption.

The assumption is mainly driven by the intergrown crystals of these structures and their common high-temperature phase. After passing the point where all satellites disappear, the ratios of the two phases changed when cooling down the crystal. Therefore, even when a sample of pure 2x is obtained, doing experiments where it is required to be heated past 357 °C, the sample will not be retained as pure 2x. However, if the oriented intergrowth is seen as one phase, the product would have been pure enough to conduct transport measurements. Likewise, the incommensurate structure, containing more Pb, possesses a distinct composition compared to the others and is thus a good candidate for the synthesis of a single-phase material and subsequent transport measurements as well.

For the new compounds in the Cu-Pb-Bi-Se system, further research is likewise needed. The most interesting new phases are the incommensurate version of Bi4P and the diselenide composite structure DiSe. Not only would the structure of Bi4P_ic be of interest, the reason for most crystals of this phase showing no satellites at all would have to be investigated as well. As for the diselenide compound, while its general structure is known, the reality of how crystals of this phase are made up is uncertain. Disordering of Pb and Bi should be investigated with resonant x-ray diffraction, especially Bi4P and Bi6P.

References

[1] H. H. Binder, *Lexikon der chemischen Elemente. Das Periodensystem in Zahlen, Fakten und Daten.* Stuttgart: S. Hirzel Verlag, 1999.

[2] X. Zhang and L. D. Zhao, "Thermoelectric materials: Energy conversion between heat and electricity," *Journal of Materiomics*, vol. 1, no. 2. 2015. doi: 10.1016/j.jmat.2015.01.001.

[3] H. Wang, Y. Pei, A. D. Lalonde, and G. J. Snyder, "Heavily doped p-type PbSe with high thermoelectric performance: An alternative for PbTe," *Advanced Materials*, vol. 23, no. 11, 2011, doi: 10.1002/adma.201004200.

[4] Y. Moëlo *et al.*, "Sulfosalt systematics: a review. Report of the sulfosalt sub-committee of the IMA Commission on Ore Mineralogy," *European Journal of Mineralogy*, vol. 20, no. 1, 2008, doi: 10.1127/0935-1221/2008/0020-1778.

[5] H. H. Otto and H. Strunz, "Zur Kristallchemie synthetischer Blei-Wismut-Spießglanze.," *Neues Jahrb. Miner. Abh.*, vol. 108, pp. 1–19, 1968.

[6] J. Takagi and Y. Takéuchi, "The crystal structure of lillianite," *Acta Crystallographica Section B*, vol. 28, no. 2, 1972, doi: 10.1107/s0567740872002924.

[7] E. Makovicky and S. Karup-Møller, "Chemistry and crystallography of the lillianite homologous series. I. General properties and definitions .," in *Neues Jahrb. Mineral., Abh.*, vol. 130, 1977, pp. 264–287.

[8] E. Makovicky, "The building principles and classification of bismuth-lead sulphosalts and related compounds.," *Fortschritte der Mineralogie*, vol. 59, pp. 137–190, 1981.

[9] E. Makovicky and D. Topa, "Lillianites and andorites: new life for the oldest homologous series of sulfosalts," *Mineral Mag*, vol. 78, no. 2, 2014, doi: 10.1180/minmag.2014.078.2.11.

[10] P. Berlepsch, T. Armbruster, E. Makovicky, C. Hejny, D. Topa, and S. Graeser, "The crystal structure of (001) twinned xilingolite, $Pb_3Bi_2S_6$, from Mittal-Hohtenn, Valais, Switzerland," *Can Mineral*, vol. 39, no. 6, 2001, doi: 10.2113/gscanmin.39.6.1653.

[11] I. C. Liang *et al.*, "New metal chalcogenides found in $Mn_{N-1}(Gd_{2-xInx})S_{N+2}$ (N = 3, 4, 5): Syntheses, structures, and magnetic properties," *Dalton Transactions*, vol. 46, no. 4, pp. 1228–1236, 2017, doi: 10.1039/c6dt04382h.

[12] F. Heinke, F. Nietschke, C. Fraunhofer, I. Dovgaliuk, J. Schiller, and O. Oeckler, "Structure and thermoelectric properties of the silver lead bismuth selenides $Ag_5Pb_9Bi_{19}Se_{40}$ and $AgPb_3Bi_7Se_{14}$," *Dalton Transactions*, vol. 47, no. 35, 2018, doi: 10.1039/c8dt01895b.

[13] H. Sawada, I. Kawada, E. Hellner, and M. Tokonami, “The crystal structure of senandorite (andorite VI): $PbAgSb_3S_6$,” *Zeitschrift fur Kristallographie - New Crystal Structures*, vol. 180, no. 1–4, 1987, doi: 10.1524/zkri.1987.180.1-4.141.

[14] B. Makovicky, W. C. Mumme, and J. A. Watts, “THE CRYSTALS STRUCTURE OF SYNTHETIC PAVONITE, $AgBi_3S_5$, AND THE DEFINITION OF THE PAVONITE HOMOLOGOUS SERIES,” *Can Mineral*, vol. 15, no. 3, pp. 339–348, 1977, Accessed: Nov. 04, 2022. [Online]. Available: https://pubs.geoscienceworld.org/canmin/article-abstract/15/3/339/11198/The-crystal-structure-of-synthetic-pavonite-AgBi-3

[15] Y. S. Borodaev *et al.*, “Rare sulfosalts from Vulcano, Aeolian Islands, Italy. III. Wittite and cannizzarite,” *Can Mineral*, vol. 38, no. 1, 2000, doi: 10.2113/gscanmin.38.1.23.

[16] D. Topa, E. Makovicky, and H. Dittrich, “The crystal structure Of 7H : 12Q cannizzarite from Vulcano, Italy,” *Can Mineral*, vol. 48, no. 3, pp. 483–495, Jun. 2010, doi: 10.3749/canmin.48.3.483.

[17] Y. Zhang *et al.*, “Determining metal ion distributions using resonant scattering at very high-energy K-edges: Bi/Pb in Pb5Bi6Se14,” *J Appl Crystallogr*, vol. 38, no. 3, 2005, doi: 10.1107/S0021889805005686.

[18] R. Freer *et al.*, “Key properties of inorganic thermoelectric materials - Tables (version 1),” *JPhys Energy*, vol. 4, no. 2, 2022, doi: 10.1088/2515-7655/ac49dc.

[19] G. J. Snyder and E. S. Toberer, “Complex thermoelectric materials,” *Nature Materials*, vol. 7, no. 2. 2008. doi: 10.1038/nmat2090.

[20] H. Liu *et al.*, “Copper ion liquid-like thermoelectrics,” *Nat Mater*, vol. 11, no. 5, 2012, doi: 10.1038/nmat3273.

[21] S. van Smaalen, *Incommensurate Crystallography*. Oxford: Oxford University Press, 2012.

[22] M. Baake and U. Grimm, *Aperiodic Order*. Cambridge University Press, 2013. doi: 10.1017/CBO9781139025256.

[23] A. Janner and T. Janssen, “Superspace groups,” *Physica A: Statistical Mechanics and its Applications*, vol. 99, no. 1–2, pp. 47–76, 1979, doi: 10.1016/0378-4371(79)90124-9.

[24] G. Bergerhoff, I. D. Brown, F. H. Allen, and R. Sievers, “Crystallographic Databases.” International Union of Crystallography, Chester, pp. 77–95.

[25] J. Koziskova, F. Hahn, J. Richter, and J. Kožíšek, “Comparison of different absorption corrections on the model structure of tetrakis(μ_2-acetato)-diaqua-di-copper(II),” *Acta Chimica Slovaca*, vol. 9, no. 2, 2016, doi: 10.1515/acs-2016-0023.

[26] G. M. Sheldrick, “SHELXT - Integrated space-group and crystal-structure determination,” *Acta Crystallogr A*, vol. 71, no. 1, 2015, doi: 10.1107/S2053273314026370.

[27] O. v. Dolomanov, L. J. Bourhis, R. J. Gildea, J. A. K. Howard, and H. Puschmann, “OLEX2: A complete structure solution, refinement and analysis program,” *J Appl Crystallogr*, vol. 42, no. 2, 2009, doi: 10.1107/S0021889808042726.

[28] G. M. Sheldrick, “Crystal structure refinement with SHELXL,” *Acta Crystallogr C Struct Chem*, vol. 71, 2015, doi: 10.1107/S2053229614024218.

[29] C. B. Hübschle, “ShelXle: a Qt graphical user interface for SHELXL,” *Acta Crystallogr A Found Adv*, vol. 75, no. a1, 2019, doi: 10.1107/s0108767319098143.

[30] V. Petříček, M. Henriques, and M. Dušek, “JANA2020 – magnetic option,” *Acta Crystallogr A Found Adv*, vol. 77, no. a2, 2021, doi: 10.1107/s0108767321095076.

[31] K. Yamamoto and S. Kashida, “X-ray study of the average structures of Cu2Se and Cu1.8S in the room temperature and the high temperature phases,” *J Solid State Chem*, vol. 93, no. 1, 1991, doi: 10.1016/0022-4596(91)90289-T.

[32] A. Edenharter, W. Nowacki, and Y. Takéuchi, “Verfeinerung der Kristallstruktur von Bournonit [$(SbS_3)_2Cu_2^{IV}Pb^{VII}Pb^{VIII}$] und von Seligmannit [$(AsS_3)_2Cu_2^{IV}Pb^{VII}Pb^{VIII}$],” *Zeitschrift fur Kristallographie - New Crystal Structures*, vol. 131, no. 1–6, 1970, doi: 10.1524/zkri.1970.131.1-6.397.

[33] K. B. Chen and C. S. Lee, “Experimental and theoretical studies of $Sn_{3-\delta}Pb_\delta Bi_2Se_6$ (δ=0.0–0.7),” *J Solid State Chem*, vol. 183, no. 4, pp. 807–813, Apr. 2010, doi: 10.1016/J.JSSC.2010.01.011.

[34] J. Li *et al.*, “Thermoelectric Material $SnPb_2Bi_2S_6$: The ^{4,4}L Member of Lillianite Homologous Series with Low Lattice Thermal Conductivity,” *Inorg Chem*, vol. 58, no. 2, 2019, doi: 10.1021/acs.inorgchem.8b02899.

[35] R. Wulf, “Experimental distinction of elements with similar atomic number using anomalous dispersion (δ synthesis): an application of synchrotron radiation in crystal structure analysis,” *Acta Crystallographica Section A*, vol. 46, no. 8, 1990, doi: 10.1107/S0108767390004469.

[36] L. Bindi, A. Dasgupta, P. Mukherjee, J. Gao, X. Yang, and J. A. Jaszczak, “Misfit-generated structural and optical anisotropies of the natural MoS2−PbS van der Waals heterostructure merelaniite,” *Phys Rev Mater*, vol. 6, no. 11, p. 115202, Nov. 2022, doi: 10.1103/PhysRevMaterials.6.115202.

[37] S. Sassi *et al.*, “Crystal Structure and Transport Properties of the Homologous Compounds $(PbSe)_5(Bi2Se3)_{3m}$ (m = 2, 3),” *Inorg Chem*, vol. 57, no. 1, 2018, doi: 10.1021/acs.inorgchem.7b02656.

Table of Figures

List of Tables